論文 / 著書情報
Article / Book Information

題目(和文)	マイクロ・ナノラマン分光によるナノマテリアルの局所物性評価に関する研究
Title(English)	Characterization of local physicochemical properties of nano-sized materials by micro and nano-Raman spectroscopy
著者(和文)	BaloisMariaVanes
Author(English)	Maria Vanessa Balois
出典(和文)	学位:博士（理学）, 学位授与機関:東京工業大学, 報告番号:甲第9959号, 授与年月日:2015年9月25日, 学位の種別:課程博士, 審査員:林　智広,早澤　紀彦,原　正彦,北村　房男,尾笹　一成
Citation(English)	Degree:Doctor (Science), Conferring organization: Tokyo Institute of Technology, Report number:甲第9959号, Conferred date:2015/9/25, Degree Type:Course doctor, Examiner:,,,,
学位種別(和文)	博士論文
Type(English)	Doctoral Thesis

Characterization of local physicochemical properties of nano-sized materials by micro and nano-Raman spectroscopy

by

Maria Vanessa Cases Balois

Submitted to the Department of Electronic Chemistry
for the degree of

DOCTOR OF SCIENCE

at the

TOKYO INSTITUTE OF TECHNOLOGY

Table of Contents

Chapter 1: Introduction

Modern day computing is constantly getting smarter and faster because of the unrelenting rule of Moore's law – which states that the number of transistors that can be placed on an integrated circuit doubles approximately every two years. In order to keep pace, ingenious engineers have devised new methods to manipulate silicon (Si), such as strain engineering, and are constantly on the look out for unique materials that can be the next transistor channel, should Si reach its limit.

1.1. TRANSISTOR CHANNEL MATERIALS

1.1.1. Strained Silicon (ε-Si) Technology

Strain in semiconductors such as Si is important because it enhances device performance and reduces power consumption of electronic device [1.1]. Present-day transistors found in a computer's central processing unit (CPU) (Fig. 1.1) employ ε-Si as channel material using high amounts of strain and stress to increase carrier mobility [1.1, 1.2]. The increase in carrier mobility is mainly due to strain-induced band warping. By applying strain to Si, its crystal symmetry is broken causing the band edge energy to shift and altering the band structure away from the energy minimum. When more stress is applied along a low-symmetry axis, the crystal symmetry is further destroyed resulting to greater band warping compared to when stress is applied along a high symmetry axis [1.3]. Strain in silicon can be induced via heteroepitaxy, a process of growing a film whose equilibrium lattice constant is different from the substrate [1.4]. For tensile strained Si, a bulk-Si film is grown on top of a bulk-$Si_{1-x}Ge_x$ film (Fig. 1.2a). The lattice mismatch between Si and $Si_{1-x}Ge_x$ causes the tensile strain in the bulk-Si film (Fig. 1.2b). Compressive strain can also be induced using epitaxy by using a substrate that has a smaller lattice constant compared to Si. The manipulation of strain done through precise strain and stress nanoengineering has been used as a powerful strategy in fabrication and processing of variety of electronic, optoelectronic and photovoltaic devices [1.1, 1.5 – 1.11].

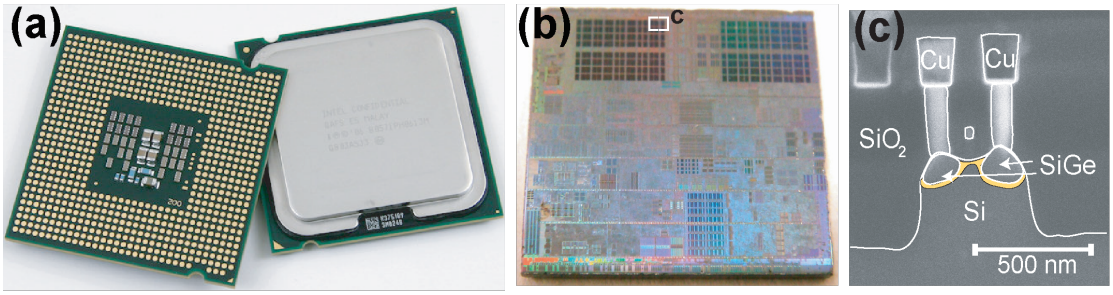

Figure 1.1. (a) Typical CPU with pins. **(b)** CPU without pins (removed by polishing). **(c)** Typical transistor in CPU located in the area indicated by the white square and point C in (b).

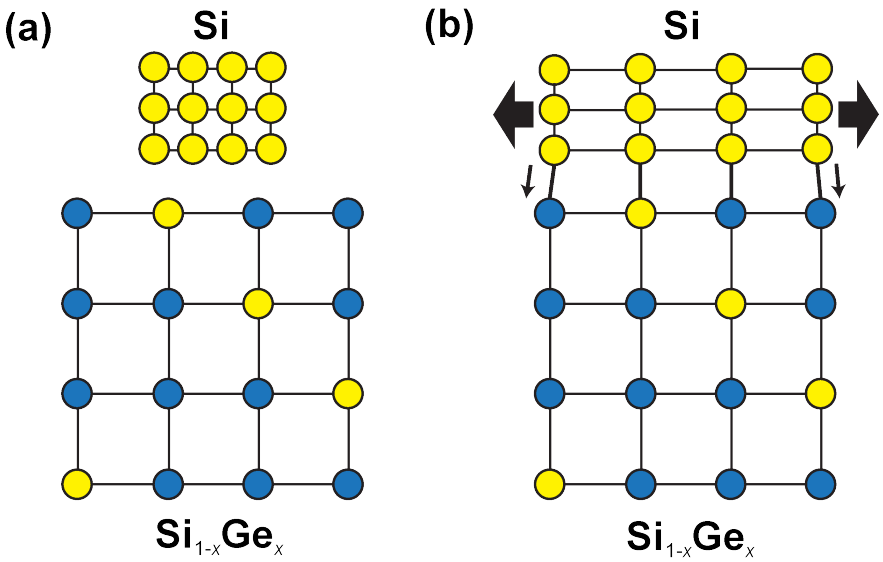

Figure 1.2. Illustration of applying strain to Silicon: **(a)** Bulk lattice constant of a bulk-Si film to be grown on top of a bulk-$Si_{1-x}Ge_x$ film and **(b)** the two films are placed together, wherein the top Si film is tensile strained.

Engineers are constantly shrinking the size of transistors leading to complex structures in order to accommodate Moore's law. As a consequence, the stress present in these structures is no longer isotropic / uniaxial but more anisotropic. In order to probe the stress and strain in the nanoscale, various characterization techniques have been developed. Each of these techniques suffers, however, a number of limitations such as being invasive or insensitive to all strain components, or having a limited spatial resolution. Transmission electron microscopy-based techniques, including among others holographic interferometry [1.12] and nanobeam electron beam diffraction, [1.13] provide the ultimate spatial resolution in mapping stress, but they are invasive, as they require a special sample preparation. This involves cutting the materials and thinning it down to ~100-500 nm, which can induce partial stress relaxation in addition to possible lattice local distortion during the analysis. X-ray-based techniques have immensely benefited from the availability of high-brilliance X-ray sources in the 3rd generation synchrotron sources or free

electron lasers leading to development of lensless coherent imaging and nanodiffraction techniques. These techniques have recently succeeded in mapping the stress in sub-micrometer structures and devices [1.13 – 1.19]. One such example of an effective X-ray-based technique was the use of X-ray nanodiffraction combined with finite element modeling in probing the local stress in single quantum dot-based devices [1.19]. However, they are still not yet ready for routine analyses because of the need for synchrotron facilities besides requiring special sample preparation to eliminate the background signal from the underlying substrate. Another technique that shows a lot of promise is micro-Raman spectroscopy, which is highly sensitive, nondestructive and simple to implement. The major drawback of this technique is its inability to measure the individual components of stress thus making the average stress value the only information accessible**. If the individual components of stress (in the *x*, *y*, and *z*-directions) can be measured, the actual stress rather than the average stress value can be determined.** Thus, providing a better understanding of the interplay between stress and basic properties and performance of strained semiconductors based nanoscale materials and devices.

1.1.2. Carbon Nanotubes: a Future Possibility

Moore's law is now slowly taking its toll on e-Si based transistors, presenting new problems as a consequence to transistor miniaturization such as current leakage and power wastage in the form of heat [1.20]. Preparing for the inevitable, scientists and engineers have been looking for alternative materials that are scalable and still follow Moore's law. A promising material is carbon nanotubes due to their superior electrical properties and ultrathin body [1.20 – 1.24]. CNTs have exhibited ballistic carrier transport and, due to their utlrathin body, are able to maintain gate control of current better than other competing structures, such as nanowires and fins - preventing short-channel effects [1.22]. There have already been studies on carbon nanotube transistors with sub-10 nm channel length [1.23]. And recently, the first CNT computer has been demonstrated by engineers from Stanford University [1.24]. The dimensions of single CNTs are typically 1 - 2 nm in diameter. To study these nano-sized structures, nano-Raman spectroscopy must be utilized. Function optimization can be realized through characterization of CNTs' local electronic properties via nano-Raman techniques such as TERS and tip-enhanced THz-Raman spectroscopy (TE-THzRS). Although nano-Raman spectroscopy is said to be non-invasive technique, it is not entirely true. In TERS, a strong localized optical field is generated at the apex of a metallic tip when illuminated [1.25]. This localized field produces

heat, which in turn can heat up the sample. Sample heating may affect its physical or chemical properties, which thus affects the analysis of the sample itself. For heat sensitive samples, heating may even cause sample damage. From this point of view, TERS can be classified as an invasive technique. **If the actual temperature generated by the localized optical field can be controlled, sensed and determined during TERS experiments, experimental parameters such as laser power and exposure time can be optimized in order not to damage or change the physical or chemical state of the sample.** Such kind of work can also be extended to studying temperature related behavior of the sample.

1.2. RAMAN SPECTROSCOPY AS A CHARACTERIZATION TECHNIQUE FOR NANO-SIZED MATERIALS

Raman spectroscopy is a vibrational spectroscopy that obtains direct information on the structure and orientation of molecules (in particular their vibrational structure) and crystals via molecular or lattice vibrations, respectively [1.26]. It is based on the inelastic scattering of a monochromatic excitation source, typically a laser. When inelastic scattering occurs, the energy of the incident photon is changed. The change in energy is manifested as a change in frequency of the scattered light relative to the incident light [1.27]. This phenomenon is called Raman scattering, which is based on the Raman effect.

1.2.1 The Raman Effect and Raman Scattering

The Raman effect is a phenomenon that results from the interaction of light and matter [1.28]. It was discovered by Chandrasekhara Venkata Raman [1.29] in 1928 in India. Raman's Nobel Prize winning discovery was motivated by his fascination with the beautiful blue color of the Mediterranean Sea while he was on a boat returning to India from England. He did not accept Lord Rayleigh's explanation that the blue color of the seawater was caused by reflection of light from the blue sky. This was because when he observed the blue seawater through a Nicol prism set at the Brewster angle (to eliminate reflected light from the seawater surface), the seawater was still blue. He then surmised that light scattering of the seawater caused the seawater to be blue [1.27, 1.30]. When he returned to India, he conducted an experiment using a focused beam of sunlight onto a liquid. He filtered the incident sunlight before the liquid with a green filter to produce a monochromatic light source. By placing a yellow

filter right after the sample, he then observed yellow light being scattered by the sample. This was evidence of the existence of inelastic scattering.

As mentioned earlier, inelastic scattering results in a change in frequency and energy between the incident and scattered photon. The change in frequency of the scattered photon can be either higher or lower than the incident photon, as shown in Fig. 1.3. Let ω_0 be the frequency of the incident photon with energy E_0 that encounters a molecule. From the photon-molecule interaction, the scattered photon is produced having a frequency ω_s and energy E_s. If the scattered photon loses energy to the molecule ($E_S < E_L$), the molecule is excited to a higher energy level, moving from the vibrational ground state, v = 0, to the first excited state, v = 1, of a vibrational mode. The vibrational energy would be $\hbar\omega_M = E_L - E_S$, where ω_M is associated to the frequency of the vibrational level. As a result, the frequency of the scattered photon will be lower than the incident photon ($\omega_s = \omega_0 - \omega_M$) and this is called **Stokes Raman scattering**. On the other hand, if the scattered photon gains energy from the molecule ($E_S > E_L$), the molecule relaxes from an excited vibrational state (v = 1) to the ground state (v = 0) with vibrational energy $\hbar\omega_M = E_S - E_L$. In this case, the frequency of the scattered photon will be higher than the incident photon ($\omega_s = \omega_0 + \omega_M$) and this is called **anti-Stokes Raman scattering**. For anti-Stokes Raman scattering to occur, the molecule must initially be in the excited vibrational state. This usually only occurs through thermal excitation, implying that at equilibrium the anti-Stokes signal depends on temperature (T) by the Boltzmann factor, $\exp\left[-\hbar\omega_M / \left(k_B T\right)\right]$. As a consequence, the anti-Stokes lines are much weaker than the Stokes lines and become exponentially weaker at higher vibrational energies [1.26, 1.30].

Another type of scattering occurs along with Raman scattering and this is **Rayleigh scattering**. Unlike Raman scattering, Rayleigh scattering is a type of elastic scattering. The incident photon does not lose nor gain energy from the molecule ($E_S = E_L$). Therefore, if the molecule was initially at the ground state, it will return to the ground state. The frequencies of the incident and the scattered photons are the same ($\omega_s = \omega_0$). In Raman spectroscopy, all three scattered photon frequencies – Rayleigh, Stokes and anti-Stokes – can be detected and recorded onto a spectrum

as shown in Fig. 1.4. The most intense peak is from Rayleigh scattering. Surrounding the Rayleigh peak are those of the Stokes and anti-Stokes peaks.

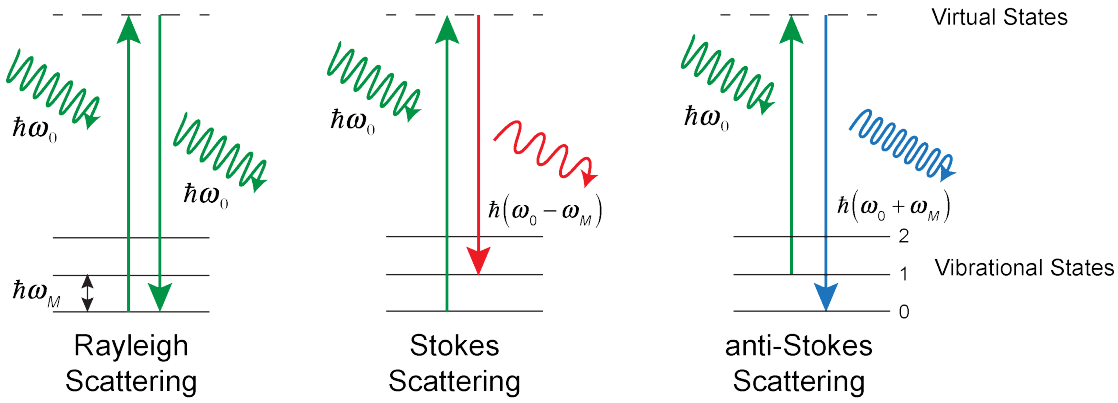

Figure 1.3. Energy diagram for Rayleigh, Stokes and anti-Stokes scattering.

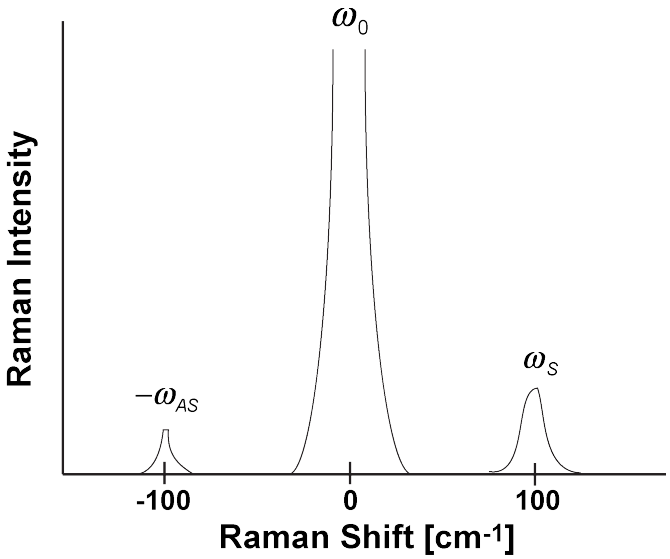

Figure 1.4. Raman spectra with Rayleigh, Stokes and anti-Stokes peaks.

There are two kinds of Raman spectroscopy techniques that can be used for characterization. These are micro-Raman spectroscopy and nano-Raman spectroscopy. Although both techniques rely on Raman scattering, their main difference is the attainable spatial resolution and is illustrated in Fig. 1.5.

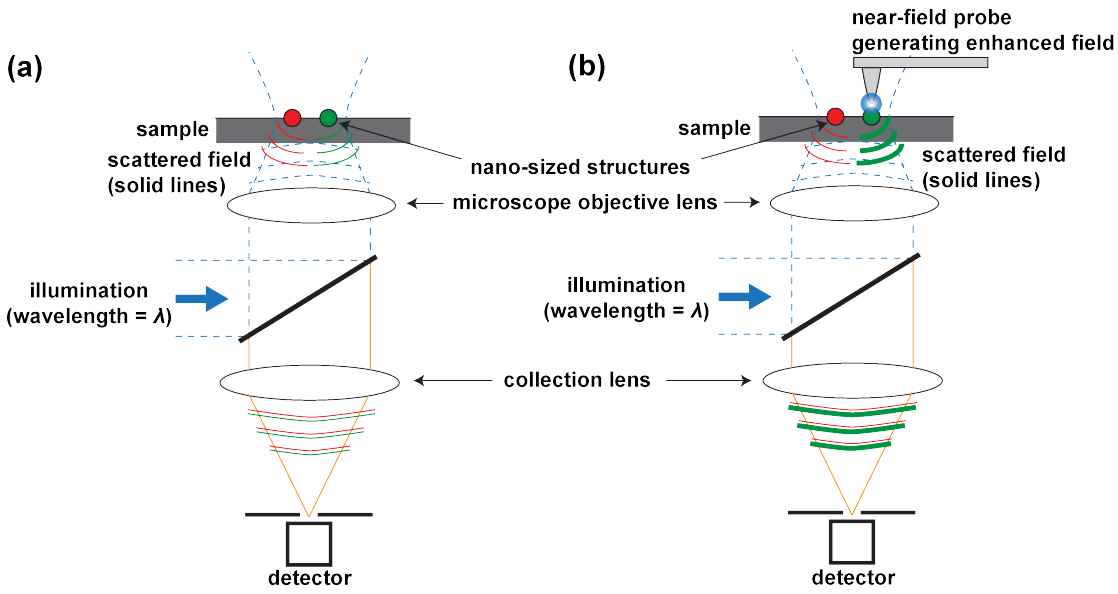

Figure 1.5. Configuration of (a) micro-Raman and (b) nano-Raman spectroscopic system.

1.2.2 Micro-Raman spectroscopy

In conventional Raman spectroscopy, laser light is focused onto the sample by a lens and detected by a spectrometer. Micro-Raman spectroscopy integrates a microscope that is coupled to a Raman spectrometer to acquire Raman spectra from microscopic samples. It is a sensitive and non-destructive technique that does not require any complex sample preparations [1.31]. Typically, a confocal microscope is used to attain higher resolution and contrast by introducing a pinhole that can spatially filter out unwanted stray light from out-of-focus regions of the sample [1.28]. However, the maximum spatial resolution that can be attained by a micro-Raman spectroscopy system cannot exceed the diffraction limit, given by

$$d = \frac{1.22\lambda}{NA}, \tag{1.1}$$

$$NA = n\sin\theta, \tag{1.2}$$

where d is the resolution length, λ is the wavelength of light, NA is the numerical aperture of the objective lens defined in Eq. (1.2), n is the index of refraction of the material being imaged and θ is the half-angle subtended by the objective lens [1.32]. Therefore, fine structures in the sample that are separated by less than a wavelength cannot be resolved (Fig. 1.5a). If there are nanoscale structures (red and green) in

the sample, the detected Raman signal would be the average of these two structures. The resolution of a micro-Raman system ranges from a few micrometers to hundreds of nanometers depending on the wavelength of light and the NA of the microscope objective. Micro-Raman spectroscopy is classified as a *far-field* technique because it is diffraction limited and the lens that illuminates and collects light from the sample is many wavelengths away from the sample.

1.2.3. Nano-Raman spectroscopy

To observe samples with nanoscale structures (typically only tens of nanometers in size), nano-Raman spectroscopy is necessary. In nano-Raman spectroscopy, a micro-Raman spectroscopy system is combined with probe-based techniques that can break the resolution barrier wherein the spatial resolution is dictated by the probe diameter (less than 100 nm). This technique is called *near-field* [1.33]. Near-field techniques use an optical probe that enhances the incident light and acts as a nano-light source. Using this nano-light source, it is possible to probe the individual structures in the sample and obtain information about that particular area of the sample, rather than an average of a large area, as is the case for micro-Raman spectroscopy. Higher spatial resolution is achieved and is dependent on the size of the optical probe (Fig. 1.5b). Prime examples of nano-spectroscopic techniques are: tip-enhanced Raman scattering (TERS) [1.34-1.36] to measure physical and chemical composition, and tip-scattering techniques using infrared light to measure electromagnetic field distributions [1.37].

1.3. THE SCOPE OF THIS THESIS

In this thesis, characterization and analysis of the local physicochemical properties of ε-Si and carbon nanotubes are conducted via micro and nano-Raman spectroscopy, respectively. Each technique had certain limitations that were overcome by the development of novel methods, which upon further improvement, can be utilized for characterization of actual transistors.

For ε-Si, the behavior of anisotropic stress relaxation upon nanopatterning for nanowire structures of various dimensions was investigated. Initially, micro-Raman spectroscopy using a backscattering geometry was insensitive to anisotropy. But through the use of a **high numerical aperture objective lens and polarized micro-Raman spectroscopy**, it is now possible to detect anisotropy.

For CNTs, the temperature change induced by nano-Raman techniques and the active control of temperature was studied. In order to determine the temperature and change in temperature at the sample, both the low frequency Stokes and anti-Stokes Raman (THz-Raman) intensities were detected. These intensities are related to the Raman shift and temperature via the Boltzmann distribution. THz-Raman detection was possible through the **development of a novel nano-Raman technique called tip-enhanced THz-Raman spectroscopy**.

1.3.1. The Remaining Chapters of this Thesis

In Chapter 2, the theoretical foundation on diffraction of focused electric fields across an interface for three different polarizations (linear, radial and azimuthal) is presented. This is essential in understanding the behavior of light as it moves from one medium to another, which is the case for any microscope-based system. The effect of polarization on the diffracted beam is also discussed. Through proper polarization control, it is possible to achieve better spatial resolution even though the system is still diffraction limited.

Chapters 3 and 4 focus on concepts and micro-Raman spectroscopy experiments related to ε-Si. Chapter 3 discusses the behavior of light as it is scattered by Si. It is shown theoretically and by numerical simulations that through the use a high numerical aperture lens and appropriate polarization it is possible to excite and

detect transverse optical phonon modes that are thought to be forbidden based on the Raman selection rules. Chapter 4 shows the first reported experimental observation of transverse optical modes from a ε-Si nanowire and nanomembrane samples. Stress analysis using longitudinal optical phonons and transverse optical phonons are made.

Chapter 5 and 6 focus on concepts and nano-Raman spectroscopy experiments related to carbon nanotubes. Chapter 5 discusses the theory and properties of carbon nanotubes and TERS. Chapter 6 discusses the theory of a novel temperature determination method by a nano-Raman spectroscopy technique, TE-THzRS. Experimental results are presented showing the potential of this technique to sense local temperature at the nanoscale and its possible applications.

Finally, Chapter 7 gives the summary and conclusions.

1.4 REFERENCES

[1.1] M. Chu, Y. Sun, U. Aghoram, and S.E. Thompson, *Annu. Rev. Mater. Res.* **39**, 203, 2009.

[1.2] S.E. Thompson, Uniaxial-Process-Induced Strained Si: Extending the CMOS Roadmap, *IEEE Transactions on Electron Devices*, **43**, 1010-1020, 2006.

[1.3] Y. Sun, S.E. Thompson, and T. Nishida, Physics of strain effects in semiconductors and metal-oxide-semiconductor field-effect transistors, *J. Appl. Phys.* **101**, 104503, 2007.

[1.4] C.K. Maiti, S. Chattopadhyay, and L.K. Bera, *Strained-Si heterostructure field effect devices*, Taylor and Francis: New York, 2007.

[1.5] Hashemi, P.; Gomez, L.; Hoyt, J. L. *IEEE Electron Device Lett.* **2009,** *30,* 401-403, DOI: 10.1109/LED.2009.2013877.

[1.6] Wu, Z.; Neaton, J. B.; Grossman, J. C. *Nano Lett.* **2009,** *9,* 2418-2422.

[1.7] Jacobsen, R. S.; Andersen, K. N.; Borel, P. I.; Fage-Pedersen, J.; Frandsen, L. H.; Hansen, O.; Kristensen, M.; Lavrinenko, A. V.; Moulin, G.; Haiyan, O.; Peucheret, C.; Zsigri, B.; Bjarklev, A. *Nature* **2006,** *441,* 199-202,

[1.8] Jain, J. R.; Hryciw, A.; Baer, T. M.; Miller, D. A. B.; Brongersma, M. L.; Howe, R. T. *Nature Photon.* **2012,** *6,* 398-405.

[1.9] Süess, M. J.; Minamisawa, R. A.; Schiefler G.; Frigerio, J.; Chrastina, D.; Isella, G.; Spolenak, R.; Faist, J.; Sigg, H. *Nature Photon.* **2013,** *7,* 466-472.

[1.10] Boucaud, P.; El Kurdi, M.; Sauvage, S.; de Kersauson, M.; Ghrib, A.; Checoury, X. *Nature Photon.* **2013,** *7,* 162.

[1.11] Minamisawa, R.; Süess, M. J.; Spolenak, R.; Faist, J.; David, C.; Gobrecht, J.; Bourdelle, K. K.; Sigg, H. *Nat. Commun.* **2012,** *3,* 1096.

[1.12] Hÿtch, M.; Houdellier, F.; Hüe, F.; Snoeck, E. *Nature* **2008,** *453,* 1086-1089.

[1.13] Hähnel, A.; Reiche, M.; Moutanabbir, O.; Blumtritt, H.; Geisler, H.; Höntschel J.; Engelmann, H. J. *Microsc. Microanal.* **2012,** *18,* 229-240.

[1.14] Newton, M. C.; Leake, S. J.; Harder, R.; Robinson, I. K. *Nature Mat.* **2010,** *9,* 120-124.

[1.15] Holt, M.; Harder, R.; Winarski, R.; Rose, V. *Annu. Rev. Mater. Res.* **2013,** *43,* 183-211.

[1.16] Godard, P.; Carbone, G.; Allain, M.; Mastropietro, F.; Chen, G.; Capello, L.; Diaz. A.; Metzger, T. H.; Stangl, J.; Chamard, V. *Nat. Commun.* **2011,** *2,* 568.

[1.17] Xiong, G.; Moutanabbir, O.; Huang, X.; Paknejad, S. A.; Shi, X.; Reiche, M.; Robinson, I. K. *Appl. Phys. Lett.* **2011,** *99,* 114103.

[1.18] Mastropietro, F.; Eymery, J.; Carbone, G.; Baudot, S.; Andrieu, F.; Favre-Nicolin, V. *Phys. Rev. Lett.* **2013,** *111,* 215502.

[1.19] Hrauda, N.; Zhang, J.; Wintersberger, E.; Etzelstorfer, T.; Mandl, B.; Stangl, J.; Carbone, D.; Holý, V.; Jovanović, V.; Biasotto, C.; Nanver, L. K.; Moers, J.; Grützmacher, D.; Bauer, G. *Nano Lett.* **2011,** *11*, 2875-2880.

[1.20] J. Appenzeller, Carbon nanotubes for high-performance electronics – progress and prospects, *Proceedings of the IEEE,* **96**, 201-211, 2008.

[1.21] P. Collins, M.S. Arnolds, and P. Avouris, Engineering Carbon nanotubes and nanotube circuits using electrical breakdown, *Science*, **292**, 706, 2001.

[1.22] A.D. Franklin, M. Luisier, S.J. Han, G. Tulevski, C.M. Breslin, L, Gignac, M.S. Lundstrom, and W. Haensch, Sub-10 nm Carbon nanotube transistor, *Nano Lett.* **12**, 758-762, 2012.

[1.23] S.J. Tans, A.R.M. Verschueren, and C. Dekker, Room-temperature transistor based on a single carbon nanotube, *Nature* **393**, 49, 1998.

[1.24] M.S. Shulaker, G. Hills, N. Patil, H. Wei, H.Y. Chen, H.S.P. Wong, and S. Mitra, Carbon nanotube computer, *Nature* **501**, 526, 2013.

[1.25] S. Kawata and V.M. Shalaev, *Tip enhancement*, Elsevier: The Netherlands, 2007.

[1.26] E. Le Ru and P. Etchegoin, *Principles of Surface-Enhanced Raman Spectroscopy and related plasmonic effects*, Elsevier: New York, 2008.

[1.27] S. Zhang, *Raman Spectroscopy and its Application in Nanostructures*, Wiley: New York, 2012.

[1.28] G. Turrell, J. Corset, *Raman Microscopy: developments and applications*, Elsevier, London, 1996.

[1.29] C.V. Raman and K.S. Krishnan, *Nature*, **121**, 501, 1928.

[1.30] D.A. Long, *The Raman Effect: a unified treatment of the theory of Raman scattering by molecules*, Wiley: New York, 2002.

[1.31] M. Becker, H. Scheel, S. Christiansen, and H.P. Strunk, Grain orientation, texture, and internal stress optically evaluated by micro-Raman spectroscopy, *J. Appl. Phys.* **101**, 063531, 2007.

[1.32] M. Born and E. Wolf, *Principles of Optics: Seventh (Expanded) Edition,* Cambridge University Press: New York, 2009.

[1.33] L. Novotny and B. Hecht, *Principles of Nano-Optics: Second Edition*, Cambridge University Press: New York, 2012.

[1.34] N. Hayazawa, Y. Inouye, Z. Sekkat, S. Kawata, *Optics Commun* 183, 333-336, 2000.

[1.35] R.M. Stöckle, Y.D. Suh, V. Deckert. R. Zenobi, *Chem Phys Lett* 318, 131-136, **2000**.

[1.36] M.S. Anderson, *Appl Phys Lett* 76, 3130, **2000**.

[1.37] M. Rang, A.C. Jones, F. Zhou, Z.Y. Li, J. Wiley, Y. Xia, M.B. Raschke, *Nano Lett* 8, 3357, **2008**.

Chapter 2: Properties of a Focused Three-Dimensional Electric Field across an Interface for Micro-Raman Spectroscopy

Knowledge of the diffracted-light distribution of focused electromagnetic fields plays an important role in various applications – from lens design to microscopy. These applications mainly deal with coherent beams strongly focused in the vicinity of planar interfaces. Such systems are common in biology and chemistry, wherein they use confocal microscopes with high numerical aperture (NA) objective lenses to focus light on a sample mounted on a glass slide. The sample usually has a different index of refraction than glass resulting to an interface. The interface itself can change various properties of the incident beam, such as the intensity of the individual components that make the beam [2.1]. These changes vary depending on the polarization of the incident beam. Exploring the behavior of light for different polarizations has been a topic of interest because through proper selection of incident polarization, it is possible to attain higher spatial resolution because of a tighter focus [2.2].

In this chapter, I discuss the properties of a focused electric field traversing an interface for different polarizations, namely, linear, radial and azimuthal. I begin with the theory of focusing light through a lens. A rigorous derivation on the mathematical representation of a diffracted focused field across an interface is shown. The derivations follow the formalism by Richards and Wolf [2.3]. After the derivations, I discuss and compare the electric field distributions in a simple glass/air system for each polarization that were computed via numerical simulations based on the equations derived. An air-glass system is used as proof of principle of the mathematical concepts explained. This is in preparation for Chapter 3 wherein a three-layer system consisting of oil/ε-Si/air is studied in detail.

2.1 FOCUSING AN ELECTRIC FIELD USING AN APLANATIC LENS

In order to thoroughly discuss focused electric fields across an interface, a theoretical understanding of how light is focused through an aplanatic lens is established. The discussion presented follows that of Novotny in Ref. 2.1.

Using geometrical optics, the fields near the optical lens can be represented mathematically. There are two rules that need to be followed when dealing with an aplanatic lens. These are 1) the sine condition and 2) the intensity law as shown in Fig. 2.1a and 2.1b, respectively. The sine condition states that the incident ray travelling parallel to the optical axis (also called the "conjugate ray") intersects with the refracted ray that emerges from or converges to the focus F of the aplanatic optical system on a sphere of radius *f* (called the Gaussian reference sphere), where *f* is the focal length of the lens. The height between the optical axis and the incident ray is:

$$h = f\sin\theta \tag{2.1}$$

where θ is the divergence angle of the incident ray. The behavior of the refracted optical rays is dictated by the sine condition. The intensity law states that the energy flux along each ray must remain constant. Thus, the energy entering the lens must be equal to the energy exciting the lens. The fields before and after refraction are related by

$$\left|\mathbf{E}_2\right| = \left|\mathbf{E}_1\right|\sqrt{\frac{n_1}{n_2}}\sqrt{\frac{\mu_2}{\mu_1}}\left(\cos\theta\right)^{1/2} \tag{2.2}$$

where the magnetic permeability is equal to one ($\mu = 1$) at optical frequencies. This is based on the power associated by a ray, $dP = \left(1/2\right)Z_{\mu\varepsilon}^{-1}\left|\mathbf{E}\right|^2 \mathrm{d}A$. $Z_{\mu\varepsilon}$ is the wave impedance and dA is an infinitesimal cross-section perpendicular to the ray propagation.

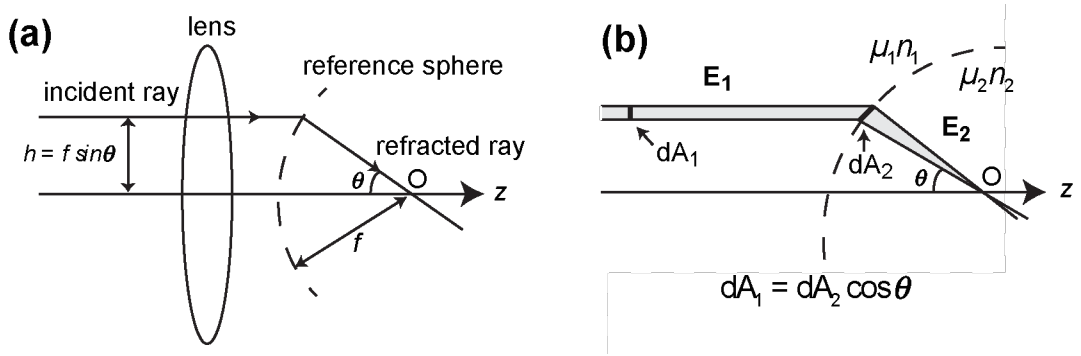

Figure 2.1. (a) The sine condition and (b) the intensity law of geometrical optics.

A geometrical representation of the aplanatic optical system is shown in Fig. 2.2. The focus is located at the origin $(x,y,z)=(0,0,0)$. To facilitate the discussion, the following definitions are made. $(x_\infty,y_\infty,z_\infty)$ is an arbitrary point on the surface of the reference sphere, while (x,y,z), an arbitrary field point near the focus. $\mathbf{n}_\rho$, $\mathbf{n}_\phi$, and $\mathbf{n}_\theta$ are unit vectors of a cylindrical coordinate system. $\mathbf{n}_\theta$ and $\mathbf{n}_\phi$ are unit vectors of a spherical coordinate system. The reference sphere of radius f refracts the incident rays. In doing so, it transforms a cylindrical coordinate system (incoming beam) into a spherical coordinate system (focused beam). In reality, these rays represent fields and if the incident field, $\mathbf{E}_{\mathbf{inc}}$, passes through the reference sphere, it is convenient to decompose the field into two components, $\mathbf{E}_{\mathbf{inc}}^{(s)}$ and $\mathbf{E}_{\mathbf{inc}}^{(p)}$. These represent the s-polarized and p-polarized vectors, respectively. From the unit vectors defined earlier, the two fields can be defined as

$$\mathbf{E}_{\mathbf{inc}}^{(s)}=\left[\mathbf{E}_{\mathbf{inc}}\bullet\mathbf{n}_\phi\right]\mathbf{n}_\phi,\qquad \mathbf{E}_{\mathbf{inc}}^{(p)}=\left[\mathbf{E}_{\mathbf{inc}}\bullet\mathbf{n}_\rho\right]\mathbf{n}_\rho. \tag{2.3}$$

The physical interpretation of Eq. (2.3) is $\mathbf{E}_{\mathbf{inc}}^{(s)}$ and $\mathbf{E}_{\mathbf{inc}}^{(p)}$ refract differently. $\mathbf{n}_\phi$ remains the same while $\mathbf{n}_\rho$, is mapped into $\mathbf{n}_\theta$. As the lens refracts the two fields, reflection and transmission occurs, for now, the only field of interest is the field transmitted through the lens. Hence, the total transmitted electric field, $\mathbf{E}_{\mathbf{FF}}$, is

$$\mathbf{E}_{\mathbf{FF}}=\left\{t_s\left[\mathbf{E}_{\mathbf{inc}}\bullet\mathbf{n}_\phi\right]\mathbf{n}_\phi+t_p\left[\mathbf{E}_{\mathbf{inc}}\bullet\mathbf{n}_\rho\right]\mathbf{n}_\theta\right\}\sqrt{\frac{n_1}{n_2}}\left(\cos\theta\right)^{1/2}. \tag{2.4}$$

where t_s and t_p are the Fresnel transmission coefficients defined as [2.4]:

$$t_s\left(k_x,k_y\right)=\frac{2\mu_2k_{z1}}{\mu_2k_{z1}+\mu_1k_{z2}},\qquad t_p\left(k_x,k_y\right)=\frac{2\varepsilon_2k_{z1}}{\varepsilon_2k_{z1}+\varepsilon_1k_{z2}}\sqrt{\frac{\mu_2\varepsilon_1}{\mu_1\varepsilon_2}}, \tag{2.5}$$

$$r_s\left(k_x,k_y\right)=\frac{\mu_2k_{z1}-\mu_1k_{z2}}{\mu_2k_{z1}+\mu_1k_{z2}},\qquad r_p\left(k_x,k_y\right)=\frac{\varepsilon_2k_{z1}-\varepsilon_1k_{z2}}{\varepsilon_2k_{z1}+\varepsilon_1k_{z2}}. \tag{2.6}$$

r_s and r_p are the Fresnel reflection coefficients which will be of much use in the latter part of this discussion. It has been defined here along with the transmission coefficients for ease of reference to the reader. Both transmission and reflection coefficients are functions of k_{z1} and k_{z2}. This implies that the coefficients can be

expressed in terms of the angle of incidence θ. The intensity law is obeyed by the presence of the $\sqrt{n_1 / n_2}\left(\cos\theta\right)^{1/2}$ factor.

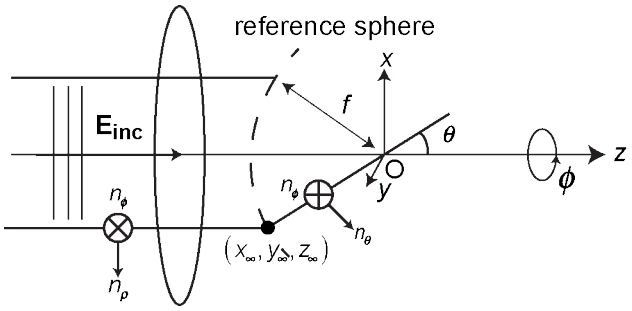

Figure 2.2. Aplanatic system and definition of the coordinates.

The unit vectors $\mathbf{n}_\rho$, $\mathbf{n}_\phi$, and $\mathbf{n}_\theta$ can now be expressed as Cartesian unit vectors $\mathbf{n}_x$, $\mathbf{n}_y$, and $\mathbf{n}_z$ using spherical coordinates θ and ϕ :

$$\mathbf{n}_\rho = \cos\phi\mathbf{n}_x + \sin\phi\mathbf{n}_y, \tag{2.7}$$

$$\mathbf{n}_\phi = -\sin\phi\mathbf{n}_x + \cos\phi\mathbf{n}_y, \tag{2.8}$$

$$\mathbf{n}_\theta = \cos\theta\cos\phi\mathbf{n}_x + \cos\theta\sin\phi\mathbf{n}_y - \sin\theta\mathbf{n}_z. \tag{2.9}$$

Substituting Eqs. (2.7) – (2.8) into Eq. (2.9),

$$\begin{aligned}\mathbf{E}_{\mathbf{FF}} = t_s\left(\theta\right)&\left[\mathbf{E}_{\mathbf{inc}}\left(\theta,\phi\right)\bullet\begin{pmatrix}-\sin\phi\\ \cos\phi\\ 0\end{pmatrix}\right]\begin{pmatrix}-\sin\phi\\ \cos\phi\\ 0\end{pmatrix}\sqrt{\frac{n_1}{n_2}}\left(\cos\theta\right)^{1/2}\\ +t_p\left(\theta\right)&\left[\mathbf{E}_{\mathbf{inc}}\left(\theta,\phi\right)\bullet\begin{pmatrix}\cos\phi\\ \sin\phi\\ 0\end{pmatrix}\right]\begin{pmatrix}\cos\phi\cos\theta\\ \sin\phi\cos\theta\\ -\sin\theta\end{pmatrix}\sqrt{\frac{n_1}{n_2}}\left(\cos\theta\right)^{1/2}.\end{aligned} \tag{2.10}$$

This field, $\mathbf{E}_{\mathbf{FF}}$, is the field to the right of the reference sphere of the aplanatic lens in Cartesian vector components form and is at the core of the calculations of the focal fields. As noted by Novotny, this field corresponds to the field on the surface of the reference sphere of the focusing lens.

2.2. DIFFRACTION OF A FOCUSED ELECTRIC FIELD ACROSS AN INTERFACE

Wolf presented an integral representation to obtain the electromagnetic field in the image space of an optical system that has only a single medium. His work was extended by Torok, et. al. [2.5] to an image space that had two media with different indices of refraction. The work of Torok is briefly summarized here and focuses only on the electric field, as it is of primary interest. For a full derivation including the magnetic field, the reader is encouraged to refer to these references [2.3, 2.5, 2,6, 2.7].

The optical system is illustrated in Figure 2.3 [adapted from Ref. 2.5 with permission from the Optical Society of America]. It is a system of revolution in a *(x, y, z)* rectangular coordinate system whose origin *O* is at the Gaussian focus and the optical axis is along *z*. All rays travel from the negative to positive *z* direction, unless indicated otherwise. The system consists of two media with refraction indices of n_1 and n_2 separated by a planar interface located $z = z_0$. A monochromatic point source is fixed in the object space at $z = -\infty$. It radiates a coherent beam that is focused by an aplanatic lens with aperture, Σ, producing a perfect converging spherical wave in image space. It is assumed that the lens is aberration free, since current real-life microscope objectives corrected for spherical aberration are well designed. Consider a point *V* in image space, at a certain time, *t*, where

$$\widetilde{\mathbf{E}}(V,t) = \mathrm{Re}\left[\mathbf{E}(V)\exp(-i\omega t)\right] \tag{2.11}$$

is the time-dependent electric field. The field of interest is the electric field vector **E**. It is generally complex and the Re denotes the real part. The location of V is defined by its position vector, $\mathbf{m_v}$ = (x, y, z), originating from O to V. Further, $\hat{s} = (s_x, s_y, s_z)$ represents a unit vector along a geometrical ray in image space.

The vector **E** satisfies the time-independent wave equation in homogeneous image space. It is assumed to be a superposition of plane waves and has an integral representation eloquently formalized by Wolf [2.6]

$$\mathbf{E}(V) = -\frac{ik}{2\pi}\iint_{\Omega}\frac{\mathbf{a}(s_x,s_y)}{s_z}\exp\left\{ik\left[\Phi(s_x,s_y)+\hat{s}\cdot\mathbf{m}_v\right]\right\}\times \mathrm{d}s_x\mathrm{d}s_y, \tag{2.12}$$

where **a** is the vector field amplitude [2.8]; Φ is the wave aberration function, which is zero in this case; Ω is the solid angle formed by all $\hat{s}$ geometrical rays in image space exiting through aperture Σ . The wavenumber is defined as

$$k = \frac{2\pi}{\lambda} = n\frac{2\pi}{\lambda_0} = nk_0 \tag{2.13}$$

where n is the refractive index of the medium in image space, and λ and λ_0 are the wavelengths in image and in vacuum, respectively. For $z < z_0$, the field is in material 1, so $k = k_1$, while for $z > z_0$, the field is in material 2, so $k = k_2$. Also, since the waves are homogeneous in image space:

$$s_z = +\sqrt{1 - s_x{}^2 - s_y{}^2} \quad \text{when} \quad s_x^2 + s_y^2 \le 1. \tag{2.14}$$

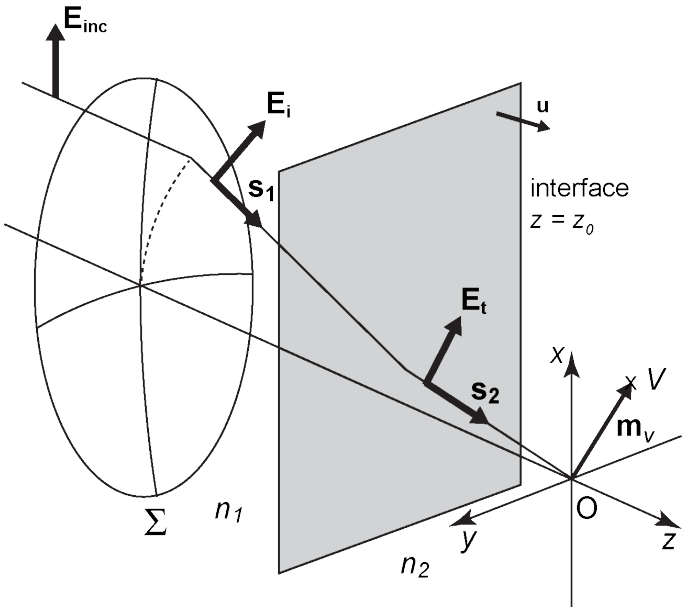

Figure 2.3. Schematic of an electric field focused across an interface between two different media.

A focused field $\mathbf{E_i}$ irradiates the interface from the left ($z < z_0$) at an angle of incidence, θ . The interface causes reflection and transmission to occur. Hence, the total field can be expressed as [2.1]

$$\mathbf{E} = \begin{cases} \mathbf{E_i} + \mathbf{E_r}, & z < z_0, \\ \mathbf{E_t}, & z > z_0, \end{cases} \tag{2.15}$$

where $\mathbf{E_r}$ and $\mathbf{E_t}$ are the reflected and transmitted fields, respectively. The refraction of a field at a planar interface is described by the Fresnel reflection (r_s, r_p) and transmission (t_s, t_p) coefficients. As discussed in Section 2.1, a field encountering a lens or interface can be decomposed into two components, $\mathbf{E}^{(s)}$ and $\mathbf{E}^{(p)}$, that results to

$$\mathbf{E} = \mathbf{E}^{(s)} + \mathbf{E}^{(p)} \tag{2.16}$$

Here, $\mathbf{E}^{(s)}$ is parallel to the interface and $\mathbf{E}^{(p)}$ is perpendicular to the wavevector **k** and $\mathbf{E}^{(s)}$. This decomposition has also been thoroughly explained in Section 2.1. $\mathbf{E_{FF}}$, Eq. (2.10), is the sum of the s- and p-polarized fields in terms of θ and ϕ. Although Eq. (2.10) describes a transmitted field, it can also describe a reflected field by simply changing the transmission coefficients into reflection coefficients.

2.2.1. Linear Polarization

Calculating for the incident electric field, $\mathbf{E_i}$. The derivation begins with solving for $\mathbf{E_i}$ in material 1. Eq. (2.12) can be rewritten to represent $\mathbf{E_i}$ as

$$\mathbf{E_i}\left(x,y,z\right) = -\frac{ik_1}{2\pi}\iint_{\Omega_1}\frac{\mathbf{E}_{\mathbf{FF},i}}{s_{1z}}\exp\left\{ik_1\left[s_{1x}x + s_{1y}y + s_{1z}z\right]\right\}\times \mathrm{d}s_{1x}\mathrm{d}s_{1y}, \tag{2.17}$$

where $\mathbf{E}_{\mathbf{FF},i}$ is the transmitted field right after the aplanatic lens and the term $\left(\widehat{s}_1\cdot\mathbf{m}_v\right)$ has been expanded. To get an expression for $\mathbf{E}_{\mathbf{FF},i}$, a few assumptions are made regarding the incoming wave, $\mathbf{E_{inc}}$, before the lens and the lens itself. Let $\mathbf{E_{inc}}$ be linearly polarized along the *x*-axis,

$$\mathbf{E_{inc}} = E_{\mathrm{inc}}\mathbf{n}_x. \tag{2.18}$$

Next it is assumed that the lens has a good antireflection coating, so that the Fresnel transmission coefficients are

$$t_s\left(\theta\right) = t_p\left(\theta\right) = 1. \tag{2.19}$$

Also, both sides of the lens are in the same medium. $\mathbf{E}_{\mathbf{FF},i}$ is represented as

$$\mathbf{E}_{\mathbf{FF},i}(\theta,\phi) = E_{\text{inc}}\left[\cos\phi\mathbf{n}_\theta - \sin\phi\mathbf{n}_\phi\right](\cos\theta)^{1/2}$$
$$= E_{\text{inc}}\begin{bmatrix} \cos\theta + \sin^2\phi(1-\cos\theta) \\ -(1-\cos\theta)\sin\phi\cos\phi \\ -\sin\theta\cos\phi \end{bmatrix}(\cos\theta)^{1/2}, \tag{2.20}$$

where the final expression is expressed in Cartesian vector components. $\mathbf{E}_{\mathbf{FF},i}$ is in terms of θ and ϕ because of the necessary coordinate transformations to project $\mathbf{E}_{\mathbf{FF},i}$ along unit vectors $\mathbf{n}_\theta$ and $\mathbf{n}_\phi$. Therefore, Eq. (2.16) must first be written in terms of spherical polar coordinates, r, θ, ϕ $\left(r > 0,\ 0 \le \theta \le \pi,\ 0 \le \phi \le 2\pi\right)$ as defined in Fig. 2.3:

$$s_{1x} = \sin\theta\cos\phi,\quad s_{1y} = \sin\theta\sin\phi,\quad s_{1z} = \cos\theta, \tag{2.21}$$

and because of symmetry, x, y, and z can be expressed as

$$x = \rho\cos\varphi,\quad y = \rho\sin\varphi,\quad z = z. \tag{2.22}$$

where ρ is the magnitude of vector $\mathbf{m}_\mathbf{v}$ and φ is the angle between the z-axis and vector $\mathbf{m}_\text{v}$.

Therefore,

$$s_{1x}x + s_{1y}y + s_{1z}z = \rho\sin\theta\cos(\phi - \varphi) + z\cos\theta. \tag{2.23}$$

The integral variables, $\mathrm{d}s_{1x}\mathrm{d}s_{1y} / s_{1z}$, must also be expressed in terms of θ and ϕ given by

$$\frac{\mathrm{d}s_{1x}\mathrm{d}s_{1y}}{s_{1z}} = d\Omega = \sin\theta\mathrm{d}\theta\mathrm{d}\phi, \tag{2.24}$$

where $\mathrm{d}\Omega$ is an element of the solid angle Ω.

Letting $E_{\text{inc}} = 1$ and, substituting Eqs. (2.20) to (2.24) into Eq. (2.17), the expression for $\mathbf{E}_\mathbf{i}$ in Cartesian components is:

$$\left.\begin{aligned}
E_{ix} &= -\frac{ik_1}{2\pi}\int_0^{\theta_{\max}}\int_0^{2\pi}\sqrt{\cos\theta}\sin\theta\left[\cos\theta+\left(1-\cos\theta\right)\sin^2\phi\right] \\
&\qquad\times\exp\left[ik_1\rho\sin\theta\cos\left(\phi-\varphi\right)\right]\exp\left[ik_1 z\cos\theta\right]\mathrm{d}\theta\mathrm{d}\phi, \\
E_{iy} &= \frac{ik_1}{2\pi}\int_0^{\theta_{\max}}\int_0^{2\pi}\sqrt{\cos\theta}\sin\theta\left(1-\cos\theta\right)\sin\phi\cos\phi \\
&\qquad\times\exp\left[ik_1\rho\sin\theta\cos\left(\phi-\varphi\right)\right]\exp\left[ik_1 z\cos\theta\right]\mathrm{d}\theta\mathrm{d}\phi, \\
E_{iz} &= \frac{ik_1}{2\pi}\int_0^{\theta_{\max}}\int_0^{2\pi}\sqrt{\cos\theta}\sin^2\theta\cos\phi \\
&\qquad\times\exp\left[ik_1\rho\sin\theta\cos\left(\phi-\varphi\right)\right]\exp\left[ik_1 z\cos\theta\right]\mathrm{d}\theta\mathrm{d}\phi,
\end{aligned}\right\} \quad (2.25)$$

where $\theta_{\max}$ is the maximum incident angle defined as $\mathrm{Arc\,Sin}(NA/n_1)$.

Equation (2.25) can be further simplified by expressing the ϕ integrals in terms of Bessel functions by the following formulae

$$\left.\begin{aligned}
\int_0^{2\pi}\cos n\phi\exp\left[iU\cos\left(\phi-\gamma\right)\right]\mathrm{d}\phi &= 2\pi i^n J_n\left(U\right)\cos n\gamma, \\
\int_0^{2\pi}\sin n\phi\exp\left[iU\cos\left(\phi-\gamma\right)\right]\mathrm{d}\phi &= 2\pi i^n J_n\left(U\right)\sin n\gamma.
\end{aligned}\right\} \quad (2.26)$$

where n is an integer and $J_n(U)$ is the Bessel function of the first kind and order n. A derivation of Eq. 2.26 is found in Ref. [2.3]. By using the double-angle identities:

$$\sin\phi\cos\phi = \frac{1}{2}\sin 2\phi \quad \text{and} \quad \sin^2\phi = \frac{1}{2}\left(1-\cos 2\phi\right), \quad (2.27)$$

and applying Eq. (2.23), the simplified expressions of each component of $\mathbf{E}_i$ at point V are:

$$\left.\begin{aligned}
E_{ix} &= -\frac{ik_1}{2}\left[I_{i0}+I_{i2}\cos\left(2\varphi\right)\right], \\
E_{iy} &= -\frac{ik_1}{2}\left[I_{i2}\sin\left(2\varphi\right)\right], \\
E_{iz} &= -k_1\left[I_{i1}\cos\varphi\right],
\end{aligned}\right\} \quad (2.28)$$

where the integrals I_{in} *(n = 0, 1, 2)* are grouped by Bessel function order:

$$\left.\begin{aligned} I_{i0} &= \int_0^{\theta_{\max}} \sqrt{\cos\theta}\,\sin\theta\left(1+\cos\theta\right)J_0\left(k_1\rho\sin\theta\right)\exp\left(ik_1 z\cos\theta\right)\mathrm{d}\theta, \\ I_{i1} &= \int_0^{\theta_{\max}} \sqrt{\cos\theta}\,\sin^2\theta J_1\left(k_1\rho\sin\theta\right)\exp\left(ik_1 z\cos\theta\right)\mathrm{d}\theta, \\ I_{i2} &= \int_0^{\theta_{\max}} \sqrt{\cos\theta}\,\sin\theta\left(1-\cos\theta\right)J_2\left(k_1\rho\sin\theta\right)\exp\left(ik_1 z\cos\theta\right)\mathrm{d}\theta. \end{aligned}\right\} \quad (2.29)$$

Calculating for the reflected electric field, $\mathbf{E}_r$. Now that an expression for $\mathbf{E}_i$ has been derived, an expression for $\mathbf{E}_r$ can be formulated. At the interface $\left(z = z_0\right)$ in material 1, the incident electric field $\mathbf{E}_i$ is

$$\mathbf{E}_i\left(x,y,z_0\right) = -\frac{ik_1}{2\pi}\iint_{\Omega_1}\frac{\mathbf{E}_{\mathbf{FF},i}}{s_{1z}}\exp\left\{ik_1\left[s_{1x}x + s_{1y}y + s_{1z}z_0\right]\right\}\times \mathrm{d}s_{1x}\mathrm{d}s_{1y}. \quad (2.30)$$

This field, obeying Fresnel's law of refraction, is reflected near the interface $\left(z = z_0 + \delta\right)$ and is expressed as

$$\mathbf{E}_r\left(x,y,z_0\right) = -\frac{ik_1}{2\pi}\iint_{\Omega_1}\mathbf{T}_r^{(e)}\frac{\mathbf{E}_{\mathbf{FF},i}}{s_{1z}}\exp\left\{ik_1\left[s_{1x}x + s_{1y}y + s_{1z}z_0\right]\right\}\times \mathrm{d}s_{1x}\mathrm{d}s_{1y} \quad (2.31)$$

for the case of $\delta \to 0$, wherein no sign change has occurred yet for s_{1z} since the field can still be considered approximately at the interface. $\mathbf{T}^{(e)}$ is an operator that modulates $\mathbf{E}_{\mathbf{FF},i}$ and is a function of the angle of incidence θ and n_1. The reflected field in material 1 can be represented as a superposition of plane waves and is a solution of the time-independent wave equation, given by:

$$\mathbf{E}_r\left(x,y,z\right) = -\frac{ik_1}{2\pi}\iint_{\Omega_1}\frac{\mathbf{E}_{\mathbf{FF},r}}{s_{1z}}\exp\left\{ik_1\left[s_{1x}x + s_{1y}y - s_{1z}z\right]\right\}\times \mathrm{d}s_{1x}\mathrm{d}s_{1y}. \quad (2.32)$$

Note that in Eq. (2.32), a change in sign of s_{1z} was made to ensure that the reflected field travels in the backward direction. Using Eq. (2.32) as a boundary condition at $z = z_0$ for Eq. (2.33), $\mathbf{E}_{\mathbf{FF},r}$ can be expressed as

$$\mathbf{E}_{\mathbf{FF},r} = \mathbf{T}_r^{(e)}\mathbf{E}_{\mathbf{FF},i}\exp\left[2ik_1 z_0\right]. \quad (2.33)$$

The factor $\mathbf{T}_r^{(e)}\mathbf{E}_{\mathbf{FF},i}$ is solved in the same manner as $\mathbf{E}_{\mathbf{FF},i}$. The field, however, is reflected by the interface. Therefore, the reflection of the s- and p-polarized components via the Fresnel reflection coefficients must be taken into consideration. It must be noted that all the Fresnel coefficients are functions of the incident angle, θ, such as $r_s(\theta)$. But the (θ) has been dropped for the sake of brevity. The factor $\mathbf{T}_r^{(e)}\mathbf{E}_{\mathbf{FF},i}$ is now defined as

$$\begin{aligned}\mathbf{T}_r^{(e)}\mathbf{E}_{\mathbf{FF},i} &= E_{inc}\left[-r_p\cos\phi\,\mathbf{n}_\theta - r_s\sin\phi\,\mathbf{n}_\phi\right](\cos\theta)^{1/2} \\ &= -E_{inc}\begin{bmatrix} r_p\cos\theta-(r_s+r_p\cos\theta)\sin^2\phi \\ (r_s+r_p\cos\theta)\sin\phi\cos\phi \\ -r_p\sin\theta\cos\phi \end{bmatrix}(\cos\theta)^{1/2}.\end{aligned} \tag{2.34}$$

Substituting Eq. (2.34) into Eq. (2.33), $\mathbf{E}_{\mathbf{FF},\mathbf{r}}$ is now

$$\mathbf{E}_{\mathbf{FF},r} = -E_{inc}\exp(2ik_1z_0)\begin{bmatrix} r_p\cos\theta-\sin^2\phi(r_s+r_p\cos\theta) \\ (r_s+r_p\cos\theta)\sin\phi\cos\phi \\ -r_p\sin\theta\cos\phi \end{bmatrix}(\cos\theta)^{1/2}. \tag{2.35}$$

Eqs. (2.35) and Eqs. (2.21) – (2.24) are then substituted into Eq. (2.32) and assuming $E_{\text{inc}}=1$,

$$\left.\begin{aligned} E_{rx} &= \frac{ik_1}{2\pi}\int_0^{\theta_{\max}}\int_0^{2\pi}\sqrt{\cos\theta}\sin\theta\left[r_p\cos\theta-(r_s+r_p\cos\theta)\sin^2\phi\right] \\ &\quad\times\exp\left[ik_1\rho\sin\theta\cos(\phi-\varphi)\right]\exp(-ik_1z\cos\theta)\exp(2ik_1z_0)\,\mathrm{d}\theta\mathrm{d}\phi, \\ E_{ry} &= \frac{ik_1}{2\pi}\int_0^{\theta_{\max}}\int_0^{2\pi}\sqrt{\cos\theta}\sin\theta(r_s+r_p\cos\theta)\sin\phi\cos\phi \\ &\quad\times\exp\left[ik_1\rho\sin\theta\cos(\phi-\varphi)\right]\exp(-ik_1z\cos\theta)\exp(2ik_1z_0)\,\mathrm{d}\theta\mathrm{d}\phi, \\ E_{rz} &= -\frac{ik_1}{2\pi}\int_0^{\theta_{\max}}\int_0^{2\pi}\sqrt{\cos\theta}\sin^2\theta(r_p)\cos\phi \\ &\quad\times\exp\left[ik_1\rho\sin\theta\cos(\phi-\varphi)\right]\exp(-ik_1z\cos\theta)\exp(2ik_1z_0)\,\mathrm{d}\theta\mathrm{d}\phi. \end{aligned}\right\} \tag{2.36}$$

Applying Eqs. (2.26) and (2.27) to Eq. (2.36), gives a representation of the individual components of $\mathbf{E}_r$.

$$\left.\begin{aligned} E_{rx} &= -\frac{ik_1}{2}\left[I_{r0} + I_{r2}\cos(2\varphi)\right] \\ E_{ry} &= -\frac{ik_1}{2}\left[I_{r2}\sin(2\varphi)\right] \\ E_{rz} &= k_1\left[I_{r1}\cos\varphi\right] \end{aligned}\right\} \tag{2.37}$$

where

$$\left.\begin{aligned} I_{r0} &= \int_0^{\theta_{\max}} \sqrt{\cos\theta}\sin\theta\left(r_s - r_p\cos\theta\right)J_0\left(k_1\rho\sin\theta\right) \\ &\quad \times \exp\left(-ik_1 z\cos\theta\right)\exp\left(2ik_1 z_0\right)\mathrm{d}\theta, \\ I_{r1} &= \int_0^{\theta_{\max}} \sqrt{\cos\theta}\sin^2\theta(r_p)J_1\left(k_1\rho\sin\theta\right) \\ &\quad \times \exp\left(-ik_1 z\cos\theta\right)\exp\left(2ik_1 z_0\right)\mathrm{d}\theta, \\ I_{r2} &= \int_0^{\theta_{\max}} \sqrt{\cos\theta}\sin\theta\left(r_s + r_p\cos\theta\right)J_2\left(k_1\rho\sin\theta\right) \\ &\quad \times \exp\left(-ik_1 z\cos\theta\right)\exp\left(2ik_1 z_0\right)\mathrm{d}\theta. \end{aligned}\right\} \tag{2.38}$$

Calculating for the transmitted electric field, $\mathbf{E}_t$. Next, the transmitted field, $\mathbf{E}_t$, is calculated. At the interface $\left(z = z_0\right)$ in material 1, the incident electric field $\mathbf{E}_i$ is given by Eq. (2.30). When the field is transmitted near the interface $\left(z = z_0 + \delta\right)$, it obeys Fresnel's law and is expressed as

$$\mathbf{E}_t\left(x,y,z_0\right) = -\frac{ik_1}{2\pi}\iint_{\Omega_1}\mathbf{T}^{(e)}\frac{\mathbf{E}_{\mathbf{FF},i}}{s_{1z}}\exp\left\{ik_1\left[s_{1x}x + s_{1y}y + s_{1z}z_0\right]\right\}\times \mathrm{d}s_{1x}\mathrm{d}s_{1y} \tag{2.39}$$

for the case of $\delta \to 0$. $\mathbf{T}^{(e)}$ is an operator that modulates the amplitude **a** and is a function of the angle of incidence θ and n_1 and n_2. The transmitted field in material 2 can be represented as a superposition of plane waves and is a solution of the time-independent wave equation, given by:

$$\mathbf{E}_t\left(x,y,z\right) = -\frac{ik_2}{2\pi}\iint_{\Omega_2}\frac{\mathbf{E}_{\mathbf{FF},t}}{s_{2z}}\exp\left\{ik_2\left[s_{2x}x + s_{2y}y + s_{2z}z\right]\right\}\times \mathrm{d}s_{2x}\mathrm{d}s_{2y}. \tag{2.40}$$

Note that in Eq. (2.40), the subscript 2 indicates that the transmitted field is in material 2. This now becomes a boundary condition problem wherein Eq. (2.40) must

satisfy the boundary condition imposed by Eq. (2.39). From the vectorial law of refraction, the relationship between $\widehat{s}_1$ and $\widehat{s}_2$ is [2.5]

$$k_2 s_{2x} = k_1 s_{1x}, \quad k_2 s_{2y} = k_1 s_{1y}. \tag{2.41}$$

A coordinate transformation is made for $\widehat{s}_2 = f\left(\widehat{s}_1\right)$. The Jacobian for this transformation is defined as

$$\mathbf{J}_0 = \frac{\partial\left(s_{2x}, s_{2y}\right)}{\partial\left(s_{1x}, s_{1y}\right)} = \left(\frac{k_1}{k_2}\right)^2, \tag{2.42}$$

which was obtained from Eq. (2.41). Equation (2.40) in terms of $\widehat{s}_1$ becomes

$$\begin{aligned}\mathbf{E}_t\left(x,y,z\right) = -\frac{ik_2}{2\pi}\iint_{\Omega_1}\mathbf{E}_{\mathbf{FF},t}\exp\left\{ik_1\left[s_{1x}x + s_{1x}y\right]\right\} \\ \times\exp\left(ik_2 s_{2z} z\right)\left(\frac{k_1}{k_2}\right)^2 \mathrm{d}s_{1x}\mathrm{d}s_{1y}.\end{aligned} \tag{2.43}$$

At $z = z_0$, Eq. (2.43) will satisfy the boundary condition, Eq. (2.39) when

$$\mathbf{E}_{\mathbf{FF},t} = \left(\frac{k_2}{k_1}\right)\mathbf{T}^{(e)}\frac{\mathbf{E}_{\mathbf{FF},i}}{s_{1z}}\exp\left[iz_0\left(k_1 s_{1z} - k_2 s_{2z}\right)\right]. \tag{2.44}$$

Substituting Eq. (2.44) into Eq. (2.43), the transmitted electric field $\mathbf{E}_t$ in material 2 is

$$\begin{aligned}\mathbf{E}_t\left(x,y,z\right) = -\frac{ik_2{}^2}{2\pi k_1}\iint_{\Omega_1}\mathbf{T}^{(e)}\frac{\mathbf{E}_{\mathbf{FF},i}}{s_{1z}}\exp\left[iz_0\left(k_1 s_{1z} - k_2 s_{2z}\right)\right] \\ \times\exp\left[ik_1\left(s_{1x}x + s_{1y}y\right)\right]\exp\left(ik_2 s_{2z} z\right)\mathrm{d}s_{1x}\mathrm{d}s_{1y}.\end{aligned} \tag{2.45}$$

The factor $\mathbf{T}^{(e)}\mathbf{E}_{\mathbf{FF},i}$ uses the same assumptions as when solving for $\mathbf{E}_{\mathbf{FF},i}$. The case of the transmitted field, has been derived in Section 2.1 and is given by Eq. (2.10). Solving for this equation gives

$$\mathbf{T}^{(e)}\mathbf{E}_{\mathbf{FF},i} = E_{inc}\left[\cos\phi t_p \mathbf{n}_\theta - \sin\phi t_s \mathbf{n}_\phi\right]\sqrt{\frac{n_1}{n_2}}\left(\cos\theta\right)^{1/2}$$
$$= E_{inc}\begin{bmatrix} t_p\cos\theta + \sin^2\phi\left(t_s - t_p\cos\theta\right) \\ -\left(t_s - t_p\cos\theta\right)\sin\phi\cos\phi \\ -t_p\sin\theta\cos\phi \end{bmatrix}\sqrt{\frac{n_1}{n_2}}\left(\cos\theta\right)^{1/2}. \quad (2.46)$$

Substituting Eqs. (2.46) and Eqs. (2.21) – (2.24) into Eq. (2.45) and assuming that $E_{inc} = 1$, $\mathbf{E_t}$ can be expressed as

$$\left.\begin{aligned} E_{tx} &= -\frac{ik_2^2}{2\pi k_1}\sqrt{\frac{n_1}{n_2}}\int_0^{\theta_{\max}}\int_0^{2\pi}\sqrt{\cos\theta}\sin\theta\left[t_p\cos\theta + \left(t_s - t_p\cos\theta\right)\sin^2\phi\right] \\ &\qquad \times\exp\left[ik_1\rho\sin\theta\cos\left(\phi-\varphi\right)\right]\exp\left(ik_2 z\cos\theta\right) \\ &\qquad \times\exp\left[iz_0\left(k_1\cos\theta - k_2\cos\theta\right)\right]\mathrm{d}\theta\mathrm{d}\phi, \\ E_{ty} &= \frac{ik_2^2}{2\pi k_1}\sqrt{\frac{n_1}{n_2}}\int_0^{\theta_{\max}}\int_0^{2\pi}\sqrt{\cos\theta}\sin\theta\left(t_s - t_p\cos\theta\right)\sin\phi\cos\phi \\ &\qquad \times\exp\left[ik_1\rho\sin\theta\cos\left(\phi-\varphi\right)\right]\exp\left(ik_2 z\cos\theta\right) \\ &\qquad \times\exp\left[iz_0\left(k_1\cos\theta - k_2\cos\theta\right)\right]\mathrm{d}\theta\mathrm{d}\phi, \\ E_{tz} &= \frac{ik_2^2}{2\pi k_1}\sqrt{\frac{n_1}{n_2}}\int_0^{\theta_{\max}}\int_0^{2\pi}\sqrt{\cos\theta}\sin^2\theta(t_p)\cos\phi \\ &\qquad \times\exp\left[ik_1\rho\sin\theta\cos\left(\phi-\varphi\right)\right]\exp\left(ik_2 z\cos\theta\right) \\ &\qquad \times\exp\left[iz_0\left(k_1\cos\theta - k_2\cos\theta\right)\right]\mathrm{d}\theta\mathrm{d}\phi. \end{aligned}\right\} \quad (2.47)$$

Applying Eqs. (2.26) and (2.27) to Eq. (2.47), gives a representation of the individual components of $\mathbf{E_t}$

$$\left.\begin{aligned} E_{tx} &= -\frac{ik_2^2}{2k_1}\sqrt{\frac{n_1}{n_2}}\left[I_{t0} + I_{t2}\cos\left(2\varphi\right)\right], \\ E_{ty} &= -\frac{ik_2^2}{2k_1}\sqrt{\frac{n_1}{n_2}}\left[I_{t2}\sin\left(2\varphi\right)\right], \\ E_{tz} &= -\frac{k_2^2}{k_1}\sqrt{\frac{n_1}{n_2}}\left[I_{i1}\cos\varphi\right], \end{aligned}\right\} \quad (2.47)$$

where

$$\left.\begin{aligned} I_{t0} &= \int_0^{\theta_{\max}} \sqrt{\cos\theta}\sin\theta\left(t_s + t_p\cos\theta\right)J_0\left(k_1\rho\sin\theta\right) \\ &\qquad \times \exp\left(ik_2 z\cos\theta\right)\exp\left[iz_0\left(k_1\cos\theta - k_2\cos\theta\right)\right]\mathrm{d}\theta, \\ I_{t1} &= \int_0^{\theta_{\max}} \sqrt{\cos\theta}\sin^2\theta(t_p)J_1\left(k_1\rho\sin\theta\right) \\ &\qquad \times \exp\left(ik_2 z\cos\theta\right)\exp\left[iz_0\left(k_1\cos\theta - k_2\cos\theta\right)\right]\mathrm{d}\theta, \\ I_{t2} &= \int_0^{\theta_{\max}} \sqrt{\cos\theta}\sin\theta\left(t_s - t_p\cos\theta\right)J_2\left(k_1\rho\sin\theta\right) \\ &\qquad \times \exp\left(ik_2 z\cos\theta\right)\exp\left[iz_0\left(k_1\cos\theta - k_2\cos\theta\right)\right]\mathrm{d}\theta. \end{aligned}\right\} \quad (2.48)$$

These equations along with Eqs. (2.28), (2.29), (2.37), and (2.38) are the necessary equations to visualize an electric field diffracted at an interface for linearly polarized illumination.

2.2.2. Radial Polarization

In studying radially and azimuthally polarized light, the same system described in Sections 2.1 and 2.2 is used along with the same geometry. But, the incident beam is expressed differently compared to linearly polarized light. The electric field prior to the lens is resolved into radial and azimuthal components [2.8 – 2.10],

$$\mathbf{E}_{\mathbf{inc}} = E_{inc,rad}\left(\cos\phi\mathbf{n}_x + \sin\phi\mathbf{n}_y\right) + E_{inc,azi}\left(-\sin\phi\mathbf{n}_x + \cos\phi\mathbf{n}_y\right). \quad (2.48)$$

For radially polarized light, the azimuthal component, $E_{inc,azi} = 0$ in Eq. (2.48). Therefore, the incident light is completely p-polarized. Using the same methodology in Section 2.2.1, the incident, reflected, and transmitted electric fields on the interface can be computed.

Incident electric field, $\mathbf{E}_{rad}$. The field right after the aplanatic lens, $\mathbf{E}_{\mathbf{FF},i,rad}$, using Eq. (2.48) as the field before the lens, is

$$\mathbf{E}_{\mathbf{FF},i,rad} = E_{inc,i,rad}\begin{bmatrix} \cos\theta\cos\phi \\ \cos\theta\sin\phi \\ -\sin\phi \end{bmatrix}\left(\cos\theta\right)^{1/2}. \quad (2.49)$$

From this point onwards, it is assumed that $E_{inc,i,rad} = 1$, the resulting incident electric field, $\mathbf{E_i}$, in individual Cartesian components is

$$\left.\begin{aligned} E_{ix,rad} &= -ik_1\left[iI_{i1,rad}\cos\varphi\right], \\ E_{iy,rad} &= -ik_1\left[iI_{i1,rad}\sin\varphi\right], \\ E_{iz,rad} &= ik_1\left[iI_{i0,rad}\sin\theta\right], \end{aligned}\right\} \tag{2.50}$$

where

$$\left.\begin{aligned} I_{i0,rad} &= \int_0^{\theta_{\max}} \left(\cos\theta\right)^{1/2}\sin\theta J_0\left(k_1\rho\sin\theta\right)\exp\left(ik_1 z\cos\theta\right)\mathrm{d}\theta, \\ I_{i1,rad} &= \int_0^{\theta_{\max}} \left(\cos\theta\right)^{3/2}\sin\theta J_1\left(k_1\rho\sin\theta\right)\exp\left(ik_1 z\cos\theta\right)\mathrm{d}\theta. \end{aligned}\right\} \tag{2.51}$$

Reflected electric field, $\mathbf{E}_{r,rad}$. The vector field amplitude $\mathbf{E}_{\mathbf{FF},\mathbf{r},rad}$, is expressed as

$$\mathbf{E}_{\mathbf{FF},\mathbf{r},rad} = -E_{inc,i,rad} r_p \begin{bmatrix} \cos\theta\cos\phi \\ \cos\theta\sin\phi \\ -\sin\phi \end{bmatrix} \left(\cos\theta\right)^{1/2}, \tag{2.52}$$

where the negative sign is a result of the reflection of the field and r_p is the Fresnel reflection coefficient. The field reflected by the interface, $\mathbf{E}_{r,rad}$, is

$$\left.\begin{aligned} E_{rx,rad} &= ik_1\left[iI_{r1,rad}\cos\varphi\right], \\ E_{ry,rad} &= ik_1\left[iI_{r1,rad}\sin\varphi\right], \\ E_{rz,rad} &= -ik_1\left[iI_{r0,rad}\sin\theta\right], \end{aligned}\right\} \tag{2.53}$$

where

$$\left.\begin{aligned} I_{r0,rad} &= \int_0^{\theta_{\max}} \left(\cos\theta\right)^{1/2}\sin\theta\left(r_p\right)J_0\left(k_1\rho\sin\theta\right)\exp\left(-ik_1 z\cos\theta\right)\exp\left(2ik_1 z_0\right)\mathrm{d}\theta, \\ I_{r1,rad} &= \int_0^{\theta_{\max}} \left(\cos\theta\right)^{3/2}\sin\theta\left(r_p\right)J_1\left(k_1\rho\sin\theta\right)\exp\left(-ik_1 z\cos\theta\right)\exp\left(2ik_1 z_0\right)\mathrm{d}\theta. \end{aligned}\right\} \tag{2.54}$$

Transmitted electric field, $\mathbf{E}_{t,rad}$. The vector field amplitude, $\mathbf{E}_{\mathbf{FF},\mathbf{t},rad}$, is expressed as

$$\mathbf{E}_{\mathbf{FF},\mathbf{t},rad} = E_{inc,i,rad} t_p \begin{bmatrix} \cos\theta\cos\phi \\ \cos\theta\sin\phi \\ -\sin\phi \end{bmatrix} \sqrt{\frac{n_1}{n_2}} \left(\cos\theta\right)^{1/2}. \tag{2.55}$$

The transmitted electric field diffracted across the interface, $\mathbf{E}_{t,rad}$, can now be expressed as

$$\left.\begin{aligned} E_{tx,rad} &= -\frac{ik_2^2}{k_1}\sqrt{\frac{n_1}{n_2}}\left[iI_{t1,rad}\cos\varphi \right], \\ E_{ty,rad} &= -\frac{ik_2^2}{k_1}\sqrt{\frac{n_1}{n_2}}\left[iI_{t1,rad}\sin\varphi \right], \\ E_{tz,rad} &= \frac{ik_2^2}{k_1}\sqrt{\frac{n_1}{n_2}}\left[iI_{t0,rad}\sin\theta \right], \end{aligned}\right\} \tag{2.56}$$

where

$$\left.\begin{aligned} I_{t0,rad} &= \int_0^{\theta_{\max}} \left(\cos\theta\right)^{1/2} \sin\theta\left(t_p\right) J_0\left(k_1\rho\sin\theta\right) \\ &\qquad \times \exp\left(ik_2 z\cos\theta\right)\exp\left[iz_0\left(k_1\cos\theta - k_2\cos\theta\right)\right]\mathrm{d}\theta, \\ I_{t1,rad} &= \int_0^{\theta_{\max}} \left(\cos\theta\right)^{3/2} \sin\theta\left(t_p\right) J_0\left(k_1\rho\sin\theta\right) \\ &\qquad \times \exp\left(ik_2 z\cos\theta\right)\exp\left[iz_0\left(k_1\cos\theta - k_2\cos\theta\right)\right]\mathrm{d}\theta. \end{aligned}\right\} \tag{2.57}$$

To construct the radial, azimuthal, and longitudinal components of the incident, reflected and transmitted fields, the following transformations are used [2.8]:

$$\left.\begin{aligned} E_{\rho,*} &= E_{jx,*}\cos\phi + E_{jy,*}\sin\phi, \\ E_{\phi,*} &= -E_{jx,*}\sin\phi + E_{jy,*}\cos\phi, \\ E_{z,*} &= E_{jz,*}, \end{aligned}\right\} \tag{2.58}$$

where ρ, ϕ, and z represent the radial, azimuthal and longitudinal components, respectively, and the * indicates the type of polarization – radial or azimuthal. For radial polarization, the $E_{\phi,rad} = 0$.

2.2.3. Azimuthal Polarization

For azimuthally polarized light, the radial component, $E_{inc,rad} = 0$ in Eq. (2.48). Therefore, the incident light is completely s-polarized. The mathematical representations of the incident, reflected, and transmitted electric fields on the interface are summarized below.

Incident electric field, $\mathbf{E}_{i,azi}$. The field right after the aplanatic lens, $\mathbf{E}_{\mathbf{FF},i,azi}$, using Eq. (2.48) as the field before the lens, is

$$\mathbf{E}_{\mathbf{FF},i,azi} = \begin{bmatrix} -\sin\phi \\ \cos\phi \\ 0 \end{bmatrix} \left(\cos\theta\right)^{1/2}. \tag{2.59}$$

The incident electric field, $\mathbf{E}_{i,azi}$, in Cartesian coordinates is

$$\left.\begin{aligned} E_{ix,azi} &= ik_1\left[iI_{i1,azi}\sin\varphi \right], \\ E_{iy,azi} &= -ik_1\left[iI_{i1,azi}\cos\varphi \right], \end{aligned}\right\} \tag{2.60}$$

where

$$I_{i1,azi} = \int_0^{\theta_{\max}} \left(\cos\theta\right)^{1/2} \sin\theta J_1\left(k_1\rho\sin\theta\right)\exp\left(ik_1 z\cos\theta\right)\mathrm{d}\theta. \tag{2.61}$$

Reflected electric field, $\mathbf{E}_{r,azi}$. The vector field amplitude, $\mathbf{E}_{\mathbf{FF},r,azi}$, is given by

$$\mathbf{E}_{\mathbf{FF},r,azi} = r_s \begin{bmatrix} -\sin\phi \\ \cos\phi \\ 0 \end{bmatrix} \left(\cos\theta\right)^{1/2}. \tag{2.62}$$

The resulting reflected electric field is

$$\left.\begin{aligned} E_{rx,azi} &= ik_1\left[iI_{r1,azi}\sin\varphi \right], \\ E_{ry,azi} &= -ik_1\left[iI_{r1,azi}\cos\varphi \right], \end{aligned}\right\} \tag{2.63}$$

where

$$I_{r1,azi} = \int_0^{\theta_{\max}} (\cos\theta)^{1/2} \sin\theta (r_s) J_1(k_1 \rho \sin\theta) \exp(-ik_1 z \cos\theta) \exp(2ik_1 z_0) \mathrm{d}\theta. \quad (2.64)$$

Transmitted electric field, $\mathbf{E}_{t,azi}$. The vector field amplitude, $\mathbf{E}_{\mathbf{FF},t,azi}$, is given by

$$\mathbf{E}_{\mathbf{FF},r,azi} = t_s \begin{bmatrix} -\sin\phi \\ \cos\phi \\ 0 \end{bmatrix} \sqrt{\frac{n_1}{n_2}} (\cos\theta)^{1/2}. \quad (2.65)$$

The transmitted electric field in Cartesian coordinates can be represented as

$$\left.\begin{aligned} E_{tx,azi} &= \frac{ik_2^2}{k_1} \sqrt{\frac{n_1}{n_2}} \left[iI_{r1,azi} \sin\varphi \right], \\ E_{ty,azi} &= -\frac{ik_2^2}{k_1} \sqrt{\frac{n_1}{n_2}} \left[iI_{r1,azi} \cos\varphi \right], \end{aligned}\right\} \quad (2.66)$$

where

$$\begin{aligned} I_{t1,azi} = \int_0^{\theta_{\max}} & (\cos\theta)^{1/2} \sin\theta J_1(k_1 \rho \sin\theta) \\ & \times \exp(ik_2 z \cos\theta) \exp\left[iz_0 (k_1 \cos\theta - k_2 \cos\theta) \right] \mathrm{d}\theta. \end{aligned} \quad (2.67)$$

As shown above, azimuthally polarized light has no longitudinal component and propagates as a purely transverse polarization field [2.8-2.9].

The results presented in this entire section can be extended to multi-layer interfaces by using generalized Fresnel reflection/transmission coefficients that take into consideration the entire structure of the media. The generalized Fresnel reflection coefficient between region *i* and region *i* + 1 for an *N*-layered medium is defined as [2.11]

$$\tilde{R}_{i,i+1} = \frac{R_{i,i+1} + \tilde{R}_{i+1,i+2} \exp\left[2ik_{i+1,z} (d_{i+1} - d_i) \right]}{1 + R_{i,i+1} \tilde{R}_{i+1,i+2} \exp\left[2ik_{i+1,z} (d_{i+1} - d_i) \right]}, \quad (2.68)$$

where d_i and d_{i+1} are the thicknesses of regions *i* and *i* + 1, respectively. The generalized transmission coefficient is defined as [2.11]

$$\tilde{T}_{1N} = \prod_{j=1}^{N-1} \exp\left[ik_{jz}\left(d_j - d_{j-1}\right)\right] S_{j,j+1}, \tag{2.69}$$

where $d_0 = d_1$ and $S_{j,j+1}$ has the form of

$$S_{i-1,i} = \frac{T_{i-1,i}}{1 - R_{i,i-1}\tilde{R}_{i,i+1}\exp\left[2ik_{iz}\left(d_i - d_{i-1}\right)\right]}. \tag{2.70}$$

The dummy indices are substituted from Eq. (2.68) into Eq. (2.69).

2.3. POLARIZATION DEPENDENCE OF A FOCUSED ELECTRIC FIELD ACROSS AN INTERFACE

From the theory discussed in the previous sections, the nature of the focused beam is different depending on the polarization of the incident beam. In this section, the behavior of the focused beam for the three types of polarizations by visualizing the diffracted electric field through numerical simulations is discussed. The equations used for the simulations are those derived in Section 2.2. A glass/air interface was chosen as proof-of-principle of the derived equations.

The numerical simulations model a system wherein a laser beam with a λ = 532 nm is focused by an aplanatic microscope objective lens with a NA of 1.49. A high NA (NA > 1) objective lens is chosen to obtain higher spatial resolution as compared to a low NA (NA < 1) objective lens. The focused beam illuminates glass/air interface (n_1 = 1.525, n_2 = 1) located at $z_0 = 0$. The polarization of the laser beam could be chosen to be linear, radial or azimuthal.

2.3.1. Linear Polarization

Figures 2.4a – 2.4b show a linearly polarized beam being focused on a glass/air interface. The distribution of the beam is different below the interface (glass) and above the interface (air). A standing wave pattern is observed in the glass material, which is a denser material compared to air. This pattern is due to the superposition of the incident and reflected plane wave components in the glass. It can also be observed that the reflected waves away from the focused spot are not transmitted across the interface. This is because the reflection at the interface is caused by total internal reflection, when the angle of incidence θ is larger than the critical angle θ_c. It is also observed that the profile of the focused spot is different in Fig. 2.4a

compared to Fig. 2.4b. This is because the focused spot is elliptical in shape, as shown in Fig. 2.4c. The focused spot is the sum of the $|\mathbf{E}_x|^2$, $|\mathbf{E}_y|^2$, and $|\mathbf{E}_z|^2$ fields (Figs. 2.4d – 2.4f). The strongest of the three components is E_x. The weakest of the three is the depolarized E_y component. However, the longitudinal field, E_z, has a relatively strong contribution to total field, being only half of E_x. There are two reasons why this is so. The first reason is the use of a high NA lens, which can aide in generating a stronger E_z field. The second reason is due to the presence of the interface. [2.1] The boundary conditions at the interface state that the transverse field components E_x and E_y must be continuous across the interface. The longitudinal field, however, scales as [2.1]

$$E_{z1}\varepsilon_1 = E_{z2}\varepsilon_2. \tag{2.71}$$

The longitudinal field is composed of two maxima. These two maxima are along the polarization direction, which in this case is the *x*-axis. Therefore, the resulting focused spot is elongated.

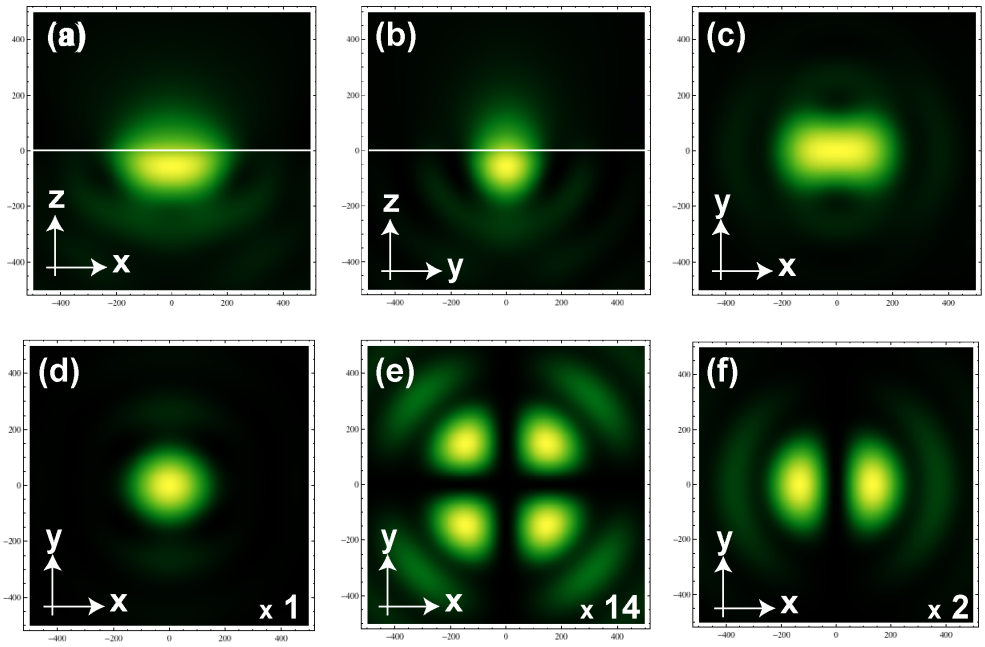

Figure 2.4 Electric field distribution of a linearly polarized beam focused by an aplanatic lens (NA = 1.49) on a glass/air interface (n_1 = 1.525, n_2 = 1). Each image has dimensions of 1 μm x 1 μm. Images (a) and (b) show a cross-sectional view of the field as it moves from glass (bottom) to air (top). The white horizontal indicates the interface located at $z_0 = 0$. The intensity of the (c) total electric field is composed of the (d) $|E_x|^2$, (e) $|E_y|^2$, and (f) $|E_z|^2$ components. Bright areas indicate high intensity and dark areas indicate low intensity.

2.3.2. Radial Polarization

Figures 2.5a and 2.5b show a focused radially polarized beam impinging on the glass/air interface. The transverse field or radial component has an on axis null through the focus. The longitudinal component, however, has a bright central spot at the focus. The reason is due to the distribution of each component. The radial component (Fig. 2.5c) has a donut-like shape as it propagates, wherein the center has zero intensity. This is a consequence of the beam being out of phase at opposite sides [2.9]. The longitudinal component, on the other hand, has a center lobe with high intensity that is surrounded by a halo of weaker intensity (Fig. 2.5d). Their phases are opposite causing a null area between them. Comparing the intensities of the radial and the longitudinal component, the longitudinal component is stronger than the radial component. This is because of the high NA of the objective lens.

For applications that utilize the longitudinal component to excite the sample, radial polarization is a good choice because of its intense single lobe feature. Linear polarization can also be used, but probing the sample would be more difficult due to the double lobes.

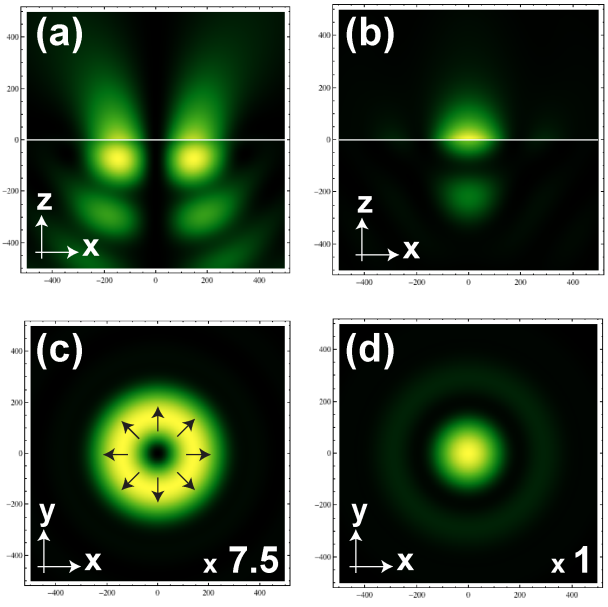

Figure 2.5 Electric field distribution of a radially polarized beam focused by an aplanatic lens (NA = 1.49) on a glass/air interface (n_1 = 1.525, n_2 = 1). Each image has dimensions of 1 μm x 1 μm. Cross-sectional views of the (a) transverse and (b) longitudinal fields as they move from glass (bottom) to air (top) are shown. The white horizontal indicates the interface located at $z_0 = 0$. The intensity distribution of the (c) transverse and (d) longitudinal fields in the x-y plane.

2.3.3. Azimuthal Polarization

The transverse field of azimuthally polarized light exhibits the same on axis null through the focus as shown in Fig. 2.6a. This is because transverse field exhibits the same donut-like shape as that of radially polarized light (Fig. 2.6b). Azimuthally polarized light, though, has no longitudinal component as shown in theory.

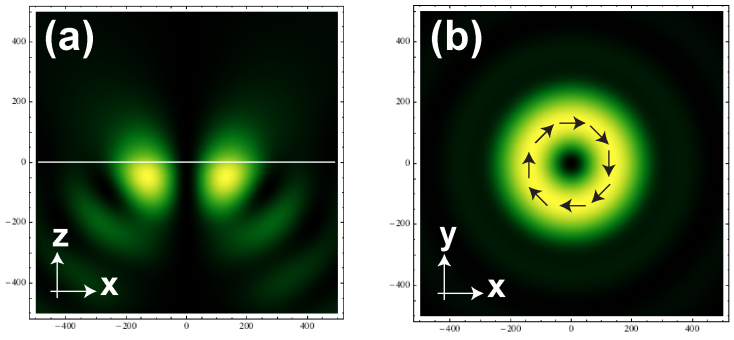

Figure 2.6 Electric field distribution of an azimuthally polarized beam focused by an aplanatic lens (NA = 1.49) on a glass/air interface (n_1 = 1.525, n_2 = 1). Each image has dimensions of 1 μm x 1 μm. Cross-sectional view of the (a) transverse field as it moves from glass (bottom) to air (top) are shown. The white horizontal indicates the interface located at $z_0 = 0$. The intensity distribution of the (c) transverse field in the x-y plane.

2.4. REFERENCES

[2.1] L. Novotny and B. Hecht, *Principles of Nano-Optics: Second Edition*, Cambridge University Press: New York, 2012.

[2.2] S. Quabis, R. Dorn, M. Eberler, O. Glöckl and G. Leuchs, Focusing light to a tighter spot, *Optics Communications* **179**, 1-7, 2000.

[2.3] B. Richards and E. Wolf, Electromagnetic diffraction in optical systems II. Structure of the image field in an aplanatic system, *Proceedings of the Royal Society A: Mathematical, Physical and Engineering Sciences,* **253**, 358-379, 1959.

[2.4] M. Born and E. Wolf, *Principles of Optics: Seventh (Expanded) Edition,* Cambridge University Press: New York, 2009.

[2.5] P. Török, P. Varga, Z. Laczik and G.R. Booker, Electromagnetic diffraction of light focused through a planar interface between amterials of mismatched refractive indices: an integral representation, *J. Opt. Soc. Am. A*, **12**, 325-332, 1995.

[2.6] E. Wolf, Electromagnetic diffraction in optical system I. An integral representation of the image field, *Proceedings of the Royal Society A: Mathematical, Physical and Engineering Sciences,* **253**, 349-357, 1959.

[2.7] J.J. Stamnes, *Waves in Focal Regions: propagation, diffraction and focusing of light, sound and water waves*, IOP Publishing Limited: Bristol, 1986.

[2.8] K.S. Youngworth and T.G. Brown, Focusing of high numerical aperture cylindrical-vector beams, *Optics Express*, **7**, 77-87, 2000.

[2.9] D.P. Biss and T.G. Brown, Cylindrical vector beam focusing through a dielectric interface, *Optics Express*, **9**, 490-497, 2001.

[2.10] L.E. Helseth, Roles of polarization, phase and amplitude in solid immersion lens systems, *Optics Communications*, **191**, 161-172, 2001.

[2.11] W.C. Chew, *Waves and Fields in Inhomogeneous Media*, IEEE Press: New York, 1995.

Chapter 3: Strained Silicon: a Theoretical Study

In the semiconductor industry, strained Silicon (ε-Si) is utilized in transistors by inducing strain to increase electron flow. This chapter discusses the relationship of strain and stress to the crystal structure and phonon modes of Si from a theoretical point of view. Phonon mode detection based on the Raman tensors is also explored. An experimental system using a backscattering geometry was modeled. The distribution of the electric field in the ε-Si sample is also discussed. Numerical simulations are conducted based on the equations derived in Chapter 2.

3.1. RAMAN SCATTERING IN CRYSTALS

Measuring the Raman spectrum of a crystal structure, such as silicon (Si), via micro-Raman spectroscopy, is one of the main methods for obtaining information about its lattice vibration frequencies [3.1]. These quantized lattice vibrations are called phonons [3.2-3.4] and mathematically expressed as [3.2]

$$Q_j = A_j \exp\left[\pm i\left(\boldsymbol{q}_j \cdot \boldsymbol{r} - \omega_j t\right)\right] \tag{3.1}$$

where Q_j is the normal coordinate of the vibration, A_j is a constant, $\boldsymbol{q_j}$ is the wavevector, $\boldsymbol{r}$ is the position vector, ω_j is the frequency at a time *t*. Raman scattering can occur when there is a change in the electrical susceptibility of the crystal, which is caused by lattice vibrations. The classical treatment of Raman scattering in crystals is explained in brief [3.2, 3.5]. An incident monochromatic light with frequency, ω_i, irradiates a crystal in a direction $\boldsymbol{k_i}$, generating an electric field, $\boldsymbol{E}$, at a point $\boldsymbol{r}$, expressed as

$$\boldsymbol{E} = E_0 \exp\left[i\left(\boldsymbol{k}_i \cdot \boldsymbol{r} - \omega_i t\right)\right]. \tag{3.2}$$

This electric field induces an electric moment *P* given by

$$P = \varepsilon_0 \chi \cdot E_0 \exp\left[i\left(\boldsymbol{k}_i \cdot \boldsymbol{r} - \omega_i t\right)\right] \tag{3.3}$$

where χ is the susceptibility tensor describing the response of the crystal to the electric field. The susceptibility can be expressed as a function of vibrations, having normal mode of vibration *j*,

$$\chi = \chi_0 + \left(\frac{\partial \chi}{\partial Q_j}\right)_0 Q_j + \left(\frac{\partial \chi}{\partial Q_j \partial Q_k}\right)_0 Q_j Q_k + \ldots \tag{3.4}$$

Combining Eqs. (3.3) and (3.4), we have

$$\boldsymbol{P} = \varepsilon_0 \chi_0 \cdot \boldsymbol{E}_0 \exp\left[i\left(\boldsymbol{k}_i \cdot \boldsymbol{r} - \omega_i t \right) \right] + \varepsilon_0 \chi_0 \cdot \boldsymbol{E}_0 \left(\frac{\partial \chi}{\partial Q_j} \right)_0 A_j \exp\left[-i\left(\omega_i \pm \omega_j \right) t \right] \exp\left[i(\boldsymbol{k}_i \pm \boldsymbol{q}_j) \cdot \boldsymbol{r} \right]. \quad (3.5)$$

This shows that, in a crystal, the induced moment will scatter light with three distinct frequencies: ω_i, Rayleigh scattering, $\omega_i + \omega_j$, anti-Stokes and $\omega_i - \omega_j$, Stokes Raman scattering. The anti-Stokes and Stokes propagate in the direction determined by $\boldsymbol{k}_i \pm \boldsymbol{q}_j$. The Raman effect will occur when ω_j is an optical frequency of the crystal.

The Raman scattering process observes the conservation of energy. More importantly, it also observes the conservation of momentum, as shown from our analysis above. As a consequence, lattice waves have directional properties. Hence, in crystals, the Raman spectrum is dependent on the orientation of the crystallographic axes with respect to the direction and polarization of both the excitation and the scattered light [3.5].

3.2. EXCITATION AND DETECTION OF PHONON MODES

In a cubic crystal of Si, there are three propagation directions of great interest. These are the [100], [110], and [111] directions corresponding to the cube edge, face diagonal, and body diagonal, respectively. When a wave travels along any of these directions, the phonons can be described to have longitudinal polarization (Fig. 3.1a) or transverse polarization (Fig. 3.1b) depending on whether their displacements are parallel or perpendicular to the direction of the wave vector [3.3, 3.6]. For Si, there are three optical phonon modes: one longitudinal optical (LO) phonon mode and two transverse optical (TO_1 and TO_2) modes, whose names describe their polarization. Physical observation of these phonon modes, in the form of scattered Raman intensity, is governed by the polarization selection rules dictated by the Raman tensors.

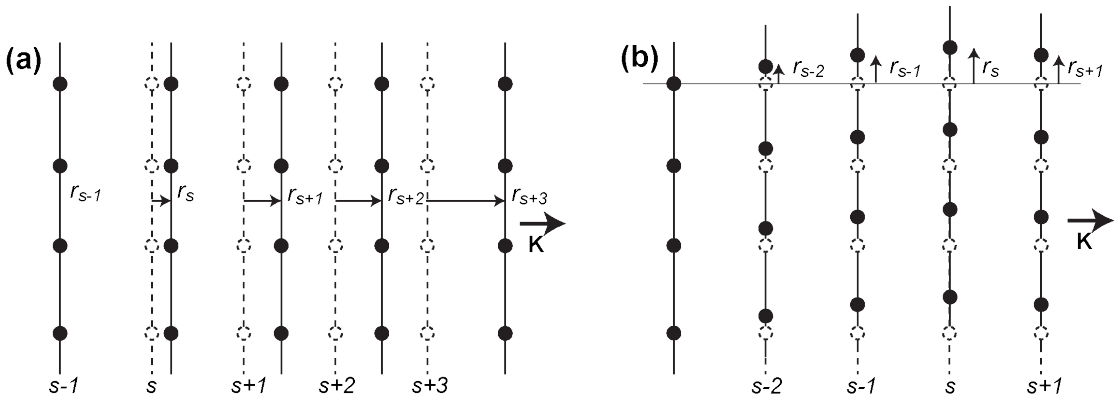

Figure 3.1. Displacement of atoms when encountering **(a)** longitudinal and **(b)** transverse waves. Dashed lines indicate planes of atoms when in equilibrium. Solid lines indicate displacement. The coordinate *r* is the measure of displacement of the planes. [Adapted from Ref. 3.3]

3.2.1. Silicon Raman Tensors in Crystal and Sample Coordinates

The intensity of scattered Raman light, I, is related to the Raman tensor R_j by [3.2]

$$I \propto \sum_j \left| e_s^T R_j e_i \right|^2, \tag{3.6}$$

where R_j is the Raman tensor for the j^{th} active phonon mode, $\mathbf{e_i}$ and $\mathbf{e_s}$ are the polarization unit vectors of the incident and scattered light, respectively. The superscript T indicates a transpose of the scattered electric field vector. The Raman tensors, R_j, for stress-free silicon were derived by Loudon [3.1] in the crystal coordinate system x = [100], y = [010], and z = [001]:

$$R_x = \begin{pmatrix} 0 & 0 & 0 \\ 0 & 0 & d \\ 0 & d & 0 \end{pmatrix}, \; R_y = \begin{pmatrix} 0 & 0 & d \\ 0 & 0 & 0 \\ d & 0 & 0 \end{pmatrix}, \; R_z = \begin{pmatrix} 0 & d & 0 \\ d & 0 & 0 \\ 0 & 0 & 0 \end{pmatrix}, \tag{3.7}$$

where d is a constant dependent on the Raman polarizability of the sample. For the micro-Raman experiments, a backscattering geometry is employed, wherein the incident laser beam is traveling along the +z-axis and the scattered light is collected in the –z direction by the same microscope objective lens. In the case of backscattering from a (001) surface, R_x and R_y are the Raman tensors corresponding to TO_1 and TO_2 phonons, respectively, while R_z corresponds to LO phonon. These assignments are relative and depend on the surface from which scattering is observed (e.g. in backscattering from a (100) surface, R_x corresponds to the LO phonon [3.2]).

In this study, the edges of the nanowire are aligned along the [110] direction. Thus, the Si Raman tensors expressed in the crystal axes (*x, y, z*) need to be transformed to the sample coordinate (*x', y', z'*) axes using the tensor rotation, wherein the sample is rotated 45° from the crystal axes (Figure 3.2). For the sample coordinate axes, the Raman tensors are [3.7]:

$$R_{x'} = \frac{1}{\sqrt{2}}\begin{pmatrix} 0 & 0 & d \\ 0 & 0 & d \\ d & d & 0 \end{pmatrix}, \quad R_{y'} = \frac{1}{\sqrt{2}}\begin{pmatrix} 0 & 0 & d \\ 0 & 0 & -d \\ d & -d & 0 \end{pmatrix}, \quad R_{z'} = \begin{pmatrix} d & 0 & 0 \\ 0 & -d & 0 \\ 0 & 0 & 0 \end{pmatrix}. \quad (3.8)$$

From the polarization selection rule, Eq. (3.6), and the Raman tensors, only the LO phonons (R_z and $R_{z'}$) can be observed for backscattering geometry along the z and z'-axes in both crystal and sample coordinate system. On the other hand, TO phonon modes, theoretically, cannot be detected when using the same backscattering configuration.

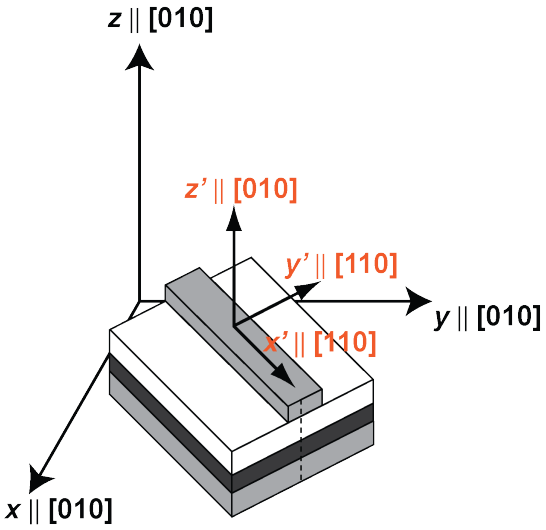

Figure 3.2. Crystal (x, y, z) and sample (x', y', z') coordinate systems. The sample coordinate system is rotate 45° around the z-axis with respect to the crystal coordinate system [Adapted from Ref. 3.8 with permission from ACS Publications].

To facilitate the discussion of the polarization and scattering configuration from the Si crystal, we shall use the Porto notation for the rest of this text, e.g. [3.9]

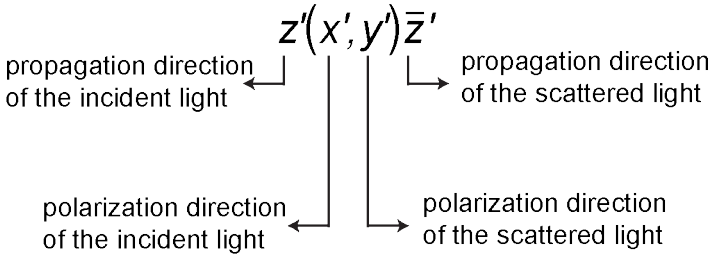

The bar on top of the propagation direction indicates backscattering geometry.

3.2.2. Using a High Numerical Aperture Objective Lens to Excite Transverse Optical Phonon Modes

From the discussion in the previous section, TO phonon modes cannot be detected, in theory, because the backscattering geometry limits the excitation polarization only to x'- or y'-polarization. If it were possible to generate z'-polarization, then TO phonon modes can be detected. A solution to this problem would be the utilization of a high NA objective lens.

For a low NA lens, Raman intensity calculation is typically based on the simplified Raman signal collection efficiency (e_i and e_s) from *x'*- or *y'*- polarization. The *z'*-polarization is ignored, whereas the *x'*- and *y'*- polarizations are set either to unity (detectable) or zero (undetectable) depending on the analyzer setting. It was found, however, that when the NA of the objective lens is sufficiently high (i.e., NA > 1.0), the *z*'- component is no longer negligible, making it possible to detect the TO phonon [3.10, 3.11]. Moreover, the depolarized (*y'*-component) light at the focus also increases and becomes comparable to the *z'*-component for linearly *x'*-polarized incident light as shown in Fig. 3.3. Therefore, contributions from the depolarized light cannot be ignored in the analysis of the scattered Raman signal. The configuration $z'(x',y')\bar{z}'$ is an example for this case in polarized micro-Raman spectroscopy.

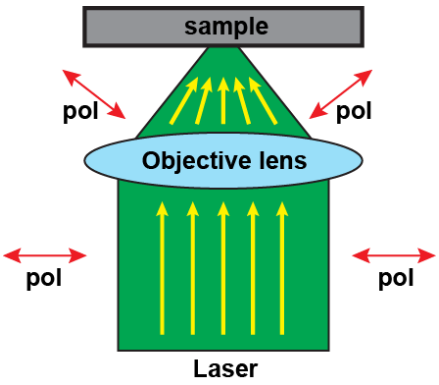

Figure 3.3. Change in polarization due to high NA objective lens.

3.2.3. Importance of Transverse Optical Phonon Mode Detection for Stress Determination in Silicon

The phonon mode frequencies of crystalline Si are selectively modified when Si is subjected to mechanical stress or strain [3.2]. Figure 3.4a – c illustrates the phonon modes at different stress states. When no strain is present (Fig. 3.4a), only a single triply degenerated phonon mode can be detected [3.8], which, in the case of (001)-oriented Si surface, has a peak frequency of about $\omega_0 \approx 520$ cm^{-1} at room temperature [3.2]. In the presence of a bi-isotropic in-plane strain ($\varepsilon'_{xx} = \varepsilon'_{yy}$), however, the degeneracy is lifted and the original single phonon will split into two (Fig. 3.4b): the singlet LO and the doublet TO. When anisotropic strain ($\varepsilon'_{xx} \neq \varepsilon'_{yy}$) is present, the doublet TO further splits into two singlet phonon modes (Fig. 3.4c) resulting to three phonon modes in total. To get a complete picture of stress experienced by a Si structure, such as ε-Si, all three phonon modes must be measured, either individually or collectively. It is theoretically possible to detect all three phonon modes either when the incident or scattered electric fields are not parallel to the sample surface or when the sample surface is not (001)-oriented [3.4, 3.12]

The three optical phonon modes in the presence of strain can be obtained by solving the secular equation [3.2, 3.13]:

$$\begin{vmatrix} p\varepsilon_{11}+q\left(\varepsilon_{22}+\varepsilon_{33}\right)-\lambda & 2r\varepsilon_{12} & 2r\varepsilon_{13} \\ 2r\varepsilon_{12} & p\varepsilon_{22}+q\left(\varepsilon_{33}+\varepsilon_{11}\right)-\lambda & 2r\varepsilon_{23} \\ 2r\varepsilon_{13} & 2r\varepsilon_{23} & p\varepsilon_{33}+q\left(\varepsilon_{11}+\varepsilon_{22}\right)-\lambda \end{vmatrix} = 0, \quad (3.9)$$

where *p, q,* and *r* are the phonon deformation potentials (PDP) related to the material and ε_{ij} are the components of the strain tensor. Following the formalism of de Wolf [3.2], the eigenvalues λ_j are defined as

$$\lambda_j = \omega_j^2 - \omega_{j0}^2 \tag{3.10}$$

$$\Delta\omega_j = \omega_j - \omega_{j0} \approx \frac{\lambda_j}{2\omega_{j0}}. \tag{3.11}$$

Here, ω_j (j = 1, 2, 3) and ω_{j0} represent the Raman frequencies in the presence and absence of stress, respectively. Hooke's Law relates the strain tensors, ε'_{ijkl}, to the stress tensors, σ'_{ijkl}, represented as

$$\sigma'_{ij} = \sum_{ijkl} c'_{ijkl}\,\varepsilon'_{kl}, \tag{3.12}$$

where c'_{ijkl} is the stiffness tensor. This serves as the starting point for calculating the stress in ε-Si nanostructures, which will be discussed further in Chapter 4.

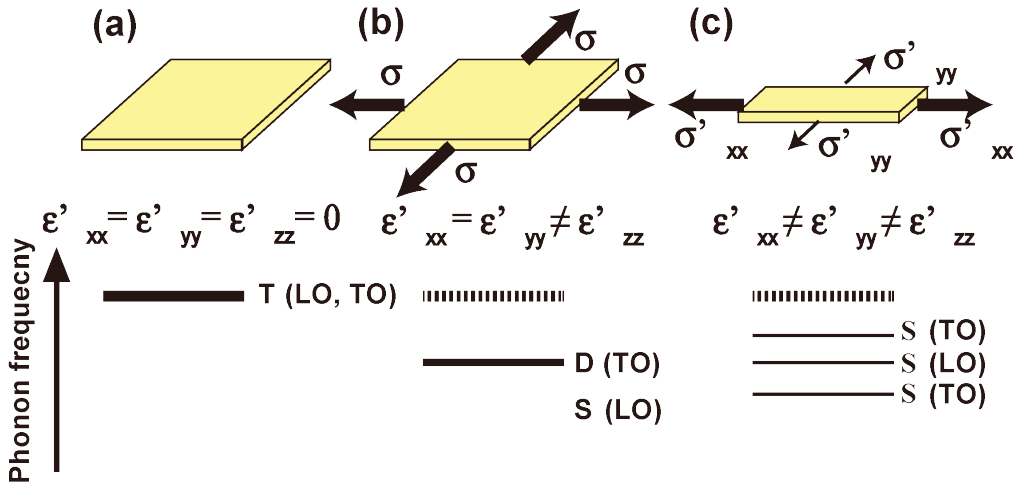

Figure 3.4. Phonon mode splitting for various types of induced strain. **(a)** In the absence of strain, the detected phonon frequency is triply degenerate, consisting of the LO and TO phonon modes. **(b)** In the case of bi-isotropic strain (nanomembrane), the triply degenerate mode is split into two singlet LO and doublet TO. **(c)** When anisotropic strain is present, the doublet TO is further split into two singlet TO phonon modes resulting to three phonon modes in total: one singlet LO and two singlet TO. [Taken from Ref. 3.8 with permission from ACS Publications.]

3.3. THREE-DIMENSIONAL ELECTRIC FIELD CALCULATIONS: POLARIZATION DEPENDENCE

To accurately describe the scattering process involving illumination and collection by a high NA lens (NA > 1), the e_i cannot be assumed to be constant across the focal volume. Considering all the non-negligible effects discussed in Section 3.2.2., the intensity of the Raman mode can be rewritten as [3.10]:

$$I_i = I_0 \sum_i \int_0^{2\pi} \int_0^{\theta_{max}} \left| \left[R(\alpha,\beta,\gamma) \begin{pmatrix} E_{scaX}(\theta,\phi,\eta) \\ E_{scaY}(\theta,\phi,\eta) \\ E_{scaZ}(\theta,\phi,\eta) \end{pmatrix} \right]^T \times \left[R_i \bullet R(\alpha,\beta,\gamma) \begin{pmatrix} E'_x \\ E'_y \\ E'_z \end{pmatrix} \right] \right|^2 \sin\theta \, d\theta \, d\phi \tag{3.13}$$

where I_0 is the incident intensity, η is the angle of the analyzer with respect to the x'–axis, and θ and ϕ are the polar and azimuthal angles, respectively. E'_x, E'_y and E'_z are the incident electric fields in the crystal coordinate system (x,y,z). R_i is the Raman tensor also in the crystal coordinate system, which is transformed into the sample coordinate system (x',y',z') using the Euler rotation matrix [3.14], $R(\alpha,\beta,\gamma)$, defined as:

$$R(\alpha,\beta,\gamma) = \begin{pmatrix} \cos\alpha\cos\gamma - \sin\alpha\cos\beta\sin\gamma & -\cos\alpha\sin\gamma - \sin\alpha\cos\beta\cos\gamma & \sin\alpha\sin\beta \\ \sin\alpha\cos\gamma + \cos\alpha\cos\beta\sin\gamma & -\sin\alpha\sin\gamma + \cos\alpha\cos\beta\cos\gamma & -\cos\alpha\sin\beta \\ \sin\beta\sin\gamma & \sin\beta\cos\gamma & \cos\beta \end{pmatrix} \tag{3.14}$$

As discussed in Chapter 2, the incident electric field, E_i, can be generated numerically for different kinds of polarization. When linearly polarized light, $\mathbf{E}'_{Lin} = (x',y',z',d)$, is focused onto ε-Si, the electric field distribution within the ε-Si is represented as [3.15 – 3.21]:

$$\mathbf{E}'_{Lin}(x',y',z',d) = \begin{bmatrix} -i\{F_0(x',y',z',d) + F_2(x',y',z',d)\} \\ -iF_2(x',y',z',d)\dfrac{2x'y'}{x'^2+y'^2} \\ -2F_1(x',y',z',d)\dfrac{x'}{\sqrt{x'^2+y'^2}} \end{bmatrix} \tag{3.15}$$

where $F_0(x',y',z',d)$, $F_1(x',y',z',d)$, and $F_2(x',y',z',d)$ are written as

$$F_0(x',y',z',d)=\int_{\theta_{\min}}^{\theta_{\max}}\sqrt{\cos\theta}\sin\theta J_0\left(k_{x'1}(\theta)\sqrt{x'^2+y'^2}\right)\times$$
$$\left\{\begin{array}{l}\left(t_{p01}(\theta,d)\sqrt{1-\left(\frac{\sqrt{\varepsilon_0}}{\sqrt{\varepsilon_1}}\sin\theta\right)^2}+t_{s01}(\theta,d)\right)\exp\left[ik_{z'1}(\theta)z'\right]+\\ \left(-r_{p01}(\theta,d)\sqrt{1-\left(\frac{\sqrt{\varepsilon_0}}{\sqrt{\varepsilon_1}}\sin\theta\right)^2}+r_{s01}(\theta,d)\right)\exp\left[-ik_{z'1}(\theta)z+2idk_{z'1}(\theta)\right]\end{array}\right\}d\theta \quad (3.16)$$

$$F_1(x',y',z',d)=\int_{\theta_{\min}}^{\theta_{\max}}\sqrt{\cos\theta}\sin^2\theta\frac{\sqrt{\varepsilon_0}}{\sqrt{\varepsilon_1}}J_1\left(k_{x'1}(\theta)\sqrt{x'^2+y'^2}\right)\times$$
$$\left\{t_{p01}(\theta,d)\exp\left[ik_{z'1}(\theta)z'\right]-r_{p01}(\theta,d)\exp\left[-ik_{z'1}(\theta)z'+2idk_{z'1}(\theta)\right]\right\}d\theta \quad (3.17)$$

$$F_2(x',y',z',d)=\int_{\theta_{\min}}^{\theta_{\max}}\sqrt{\cos\theta}\sin\theta J_2\left(k_{x'1}(\theta)\sqrt{x'^2+y'^2}\right)\times$$
$$\left\{\begin{array}{l}\left(t_{s01}(\theta,d)-t_{p01}(\theta,d)\sqrt{1-\left(\frac{\sqrt{\varepsilon_0}}{\sqrt{\varepsilon_1}}\sin\theta\right)^2}\right)\exp\left[ik_{z'1}(\theta)z'\right]+\\ \left(r_{s01}(\theta,d)+r_{p01}(\theta,d)\sqrt{1-\left(\frac{\sqrt{\varepsilon_0}}{\sqrt{\varepsilon_1}}\sin\theta\right)^2}\right)\exp\left[-ik_{z'1}(\theta)z'+2idk_{z'1}(\theta)\right]\end{array}\right\}d\theta \quad (3.18)$$

where θ is the incident angle of light, ε_0 and ε_1 are the dielectric constants of oil and ε-Si, respectively. $\theta_{\min}$ and $\theta_{\max}$ are the minimum and maximum angles corresponding to $\sin^{-1}(NA/\sqrt{\varepsilon_0})$. The $k_{x'1}(\theta)$ and $k_{z'1}(\theta)$ are the *x'*- and *z'*-components of the wavenumbers in ε-Si, respectively. The $t_{p01}(\theta,d)$ and $r_{p01}(\theta,d)$ are the transmission and reflection Fresnel coefficients for *p*-polarized light at the ε-Si/SiO_2 interface and ε-Si/oil interface, respectively. Fresnel coefficients of the three layers were calculated by taking into account multiple reflections at different interfaces as outlined in the next section (Section 3.4) and in Chapter 2. In order to consider the attenuation due to the absorption of light crossing the ε-Si layer, Fresnel coefficients are also expressed as a function of thickness *d*. For high NA lens illumination, the *z'*-component is small but not negligible. This means that the scattered light comprises both LO and TO modes. When the scattered Raman passes through the analyzer that is oriented parallel to the incident polarization, LO phonons could be suppressed.

However, the analyzer cannot block the scattered light of the depolarized, $F_2(x',y',z',d)$, signal, which excites LO as well. Thus, even under linearly polarized Raman measurement, both LO and TO are excited and detected.

In addition to the use of linear polarization, radially polarized light can also be utilized to further increase the *z'*-component of the electric field – a prerequisite for TO excitation – while also achieving tighter focus [3.22]. This indicates that by using radially polarized light [3.10], both TO and LO phonons can be excited. In order to enhance the intensity of TO phonon relative to LO phonon mode, it is necessary to increase the longitudinal electric field relative to the transverse field. Radial polarization is the promising approach for this purpose combined with a high NA lens.

When radially polarized light is focused onto the planar surface (*x'y'* plane) through a high NA oil immersion lens, the electric field distribution inside the ε-Si is given by [3.15 – 3.21]:

$$\mathbf{E}_{rad}(x',y',z',d)=\begin{bmatrix} iF_{rad}(x',y',z',d)\dfrac{x'}{\sqrt{x'^2+y'^2}} \\ iF_{rad}(x',y',z',d)\dfrac{y'}{\sqrt{x'^2+y'^2}} \\ -G_{rad}(x',y',z',d) \end{bmatrix}, \tag{3.19}$$

where $\mathbf{E}_{rad}(x',y',z',d)$ is the electric field vector having *x', y'* and *z'*- component of the light at each depth *d* ($0 \le d \le 15$ nm) of the ε-Si sample. The explicit forms of the terms $F_{rad}(x',y',z',d)$ and $G_{rad}(x',y',z',d)$ are given by:

$$F_{rad}(x',y',z',d)=\int_{\theta_{\min}}^{\theta_{\max}}\sqrt{\cos\theta}\sin\theta\sqrt{1-\left(\frac{\sqrt{\varepsilon_0}}{\sqrt{\varepsilon_1}}\sin\theta\right)^2}\,J_1\left(k_{x'1}(\theta)\sqrt{x'^2+y'^2}\right)\times \tag{3.20}$$
$$\left\{t_{p01}(\theta,d)\exp\left[ik_{z'1}(\theta)z'\right]+r_{p01}(\theta,d)\exp\left[-ik_{z'1}(\theta)z'+2idk_{z'1}(\theta)\right]\right\}d\theta$$

$$G_{rad}(x',y',z',d)=\int_{\theta_{\min}}^{\theta_{\max}}\sqrt{\cos\theta}\sin\theta\frac{\sqrt{\varepsilon_0}}{\sqrt{\varepsilon_1}}\sin\theta J_0\left(k_{x'1}(\theta)\sqrt{x'^2+y'^2}\right)\times \\ \left\{t_{p01}(\theta,d)\exp\left[ik_{z'1}(\theta)z'\right]-r_{p01}(\theta,d)\exp\left[-ik_{z'1}(\theta)z'+2idk_{z'1}(\theta)\right]\right\}d\theta \tag{3.21}$$

In the case of azimuthally polarized light, the *z*-component of the electric field is zero. From the Raman polarization selection rules [3.23, 3.24], this indicates that only LO phonons can be detected simply because there is no *z*-polarized component to excite the TO phonons. However, the focus spot profile shows a donut shape [3.25], which degrades the spatial resolution. This is because when the donut shaped focus illuminates the sample, it essentially irradiates two different areas of the sample, and it has a larger focus spot as compared to radial polarization, which has a tighter focus spot. The components of the electric field distributions created by azimuthally polarized, $\mathbf{E}_{azi}(x,y,z,d)$, light are given by [3.15 – 3.21]:

$$\mathbf{E}_{azi}\left(x',y',z',d\right)=\begin{bmatrix} F_{azi}\left(x',y',z',d\right)\dfrac{y'}{\sqrt{x'^2+y'^2}} \\ F_{azi}\left(x',y',z',d\right)\dfrac{x'}{\sqrt{x'^2+y'^2}} \\ 0 \end{bmatrix}, \tag{3.22}$$

where the corresponding form of $F_{azi}(x',y',z',d)$ is described below:

$$F_{azi}(x',y',z',d)=\int_{\theta_{\min}}^{\theta_{\max}}\sqrt{\cos\theta}\sin\theta J_1\left(k_{x'1}(\theta)\sqrt{x'^2+y'^2}\right)\times \\ \left\{t_{s01}(\theta,d)\exp\left[ik_{z'1}(\theta)z'\right]+r_{s01}(\theta,d)\exp\left[-ik_{z'1}(\theta)z'+2idk_{z'1}(\theta)\right]\right\}d\theta \tag{3.23}$$

where $t_{s01}(\theta,d)$ and $r_{s01}(\theta,d)$ are the Fresnel coefficients for *s*-polarized light.

In the backscattering configuration, the same lens is used for the collection of the scattered electric field, $\begin{pmatrix} E_{scaX}\left(\theta,\phi,\eta\right) \\ E_{scaY}\left(\theta,\phi,\eta\right) \\ E_{scaZ}\left(\theta,\phi,\eta\right) \end{pmatrix}$, which consists of all three phonon modes. The dependence of these collected phonon modes (LO and TO) on the NA of the lens need to be integrated to accurately assess the intensity of each phonon modes.

For this reason, to describe the scattering collection process, it is necessary to define an objective transfer matrix, $T_{obj}(\theta,\phi)$, for the scattered Raman polarization vector, e_s, and integrate over the entire polar angle θ subtended by the objective. This calculation is similar to that of the incident light. The scattered Raman polarization vector is defined as:

$$e_s(\eta) = \begin{pmatrix} \cos\eta \\ \sin\eta \\ 0 \end{pmatrix} \tag{3.24}$$

where *h* is the angle setting of the analyzer with respect to the *x'* – axis (*h* = 0 for parallel to *x'* – axis and *h* = 90 for parallel to *y'* – axis). The expression for 3×3 transfer matrix $T_{obj}(\theta,\phi)$ for the scattered Raman polarization vector e_s is [3.26, 3.27]:

$$T_{obj}(\theta,\phi) = t_{p10}(\xi)\begin{pmatrix} \cos\theta\cos\phi \\ \cos\theta\sin\phi \\ -\sin\theta \end{pmatrix}\begin{pmatrix} \cos\phi \\ \sin\phi \\ 0 \end{pmatrix}^T + t_{s10}(\xi)\begin{pmatrix} \sin\phi \\ -\cos\phi \\ 0 \end{pmatrix}\begin{pmatrix} \sin\phi \\ -\cos\phi \\ 0 \end{pmatrix}^T \tag{3.25}$$

where $t_{p10}(\xi)$ and $t_{s10}(\xi)$ are the Fresnel transmission coefficients for *p*- and *s*-polarized (parallel to light traveling from ε-Si to oil), respectively. Since the scattering process takes place inside the ε-Si, the Fresnel coefficients are expressed in terms of $\xi = \sin^{-1}\left(\sqrt{\varepsilon_0/\varepsilon_1}\sin(\theta)\right)$, which is a function of the incident angle of light that varies within $0 \le \theta \le \theta_{\max}$ ($\theta_{\max} = 78^\circ$ for NA = 1.49).

The components of the collected scattered field, $\begin{pmatrix} E_{scaX}(\theta,\phi,\eta) \\ E_{scaY}(\theta,\phi,\eta) \\ E_{scaZ}(\theta,\phi,\eta) \end{pmatrix}$, of a high NA lens at different analyzer settings can be obtained by performing a matrix multiplication of Eqs. (3.24) and (3.25):

$$\begin{pmatrix} E_{scaX}(\theta,\phi,\eta) \\ E_{scaY}(\theta,\phi,\eta) \\ E_{scaZ}(\theta,\phi,\eta) \end{pmatrix} = T(\theta,\phi)\cdot e_s(\eta) = \begin{pmatrix} T_{11}(\theta,\phi)\cos\eta + T_{12}(\theta,\phi)\sin\eta \\ T_{21}(\theta,\phi)\cos\eta + T_{22}(\theta,\phi)\sin\eta \\ T_{31}(\theta,\phi)\cos\eta + T_{32}(\theta,\phi)\sin\eta \end{pmatrix} \tag{3.26}$$

where T_{11}, T_{12}, T_{21}, T_{22}, T_{31}, and T_{33} are the non-zero elements of the $T_{obj}(\theta,\phi)$ objective transfer matrix expressed as:

$$\begin{aligned}
T_{11}(\theta,\phi) &= t_{p10}(\xi)\cos\theta\cos^2 + t_{s10}(\xi)\sin^2\phi \\
T_{12}(\theta,\phi) &= T_{21}(\theta,\phi) = \cos\phi\sin\phi\left[t_{p10}(\xi)\cos\theta - t_{s10}(\xi)\right] \\
T_{22}(\theta,\phi) &= t_{p10}(\xi)\cos\theta\sin^2\phi + t_{s10}(\xi)\cos^2\phi \\
T_{31}(\theta,\phi) &= -t_{p10}(\xi)\sin\theta\cos\phi \\
T_{32}(\theta,\phi) &= -t_{p10}(\xi)\sin\theta\sin\phi
\end{aligned} \tag{3.27}$$

3.4. CALCULATION OF FRESNEL COEFFICIENTS

When a light is focused by a high NA lens through a three-layer system consisting of oil (0^{th} $\varepsilon_0 = 2.356$), ε-Si (1^{st} $\varepsilon_1 = 17.2207 + 0.3569i$) and SiO_2 (2^{nd} $\varepsilon_2 = 2.136$), the amplitude of the *p* and *s*-polarized light changes. The change in the amplitude can be derived from Snell's Law and the Fresnel equations [3.28] given as $\theta = \sin^{-1}(NA/\sqrt{\varepsilon_0})$, where θ is the incident angle of light. The wave number, $k = 2\pi/\lambda$, expressed in terms of wavelength, λ =532nm, can be obtained from each layer as: $k_0 = \sqrt{\varepsilon_0}k$ (oil), $k_1 = \sqrt{\varepsilon_1}k$ (e-Si), and $k_2 = \sqrt{\varepsilon_2}k$ (SiO_2).

Since the components of this wavenumber are dependent on θ , we can represent them as:

$$\left.\begin{aligned}
k_{x0}(\theta) &= k_{x1}(\theta) = k_{x2}(\theta) = k_0\sin\theta \\
k_{z0}(\theta) &= k_0\cos\theta \\
k_{z1}(\theta) &= k_1\sqrt{\left(1 - \frac{\varepsilon_0}{\varepsilon_1}\sin^2\theta\right)} \\
k_{z2}(\theta) &= k_2\sqrt{\left(1 - \frac{\varepsilon_0}{\varepsilon_2}\sin^2\theta\right)}
\end{aligned}\right\} \tag{3.28}$$

The transmission, $t_{p01}(\theta,d)$, and the reflection, $r_{p01}(\theta,d)$, Fresnel coefficients for *p*-polarized light are given by:

$$t_{p01}(\theta,d) = \frac{t_{p01}(\theta)}{1 + r_{p01}(\theta)r_{p12}(\theta)\exp\left[2ik_{z1}(\theta)d\right]} \tag{3.29}$$

$$r_{p01}(\theta,d) = \frac{t_{p01}(\theta)r_{p12}(\theta)}{1 + r_{p01}(\theta)r_{p12}(\theta)\exp\left[2ik_{z1}(\theta)d\right]} \tag{3.30}$$

where, *d* (=15nm) is the thickness of ε-Si. Note that the equations are express in complex Fresnel coefficients to take into account the effect of extinction coefficient,

which is not negligible for shorter laser wavelengths. This is important because some information on the change of the stress with depth can be obtained by using different excitation wavelengths.

The reflection and transmission coefficients at different interfaces of the three-layer system are as follows:

$$r_{p01}(\theta)=\frac{\varepsilon_0 k_{z1}(\theta)-\varepsilon_1 k_{z0}(\theta)}{\varepsilon_1 k_{z0}(\theta)+\varepsilon_0 k_{z1}(\theta)}\text{, Reflection coefficient from oil (0}^{th}\text{) to ε-Si (1}^{st}\text{)} \quad (3.31)$$

$$t_{p01}(\theta)=\frac{2\sqrt{\varepsilon_0}\sqrt{\varepsilon_1}k_{z0}(\theta)}{\varepsilon_1 k_{z0}(\theta)+\varepsilon_0 k_{z1}(\theta)}\text{, Transmission coefficient from oil (0}^{th}\text{) to ε-Si (1}^{st}\text{)} \quad (3.32)$$

$$r_{p12}(\theta)=\frac{\varepsilon_1 k_{z2}(\theta)-\varepsilon_2 k_{z1}(\theta)}{\varepsilon_2 k_{z1}(\theta)+\varepsilon_1 k_{z2}(\theta)}\text{, Reflection coefficient from ε-Si (1}^{st}\text{) to SiO}_2\text{ (2}^{nd}\text{).} \quad (3.33)$$

The Fresnel coefficients for *s*-polarized light are given by:

$$t_{s01}(\theta,d)=\frac{t_{s01}(\theta)}{1+r_{s01}(\theta)r_{s12}(\theta)\exp\left[2ik_{z1}(\theta)d\right]} \quad (3.34)$$

$$r_{s01}(\theta,d)=\frac{t_{s01}(\theta)r_{s12}(\theta)}{1+r_{s01}(\theta)r_{s12}(\theta)\exp\left[2ik_{z1}(\theta)d\right]} \quad (3.35)$$

where, d (=15nm) is the thickness of ε-Si and

$$r_{s01}(\theta)=\frac{k_{z0}(\theta)-k_{z1}(\theta)}{k_{z0}(\theta)+\varepsilon_0 k_{z1}(\theta)}\text{, Reflection coefficient from oil (0}^{th}\text{) to e-Si (1}^{st}\text{)} \quad (3.36)$$

$$t_{s01}(\theta)=\frac{2k_{z0}(\theta)}{k_{z0}(\theta)+k_{z1}(\theta)}\text{, Transmission coefficient from oil (0}^{th}\text{) to ε-Si (1}^{st}\text{)} \quad (3.37)$$

$$r_{s12}(\theta)=\frac{k_{z1}(\theta)-k_{z2}(\theta)}{k_{z1}(\theta)+k_{z2}(\theta)}\text{, Reflection coefficient from ε-Si (1}^{st}\text{) to SiO}_2\text{ (2}^{nd}\text{).} \quad (3.38)$$

For scattered photons traveling from ε-Si to oil, the Fresnel coefficients are:

$$t_{p10}(\xi)=\frac{2\sqrt{\varepsilon_1}\sqrt{\varepsilon_0}k_{z10}(\xi)\sqrt{k_{z11}(\xi)/k_{z10}(\xi)}}{\varepsilon_0 k_{z10}(\xi)+\varepsilon_1 k_{z11}(\xi)}, \quad (3.39)$$

the transmission coefficient from ε-Si (1st) to oil (0th)

$$t_{s10}(\xi) = \frac{2k_{z10}(\xi)\sqrt{k_{z11}(\xi)/k_{z10}(\xi)}}{k_{z10}(\xi)+k_{z11}(\xi)}, \tag{3.40}$$

the transmission coefficient from ε-Si (1st) to oil (0th)

where $\xi = \sin^{-1}\left(\sqrt{\varepsilon_0/\varepsilon_1}\sin(\theta)\right)$

$$k_{z10}(\xi) = \sqrt{\varepsilon_1}k\cos\xi \tag{3.41}$$

$$k_{z11}(\xi) = \sqrt{\varepsilon_0}k\sqrt{1-\frac{\varepsilon_1}{\varepsilon_0}\sin^2\xi} \tag{3.42}$$

3.5. PHONON MODE VISUALIZATION IN STRAINED SILICON VIA THREE-DIMENSIONAL RAMAN INTENSITY CALCULATION

Figure 3.5 shows the results of numerically simulated 1 x 1 μm^2 electric field distributions inside the ε-Si surface at different polarizations. Three kinds of polarization are studied, namely, linear, radial and azimuthal. These distributions were obtained for a 532 nm light source focused using the full aperture of a high numerical aperture (NA) (0 ≤ NA ≤ 1.49) oil immersion lens. To simplify the comparison, the electric field distributions were normalized at each polarization.

The incident electric field (Fig. 3.5) is the field that has exited the microscope objective and illuminates the ε-Si sample. For each polarization, the incident field has been decomposed into the *x'*, *y'*, and *z'*-components. In all polarizations, the three components of the incident electric field are non-zero – except for the *z'*-component of azimuthal polarization. This indicates that the three Raman modes of Si (TO_1, TO_2 and LO) are excited for high NA illumination based on Eq. (3.13). Clear differences can be seen among the different polarization types when the incident field illuminates either a nanomembrane or nanowire. The intensity distribution of the incident field determines the intensity profile of the excited phonon modes. The intensity profile of the LO mode is dictated by either *x'* or *y'* depending on the analyzer setting, while the intensity profiles of the TO modes are that of *z'*. In the case of azimuthal polarization, the TO modes' intensity profiles are the sum of the *x'* and *y'*.

The Porto notations $z'\left(*,x'\right)\bar{z}'$ and $z'\left(*,y'\right)\bar{z}'$ are used to indicate when the analyzer is set parallel to the *x'*-axis (η = 0˚) or *y'*-axis (η = 90˚), respectively. The " * " implies linear, radial or azimuthal incident polarization. The TO/LO ratio in the numerical

simulations is computed by adding the intensities of the TO_1 and TO_2 modes and dividing this sum by the intensity of the LO signal. The individual intensities of the phonon modes are taken by integrating the intensity in three dimensions over the 15 nm thick ε-Si nanomembrane.

3.5.1. Nanomembrane

In the case of the ε-Si nanomembrane (Fig. 3.5), the Raman intensity is normalized with respect to the maximum Raman intensity of the LO signal at each analyzer setting.

For linearly polarized light, the incident field has a strong *x'*-polarized component as compared to the depolarized *y'*- and the normal *z'*-components. Thus, LO phonon are mostly excited. In the $z'\left(x',x'\right)\bar{z}'$ setting, the LO intensity is strong compared to the TO_1 and TO_2 intensities even after scaling the TO value 40 times. This is reflected by the TO/LO ratio which is ~ 0.1. In the $z'\left(x',y'\right)\bar{z}'$ setting, the TO_1 and the TO_2 phonon modes can be detected because the LO mode is mostly filtered out by the analyzer. This results to a higher TO/LO ratio of ~ 0.94 as compared to the $z'\left(x',x'\right)\bar{z}'$ setting. Hence, we designate the $z'\left(x',x'\right)\bar{z}'$ to be LO-active and $z'\left(x',y'\right)\bar{z}'$ to be TO-active. For radial polarization, the *x'* and *y'*-components have similar intensities. But, the *z'*-component of the incident electric field is tightly focused and, comparing this feature to the two lobes in linear polarization, indicates better spatial resolution. Also, the intensity of the radially polarized *z'*-component is relatively higher – by around twice – than the linearly polarized incident field (Fig. 3.6a). This makes radially polarized light TO-active and suitable for TO characterization. For azimuthal polarization, there is no *z'*-component. Therefore, the TO_1 and TO_2 Raman signals are very weak, making this polarization LO-active.

The integrated intensities of TO_1 and TO_2 are assumed to be equal because of symmetry in the sample (for both nanomembrane and nanowire), but differences in the distribution can be seen between the two modes. This is due to the polarization selection rules [3.1, 3.2, 3.10]. The behavior of the transverse electric fields are determined by the Raman tensors, R_x and R_y for TO_1 and TO_2, respectively. For TO_1, the transverse fields add up resulting to a circular distribution. For TO_2, the transverse fields cancel each other resulting to a more oval-shaped distribution.

3.5.2. Nanowire

From the nanomembrane simulation data, the Raman intensity distribution on the ε-Si sample is not uniform and the location of the most intense areas vary depending on the polarization of the incident electric field. This information is important when characterizing strain in nanostructures such as nanowires because, depending on the location of the focused light on the nanowire, the detected Raman signal can be either LO or TO phonon modes.

Figure 3.5 shows the Raman intensity distribution on ε-Si nanowires having 30 nm width, 1 mm length and 15 nm thickness within a diffraction-limited focused spot given by 1.22λ/NA (~ 436 nm). In the simulation of the ε-Si nanowires, the Raman intensity is normalized with respect to the maximum Raman intensity of either the LO or TO_1 signal at each analyzer setting.

In the TO-active $z'(x',y')\bar{z}'$ and $z'(\mathrm{rad},y')\bar{z}'$ settings, there is a considerable increase in the TO/LO ratio for both polarizations compared to their nanomembrane counterparts. This is because, as it can be seen from the LO profile of the nanomembrane, when using a nanowire that is located parallel to the *x'*-axis, the LO components induced by the depolarized field (E_y) can be drastically reduced resulting in a high contrast of TO/LO ratio. For $z'(x',y')\bar{z}'$, the TO/LO ratio is 84.57 while for $z'(rad,y')\bar{z}'$, the TO/LO ratio is 12.62. This change in TO/LO ratio is also dependendent on the width of the nanowire as shown in Fig. 3.7a. The data shown is from the $z'(x',y')\bar{z}'$ setting. The same behavior is also observed for the $z'(\mathrm{rad},y')\bar{z}'$ setting. The TO/LO ratio peaks at a nanowire width of 20 nm and then decreases approaching a value of 0.94 as the width reaches infinity (nanomembrane case). The increase and then decrease for widths larger than 20 nm is due to the change of the overlap between the electric field distribution of the tight focus and the nanowire structure. Precisely, this rapid increase of the LO intensity as the width increases is caused by the depolarized electric field contribution in the $z'(x',y')\bar{z}'$ configuration (Fig. 3.7b). Based on the simulation, it should be pointed out that the TO/LO ratio is sufficiently high allowing for selective detection of TO Raman signals particularly when the width is smaller than 100 nm because of less contribution by the depolarized electric field induced LO Raman signal. Continuing the comparison of $z'(x',y')\bar{z}'$ and $z'(\mathrm{rad},y')\bar{z}'$, the probed area is different for the two polarizations. In

terms of TO detection sensitivity, linear polarization is more sensitive than radial polarization judging from the TO/LO ratio. But when similar laser power is used, the TO intensity is stronger for radial polarization than for linear polarization, as shown in Fig. 3.6b. Therefore, radial polarization is useful for low laser power TO characterization in ε-Si nanowires. With the improved sensitivity of TO phonon modes for nanowires, it is reasonable to fit the spectra of $z'(x',y')\bar{z}'$ configuration with double Lorentzian functions for the split TO_1 and TO_2.

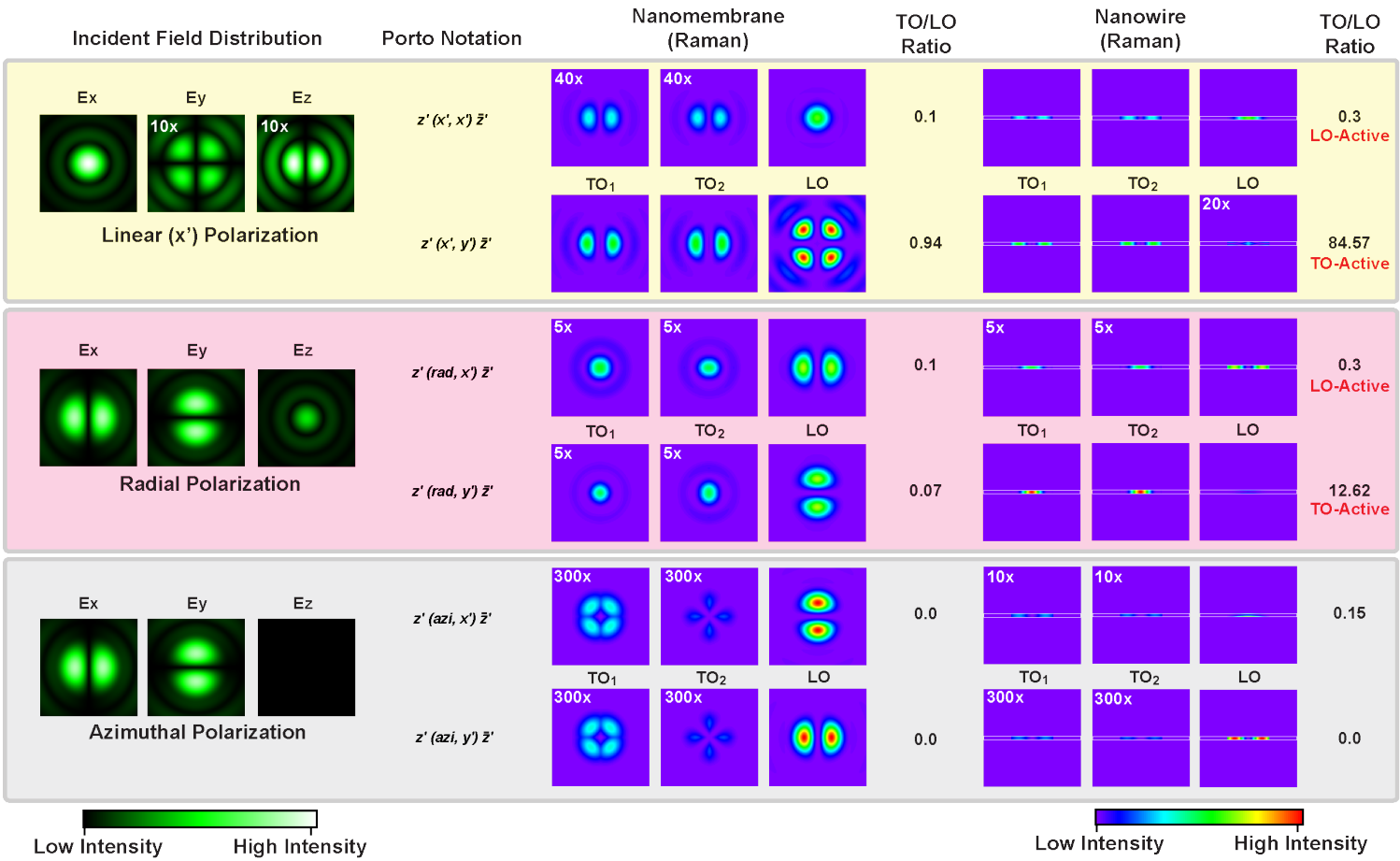

Figure 3.5. Incident electric field distribution illuminating the surface of the ε-Si nanomembrane and nanowires with the calculated Raman intensities using Eq. 3.13 at various polarizer and analyzer settings. Raman intensities were normalized at each setting. Image size is 1 x 1 μm^2. The maximum Raman intensity is observed to be at the SiO_2 and ε-Si interface.

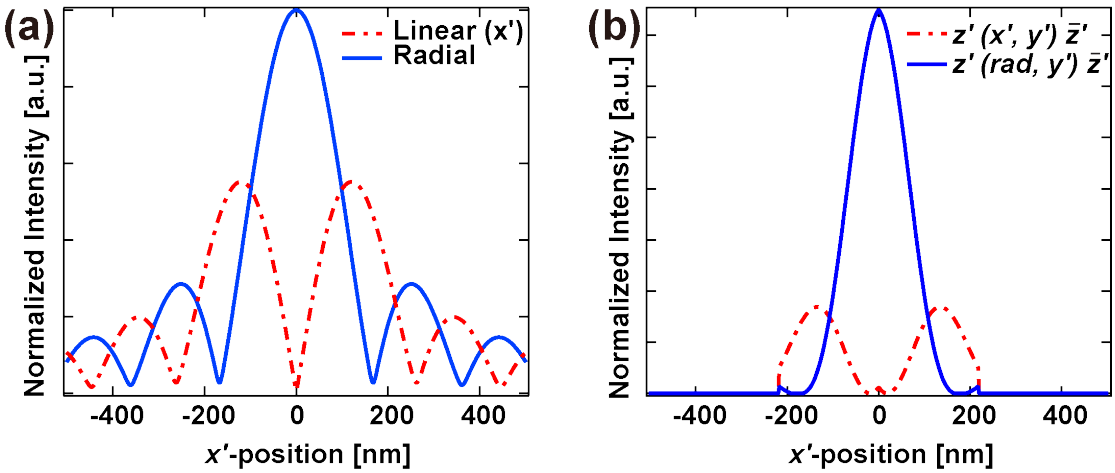

Figure 3.6. Comparison of line profiles across the center of (a) $E_{z'}$ component of the incident electric field for linear and radial polarization in a nanomembrane. (b) TO_1 intensity comparison for TO-active $z'(x',y')\bar{z}'$ and $z'(\mathrm{rad},y')\bar{z}'$ configuration in a nanowire. The smaller area reflects the diffraction-limited focus spot illuminating the sample.

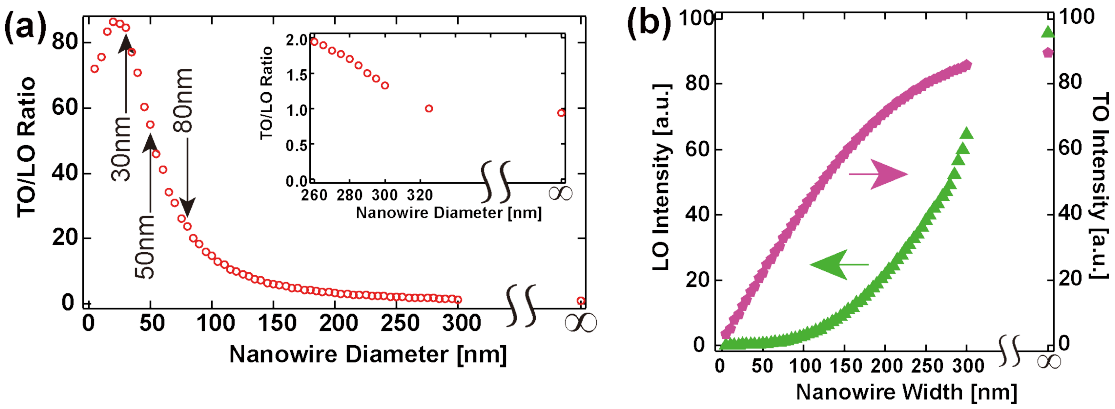

Figure 3.7 (a) Calculated Raman intensity ratio of TO and LO phonon signal as a function of nanowire width. The arrows indicate the widths used in experiments. Inset shows the TO/LO ratio for nanowires greater than 250 nm up to infinity. The TO/LO ratio reaches a value of 0.94. (b) Calculated Raman intensity of each phonon mode as a function of nanowire width. LO intensity drastically increases with larger width because of the depolarized electric field contribution (e.g. $E_{y'}$ field in $z'(x',y')\bar{z}'$ configuration).

3.6. REFERENCES

[3.1] R. Loudon, The Raman effect in crystals, *Adv. Phys.,* **13**, 423-482, 1964.

[3.2] I. De Wolf, Micro-Raman spectroscopy to study local mechanical stress in silicon integrated circuits, *Semicond. Sci. Technol.*, **11**, 139-154, 1996.

[3.3] C. Kittel, *Introduction to Solid State Physics: Eighth Edition*, John Wiley & Sons, Inc: USA, 2005.

[3.4] R. Ossikovski, Q. Nguyen,G. Picardi and J. Schreiber, Determining the stress tensor in strained semiconductor structures by using polarized micro-Raman spectroscopy in oblique backscattering configuration, *J. Appl. Phys.*, **103**, 093525, 2008.

[3.5] G. Turrell, J. Corset, *Raman Microscopy: developments and applications*, Elsevier, London, 1996.

[3.6] P. Yu, M. Cardona, *Fundamentals of Semiconductors: Physics and Materials Properties 3rd Edition*, Springer: Berlin, 2001.

[3.7] I. De Wolf, H.E. Maes, and S.K. Jones, Stress measurements in silicon devices through Raman spectroscopy: bridging the gap between theory and experiment. *J. Appl. Phys.* **79**, 7148-7156, 1996.

[3.8] **M.V. Balois**, N. Hayazawa, A. Tarun, S. Kawata, M. Reiche and O. Moutanabbir. *Direct optical mapping of anisotropic stresses in nanowires using transverse optical phonon splitting*. Nano Lett. **14**, 3793-3798, 2014.

[3.9] P.V. Huong, A.L Verma, J.P. Chaminade, L. Nganga and J.C. Frison, Characterization of materials by micro-Raman spectroscopy, *Materials Science and Engineering, B5,* 255-260, 1990.

[3.10] A. Tarun, N. Hayazawa, H. Ishitobi, S. Kawata, M. Reiche and O. Moutanabbir, Mapping the “forbidden” transverse-optical phonon in single strained silicon (100) nanowire, *Nano Lett.* **11**, 4780-4788, 2011.

[3.11] D. Kosemura and A. Ogura, Transverse-optical phonons excited in Si using a high-numerical aperture lens, *Appl. Phys. Lett.* **96**, 212106, 2010.

[3.12] K. Mizoguchi, and S. Nakashima. "Determination of Crystallographic Orientations in Silicon Films by Raman-Microprobe Polarization Measurements", J. Appl. Phys., 65, pp.2583-2590 (1989).

[3.13] S. Ganesan, A.A. Maradudin, and J. Oitmaa, A lattice theory of morphic effects in crystals of the diamond structure, *Ann. Phys.* **56**, 556-594, 1970.

[3.14] J.B. Hopkins and L.A. Farrow, Raman microprobe determination of local crystal orientation, *J. Apply. Phys.* **59**, 1103-1110, 1986.

[3.15] B. Richards and E. Wolf, Electromagnetic diffraction in optical systems II. Structure of the image field in an aplanatic system, *Proceedings of the Royal Society A: Mathematical, Physical and Engineering Sciences,* **253**, 358-379, 1959.

[3.16] P. Török, P. Varga, Z. Laczik and G.R. Booker, Electromagnetic diffraction of light focused through a planar interface between amterials of mismatched refractive indices: an integral representation, *J. Opt. Soc. Am. A*, **12**, 325-332, 1995.

[3.17] J.J. Stamnes, *Waves in Focal Regions: propagation, diffraction and focusing of light, sound and water waves*, IOP Publishing Limited: Bristol, 1986.

[3.18] K.S. Youngworth and T.G. Brown, Focusing of high numerical aperture cylindrical-vector beams, *Optics Express*, **7**, 77-87, 2000.

[3.19] D.P. Biss and T.G. Brown, Cylindrical vector beam focusing through a dielectric interface, *Optics Express*, **9**, 490-497, 2001.

[3.20] L.E. Helseth, Roles of polarization, phase and amplitude in solid immersion lens systems, *Optics Communications*, **191**, 161-172, 2001.

[3.21] H. Ishitobi, I. Nakamura, N. Hayazawa, Z. Sekkat, and S. Kawata, Orientational imaging of single molecules by using azimuthal and radial polarizations, *J. Phys. Chem. B,* **114**, 2565-2571, 2010.

[3.22] S. Quabis, R. Dorn, M. Eberler, O. Glöckl and G. Leuchs, Focusing light to a tighter spot, *Optics Communications* **179**, 1-7, 2000.

[3.23] A. Tarun, N. Hayazawa, M. Motohashi, and S. Kawata, *Rev. Sci. Instrum.,* **79**, 013706, 2008.

[3.24] R. A. Minamisawa, M. J. Süess, R. Spolenak, J. Faist, C. David, J. Gobrecht, K. K. Bourdelle, and H. Sigg, *Nat. Comm.*, **3**, 1096, 2012.

[3.25] N. Hayazawa, K. Furusawa, A. Taguchi, and S. Kawata, *J. Apply. Phys.*, **106**, 113103, 2009.

[3.26] Deb, S. K.; Bansal, M. L. Roy, A. P. *Appl. Spectrosc.* **1984**, 38, 500.

[3.27] F. Cerdeira, C. J. Buchenauer, F. H. Pollak, and M. Cardona. *Phys. Rev. B.* **1972**, 5, 508.

[3.28] M. Born and E. Wolf, *Principles of Optics: Seventh (Expanded) Edition,* Cambridge University Press: New York, 2009.

Chapter 4: Strained Silicon: a micro-Raman spectroscopy characterization study of stress after nanopatterning via precise polarization control [4.1 – 4.2]

Silicon (Si) electronics currently have a nanowire-based architecture to achieve lower power consumption, higher performance and scalable devices whose constant trend of miniaturization is dictated by Moore's law [4.2]. Si nanowires are quasi-one-dimensional nanostructures that can overcome the limitations faced in two-dimensional planar devices [4.3 – 4.8]. Therefore, transistors employ nanowire-like channels to create high-performance microprocessors and memory devices for wireless systems such as mobile phones and radars [4.2]. Such new technologies utilize nanowires that have three free facets with the fourth facet forming an interface with the underlying substrate [4.7, 4.8]. But due to the quantum confinement and scattering at the sidewalls, these nanowires suffer degradation in carrier velocity that decreases device performance [4.9, 4.10]. Stress nano-engineering has emerged as a powerful technique to alleviate these limitations and extend the capabilities of nanowire-based electronics [4.11].

Strain engineering has been used in the microelectronics industry since the 90-nm technology node [4.1]. This approach employs deposition of stressor layers on top of transistors. The dimensions of nanowire-based transistors, however, are becoming smaller than the required thickness of the stressor overlayer, making it difficult to employ this method for smaller nodes or other nanowire-based architectures. Recently, ultrathin, globally strained silicon layers (called nanomembranes) have been the base material to generate strained Si nanowires (ε-SiNWs) via top-down nanofabrication processes [4.11 – 4.13]. A crucial step in the fabrication of ε-SiNWs involves nanoscale patterning (nanopatterning) of biaxially strained nanomembranes, but this step results in the formation of free surfaces. The free surfaces cause a local relaxation of strain due to the rearrangement of lattice atoms near the newly formed edges [4.12, 4.14 – 4.18]. Generally speaking, the extent of this phenomenon depends on dimension and geometry [4.14 – 4.18]. It is widely accepted, however, that due to nanowire geometry (i.e., the high aspect ratio) the post-patterning stress becomes uniaxial, which means that the stress is fully relaxed along the width of the nanowire [4.11, 4.14]. But this is not the case for nanowires directly fabricated on oxide as discussed in this chapter. The nanowire-substrate interface makes the strain redistribution rather complex due to the underlying oxide layer that stabilizes one of

the four facets [4.1]. After nanopatterning, it is found that the ε-SiNWs experience anisotropic stress relaxation. The amount of relaxation is very much dependent on the dimensions of the ε-SiNWs [4.2]. Another important aspect that is investigated is the effect of the nanomembrane edge on the stress distribution of the ε-SiNWs [4.19]. The proximity of the ε-SiNW to the nanomembrane edge can affect the stress present in the nanowire. Exploring and understanding these subtle but important phenomena is crucial for accurate strain nano-engineering and a precise prediction of the performance of strained Si nanowire-based devices.

To probe the evolution of strain and stress in ε-SiNWs, Tarun et. al. recently developed a high-resolution polarized micro-Raman spectroscopic technique that allows the detection and analysis of the individual contributions of longitudinal optical (LO) phonons and transverse optical (TO) phonons [4.12]. In this work, to explore the effects of the interface, I employ two excitation wavelengths with linear polarizations corresponding to different penetration depths in silicon thereby achieving LO phonon detection as a local stress probe at different depths within a single nanowire. To probe the effects of the nanomembrane edge on the stress redistribution in ε-SiNWs, I employ a single excitation wavelength (532 nm) using linear polarization. This is because of the stronger signal-to-noise ratio that can be achieved when using 532-nm illumination. Direct detection of TO phonon modes can characterize anisotropic stress relaxations at each position by using a high NA lens and proper polarization. I experimentally demonstrated for the first time the splitting of TO phonon modes and was able to analyze the dimension dependence of anisotropic stress relaxation. I also discuss and take into consideration the effects of the scattering at the nanowire sidewalls on the obtained Raman data and present two methods for accurate determination of stress in nanoscale structures. The first method is LO phonon analysis, while the second method is TO analysis. A comparison of the two is made at the end of this chapter.

The work presented in this chapter is adapted from Balois and Tarun, et. al. (2013) [4.1] and Balois, et. al. (*in preparation*) [4.19] for the analysis of stress redistribution in ε-SiNWs and nanomembranes using longitudinal optical (LO) phonon analysis and Balois, et. al. (2014) [4.2] for the analysis of anisotropic stress relaxation in ε-SiNWs using transverse optical (TO) phonon analysis.

4.1 SAMPLE FABRICATION

There are two kinds of samples used in all the experiments discussed in this chapter. The first kind of sample is a ε-Si nanomembrane (Figure 4.1) that has a 1 μm length, 15 nm thickness and 10 μm width. The second kind of sample is ε-Si nanowires with a fixed 1 μm length, 15 nm thickness and varying widths of 80 nm, 50 nm and 30 nm (Fig. 4.1a – only 80 nm width is shown). Figure 4.1b shows the transmission electron microscopy (TEM) cross-sectional image of the ε-Si sample.

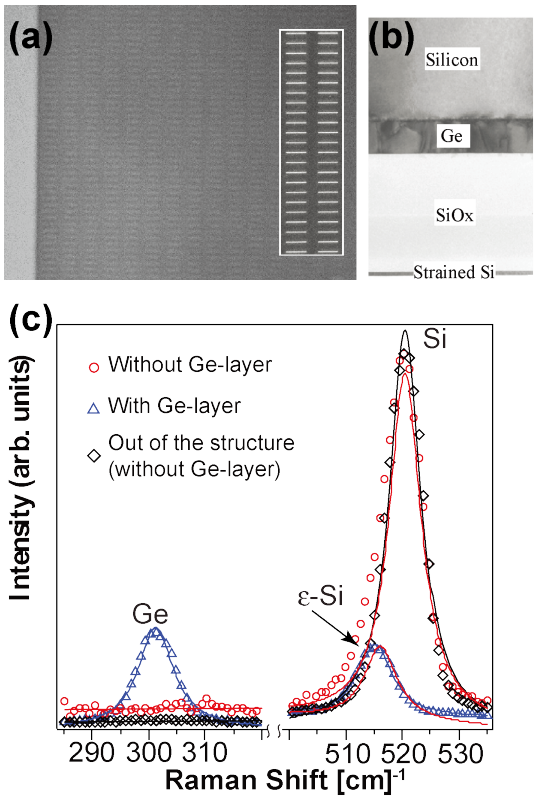

Figure 4.1 (a) Optical reflection image of the nanowires aligned near the unpatterned nanomembrane and the scanning electron micrograph image of the aligned nanowires (inset). The scale bar indicates 2 mm. **(b)** TEM of the cross-sectional profile of the ε-Si sample. The scale bar indicates 75 nm. **(c)** Comparison of Raman spectra with and without Ge layer. The Ge layer perfectly suppresses the background Raman signal of the silicon substrate peaked at 520.5 cm^{-1} and allows selective detection of the ε-Si layer.

From a 15 nm thick biaxially tensile ε-Si nanomembrane, the ε-SiNWs were formed by nanopatterning and electrochemical etching. The fabrication process is shown in Figs. 4.2a – f. To generate the ε-Si nanomembrane, an ultrathin layer of Si was epitaxially grown on a ~500 nm thick $Si_{0.84}Ge_{0.16}$ relaxed buffer layer. This buffer layer is grown on a Si (001) substrate via reduced pressure chemical vapor deposition. A ε-Si/$Si_{0.84}Ge_{0.16}$/Si heterostructure was made and the ε-Si layer was coated with a SiO_2 layer via plasma-enhanced chemical vapor deposition. The Si (001) host

substrate was prepared separately which consists of a ~120 nm thick Ge layer deposited directly on top of the Si host substrate via solid molecular beam epitaxy. The Ge layer was then coated with a ~200 nm thick SiO_2 layer. The ε-Si layer was transferred to the host substrate via direct wafer bonding. Ion-induced slicing was used to remove the $Si_{0.84}Ge_{0.16}$/Si wafer and selective chemical etching was conducted to remove the excess $Si_{0.84}Ge_{0.16}$ relaxed buffer layer. The resulting wafer was a ε-Si/SiO_2/Ge/Si heterostructure with a 15 nm thick ε-Si nanomembrane layer. The role of the Ge is to act as a shield that prevents the laser from reaching the Si substrate, in the case of visible excitation. The existence of the Ge layer allows us to selectively detect the ε-Si layer without any background signal from the underlying Si host substrate. Ordered arrays of rectangular nanostructures, spaced 500 nm apart, were patterned onto a negative resist using electron-beam lithography. Reactive ion etching (RIE) was used to transfer the pattern to the strained layer, forming ordered arrays of rectangular ε-Si nanowires directly on SiO_2. The patterned islands are aligned along the [110] direction. The RIE process was done at a pressure of 6 mTorr using a mixture of SF_6 (100 sccm) and O_2 (5 sccm) with a rate of ~2 nm s^{-1} [4.20].

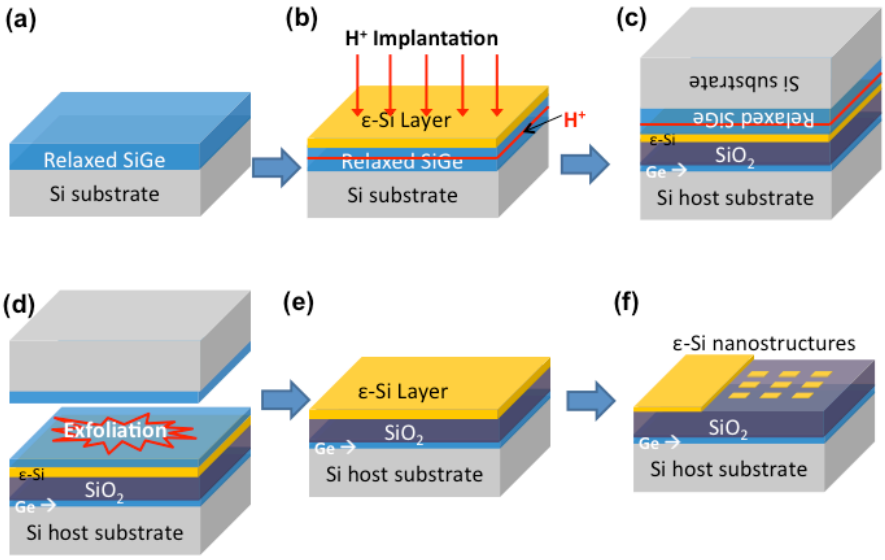

Figure 4.2. Illustration of the process flow for the fabrication of background-free ultrathin ε-SiNWs using thin layer transfer. (a) Growth of $Si_{0.84}Ge_{0.16}$ relaxed buffer layer on Si-(001) substrate; (b) growth of biaxially tensile strained Si on $Si_{0.84}Ge_{0.16}$ and subsequent hydrogen ion implantation into the grown heterostructure; (c) growth of Ge layer and SiO_2 deposition on Si host substrate and bonding of hydrogen-implanted heterostructure onto host substrate; (d) exfoliation via thermal annealing around the hydrogen implantation depth; (e) polishing to remove excess $Si_{0.84}Ge_{0.16}$ relaxed buffer layer; (f) Nanopatterning of ε-Si nanostructures using electron beam lithography and RIE. [Adapted from Ref. 4.12 with permission from ACS Publications]

4.2 EXPERIMENTAL SETUP

Figure 4.3 shows the experimental setup used for both LO and TO experiments. Laser light (λ = 355 nm, 442 nm, for LO multiwavelength experiment and 532 nm for TO analysis and comparative LO analysis) passes through a linear polarizer and a half wave plate. The linear polarizer sets the incoming polarization from the laser. The half-wave plate is used to align the incident polarized beam either parallel (*x'*) or perpendicular (*y'*) to the nanowire long axis. The beam is then expanded and focused onto the nanowires using an oil-immersion objective lens (numerical aperture, NA = 1.4, x125 for 355 nm and 442 nm experiments, and NA = 1.49, x100, for 532 nm). The surface of the ε-Si is directly immersed in oil. This configuration improves the laser focusing and minimizes index mismatch-induced spherical aberrations. According to the Rayleigh criterion, the diameter of the laser spot is $\lambda/2$. The backscattered Raman signal is collected by the same objective lens and passes through a pinhole (ϕ = 50 mm), which leads to an edge filter to block the strong Rayleigh signal in order for the backscattered Raman signal to be detected. The backscattered light goes through an analyzer before reaching a spectrometer (grating = 1800 g mm^{-1}, slit width = 50 μm) equipped with a thermo-electronically cooled charge coupled device (CCD) camera. The samples with nanowire arrays were mounted on an *x'-y'* translation stage and were scanned with a 25 nm step while exposed to the focused laser beam. At each step, a Raman spectrum was recorded. To prevent laser heating, Raman spectra were acquired at 5 mW power. For the LO data, a 6 μm x 6 μm area was scanned with an exposure time of 0.5 s/pixel (total scan time ~ 12 hours / image). For the TO data, a 3.5 μm x 2.75 μm area was scanned with an exposure time of 5 s/pixel (total scan time ~ 22 hours / image). A longer exposure time was needed for the TO data because of its relatively weaker signal compared to the LO data. Acquiring both LO and TO data required scan time ranging from half a day to almost a day. For long duration experiments like these, stability of the experimental system is important, especially thermal stability, which can induce both defocusing and sample drift. To address these issues, an autofocusing system [4.21] has been installed to the microscope objective assembly and a thermal control booth enclosed the entire confocal microscope system.

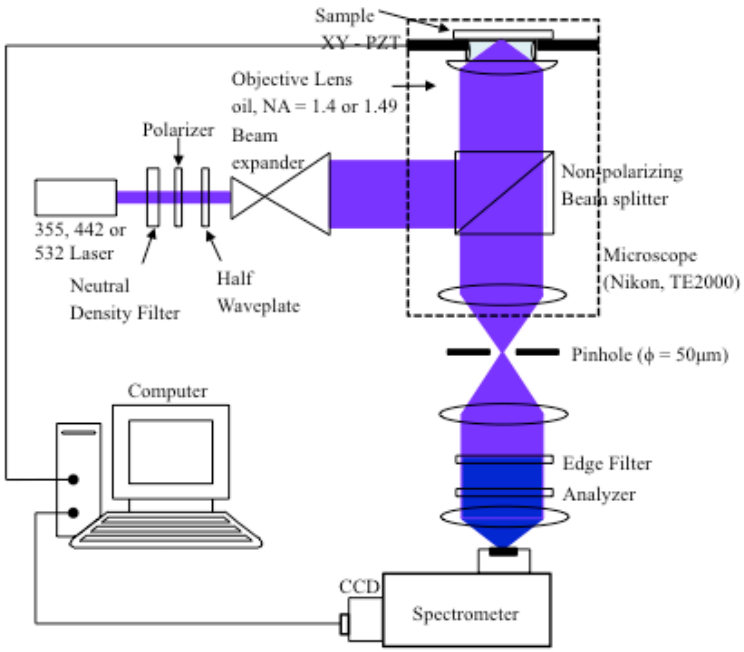

Figure 4.3 Experimental setup for LO and TO detection.

4.2.1 Stability of the Experimental System

As mentioned in the previous section, image acquisition during the LO and TO experiments require a considerable amount of time. In imaging experiments, it is important that the illuminating laser remain focused onto the sample during the entire experiment to avoid image degradation and erroneous data analysis. Stability becomes a key issue since fluctuations in the experimental system and its environment are not negligible as they compound over time. Fluctuations can be electrical, vibrational or thermal in nature. Electrical and vibrational fluctuations can be dealt with by state-of-the-art circuits and ingenious vibrational isolation designs that are commercially available. Thermal fluctuations are more complex because these fluctuations can come from a variety of sources, even from the person operating the experimental system. Two unavoidable consequences arise from thermal fluctuations: 1) thermal drift of the sample in the *x'* and *y'*-directions and 2) defocusing caused by drifting of the microscope objective in the *z'*-direction. To minimize sample drift (*x'*-*y'*), a thermally controlled booth was installed to enclose the entire confocal microscope system. Figure 4.4a shows the temperature booth controller (left-side) and the temperature boot (right side). This booth regulates the temperature inside the booth to be constantly at 22˚C with a minimal fluctuation of ± 0.1˚C, as shown in Fig. 4.4b. When the temperature booth is turned OFF, the temperature is not stable and either increases or decreases. As for the defocusing, an autofocusing system [4.21] has been installed and attached to the microscope

objective (Fig. 4.5a). Figure 4.5b shows the configuration of the autofocusing system. It is composed of a capacitive sensor (Mess-tek TRA616-200-V2) that can be attached to any microscope objective mounted on a Z-PZT stage (Nanocontrol, PFHC252R-020U-N). A microscope objective with a high NA is preferable to attain a tightly focused spot. The capacitive sensor has a maximum dynamic range of 100 μm. A polyimide tape (thickness ~ 50 μm) is used as a spacer to form a gap between the capacitive sensor and the grounded sample stage, which serves as a counter electrode. The capacitive sensor recognizes the gap and the signal is converted to DC voltage (low-pass-filter: 1 kHz). An analog-digital converter (16-bit resolution) constantly monitors the DC voltage from the capacitive sensor. After setting the focused position of the objective lens, the DC voltage of the sensor is locked. If there are changes in the voltage, which can be due to the movement of the objective lens in the *z*'-direction or tilting of the sample, a feedback voltage is applied to the Z-PZT (dynamic range: 2 μm; bandwidth: DC ~ 1 kHz) to compensate for the displacement. This autofocusing system constrains the gap fluctuation within ± 1 nm [4.21].

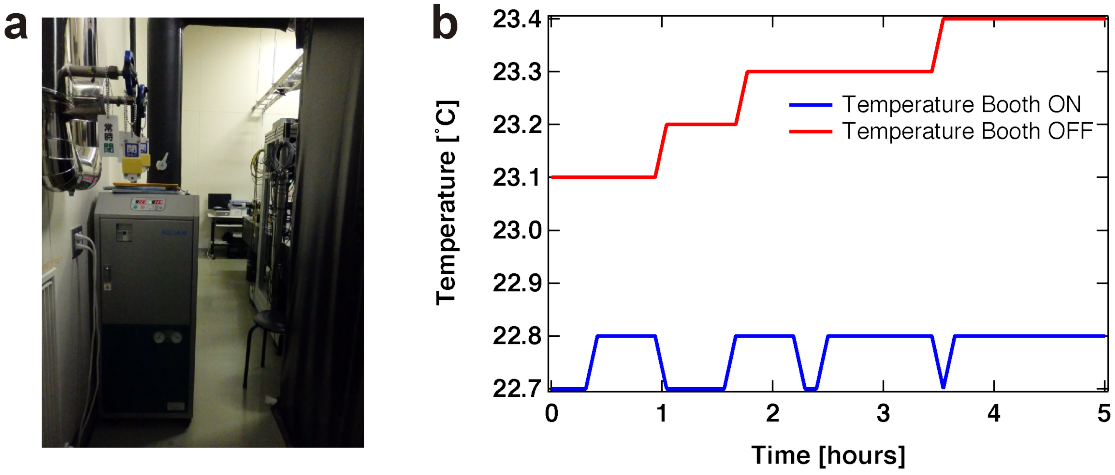

Figure 4.4 (a) Temperature booth controller and temperature booth (black structure at the right side of picture). (b) Temperature fluctuation when temperature booth is ON and OFF.

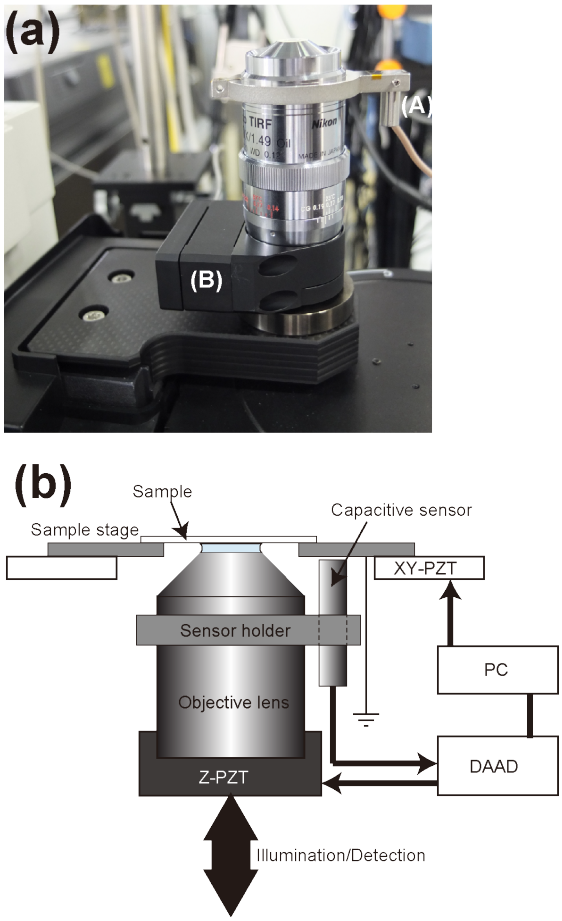

Figure 4.5 (a) Autofocusing system installed onto the microscope objective lens where (A) is the capacitive sensor and (B) is the Z-PZT. (b) Schematic of the autofocusing system [Adapted from Ref. 4.21 with permission from IOP Publishing].

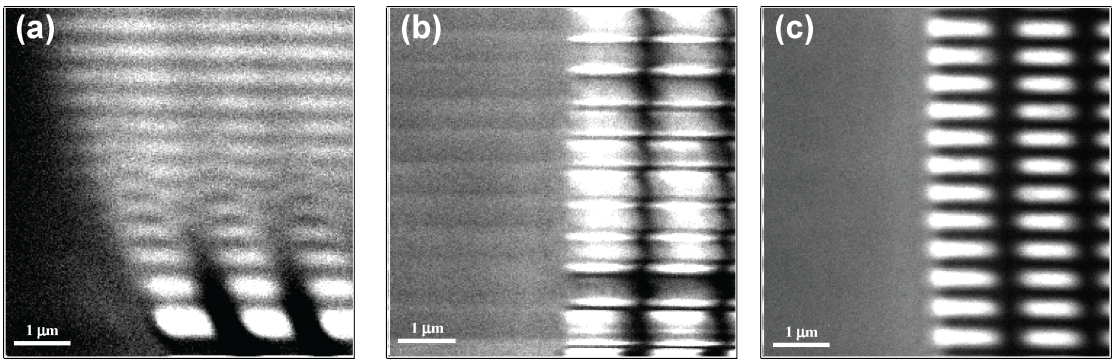

Figure 4.6 Nanomembrane and nanowire area (6 µm x 6 µm) scanned with different environmental parameters: (a) room air conditioning OFF, autofocusing system OFF and thermal control booth OFF; (b) room air conditioning ON, autofocusing system ON and thermal control booth OFF; (c) all three systems are turned ON.

To demonstrate the influence of the environment and the stability of the system, a 6 μm x 6 μm area was scanned which consisted of part of the nanomembrane and 80 nm width nanowires (Figs. 4.6a – 4.6c). A laser wavelength of 532 nm was used. During each scan, the environmental conditions were different. For Fig. 4.6a, the air conditioner of the experimental room, the thermally controlled and the autofocusing system were turned off. This resulted to a gradually degraded image. The initially focused image of the nanowire region became defocused as the scanning progressed. Not even half-way through the scan, the contrast between the nanowires decreased to the point that the nanowires cannot be individually resolved. This was due to the thermal drift present in all three directions. The direction of the drift was influenced by the increase in room temperature, since the air conditioning of the room was also turned off. For Fig. 4.6b, the air conditioning was turned on along with the autofocusing system, but the thermally controlled booth was still turned off. Through the use of the autofocusing system, the nanomembrane and the nanowire areas were clearly identified and the amount of drift lessened in the *x'* and *y'*-directions. But periodic artifacts can be seen in the nanomembrane and in the nanowire areas. This was due to the periodic on and off cycle of the air-conditioner to maintain a constant room temperature. For Fig. 4.6c, the thermally controlled booth was turned on, along with the room air conditioning and the autofocusing system. The thermally controlled booth helped maintain a constant temperature within the vicinity of the microscope and eliminated the unwanted artifacts caused by the cycle of the room air conditioning system.

4.3 ANALYSIS OF STRESS I: LONGITUDINAL OPTICAL PHONON APPROACH [4.1]

4.3.1. LO: Theoretical Approach

The local stress in Si lattice is obtained from Raman shifts by solving the well-known secular equation. In the case of the unpatterned nanomembrane, the equi-biaxial stress ($\sigma_{xx} = \sigma_{yy} = \sigma_0$) model of stress-induced Raman shift for doublet ($\Delta\omega_{xy}$: TO phonons) and the singlet ($\Delta\omega_z$: LO phonons) are [4.22]:

$$\Delta\omega_{xy} = \frac{\left[p\left(S_{11}+S_{12}\right)+q\left(S_{11}+3S_{12}\right)\right]\sigma_0}{2\omega_0} = -3.42\times\sigma_0, \qquad (4.1)$$

$$\Delta\omega_z = \frac{\left[pS_{12} + q\left(S_{11} + S_{12}\right)\right]\left(\sigma_{xx} + \sigma_{yy}\right)}{2\omega_0} = -4.60 \times \sigma_0, \qquad (4.2)$$

where $\Delta\omega_{xy} = \omega_{\varepsilon-SiTO} - \omega_{Si}$ and $\Delta\omega_z = \omega_{\varepsilon-SiLO} - \omega_{Si}$ are expressed in the Raman frequency in each mode in the presence ($\omega_{\varepsilon-Si}$) and absence (ω_{Si}) of stress. S_{11} = 7.68 and S_{12} = –2.14 (in GPa) are the elastic compliance tensor elements, while p = –1.85 and q = –2.31 are the phonon deformation potentials for bulk Si at room temperature [4.23]

The stress relaxation ratio upon patterning at any position in the nanowire is calculated using $R\left(x,y\right) = 1 - \sigma_{nanowire}\left(x,y\right)/\sigma_0$, where σ_0 and $\sigma_{nanowire}$ correspond to the initial stress before nanopatterning and the measured stress in nanowires, respectively [4.24]. The initial stress, σ_0, in the nanomembrane is calculated from the measured Raman shift using Eq. (4.2). However, it is important to note that Eq. (4.2) cannot be used for the extraction of stress in the nanowires, $\sigma_{nanowire}$, mainly because the assumption that shear stress is zero used to obtain the stress is no longer valid as the stress is no longer bi-isotropic in the nanowire due to geometrical constraints and non-uniform rearrangements of atoms near the newly formed free surfaces. In fact, in a nanowire the shearing strain terms at the crystal coordinate are no longer zero due to anisotropic strain relaxation along the nanowire axes. In order to obtain the nanowire stress, I first calculated the strain and stress components in the sample coordinates where shearing terms are all zero due to the symmetry of the structure at the sample coordinate system and then transform them into crystal coordinate [4.24]. At the center of the nanowire, the strain component along the nanowire length ($\varepsilon'_{xx}\left(x',d\right)$) has almost the value of the original membrane, ε_0 , but the stress along the width ($\sigma'_{yy}\left(x',d\right)$) will be dramatically relaxed due to the reduced dimension in this direction. d represents the width of the nanowires. The shear strain component becomes zero in the middle of the nanowire, and the stress component along z' is equal to zero due to free surface boundary conditions; the strain and stress tensors are then expressed as [4.24]

$$\left\{\varepsilon'\left(x',d\right)\right\}=\varepsilon'_{xx}\left(x',d\right)\begin{bmatrix}1 & 0 & 0\\ 0 & \dfrac{s\alpha\left(x',d\right)C_{11}+C_{12}^2-C_{11}\left(C_{12}-H/2\right)}{C_{11}\left(C_{11}+H/2\right)-C_{12}^2} & 0\\ 0 & 0 & \dfrac{-s\alpha\left(x',d\right)C_{12}-2C_{12}C_{44}}{C_{11}\left(C_{11}+H/2\right)-C_{12}^2}\end{bmatrix}, \tag{4.3}$$

$$\left\{\sigma'\left(x',d\right)\right\}=\begin{bmatrix}C'_{11}\varepsilon'_{xx}\left(x',d\right)+C'_{12}\varepsilon'_{yy}\left(x',d\right)+C'_{13}\varepsilon'_{zz}\left(x',d\right) & 0 & 0\\ 0 & \alpha\left(x',d\right)\sigma_0 & 0\\ 0 & 0 & 0\end{bmatrix}, \tag{4.4}$$

where $\alpha\left(x',d\right)=\sigma'_{yy}\left(x',d\right)/\sigma_0$, s = C_{11} +C_{12} – ($2C^2_{12}/C_{11}$) and H = $2C_{44}$ + C_{12} – C_{11}. The elastic constants C_{11} = C_{22} = 166 GPa, C_{12} = C_{21} = 64 GPa, C_{44} = 79.6 GPa, C'_{12} = C_{12} – 0.5H = 35.4 GPa, C'_{11} = C_{11} + 0.5H = 194.6 GPa and C'_{13} = C_{12} = 64 GPa are obtained from Refs. [4.24] and [4.25]. The constant $\alpha\left(x',d\right)$ varies between 0 and 1 and depends upon the diameter of the nanowire. At the limits, $\alpha\left(x',d\right)$ equals 0 for uniaxial stress and 1 for bi-isotropic stress. After substitution, the strain tensor in the sample coordinate reduces to:

$$\left\{\varepsilon'\left(x',d\right)\right\}=\varepsilon'_{xx}\left(x',d\right)\begin{bmatrix}1 & 0 & 0\\ 0 & 1.06\alpha\left(x',d\right)-0.06 & 0\\ 0 & 0 & -0.41\alpha\left(x',d\right)-0.36\end{bmatrix} \tag{4.5}$$

and transformation to the crystal coordinate system results to:

$$\left\{\varepsilon'\left(x',d\right)\right\}=\varepsilon'_{xx}\left(x',d\right)\begin{bmatrix}0.53\alpha\left(x',d\right)+0.47 & -0.53\alpha\left(x',d\right)+0.53 & 0\\ -0.53\alpha\left(x',d\right)+0.53 & 0.53\alpha\left(x',d\right)+0.47 & 0\\ 0 & 0 & -0.41\alpha\left(x',d\right)-0.36\end{bmatrix}. \tag{4.6}$$

Using the strain components above, the solution to the well-known secular equation for the LO phonon mode is expressed as

$$\Delta\omega_z=\omega_{\varepsilon-SiLO}-\omega_{Si}=\frac{\omega_{Si}}{2}\left[p\varepsilon_{zz}\left(x',d\right)+2q\varepsilon_{yy}\left(x',d\right)\right], \tag{4.7}$$

$$\Delta\omega_z = \omega_{\varepsilon-SiLO} - \omega_{Si} = \frac{-\omega_{Si}\varepsilon'_{xx}\left(x',d\right)}{2}\left[1.70\alpha\left(x',d\right)+1.50\right]. \quad (4.8)$$

In Eq. (4.6), there are two unknown parameters, strain $\varepsilon'_{xx}\left(x',d\right)$ along the nanowire long *x'*-axis and the $\alpha\left(x',d\right)$, stress relaxation factor along the nanowire width, which I have to extract from the Raman measurement. However, assuming I detect only LO phonon mode by conventional backscattering geometry, it is impossible to determine the two unknown parameters from the single phonon mode. To circumvent this limitation and obtain the stress in nanowires, it is widely accepted to assume that the stress along the width of the nanowire can be assumed fully relaxed, that is $\alpha\left(x',d\right)=0$, (see for e.g., Refs. 4.15, 4.24 and 4.25 and references therein). Herein, I demonstrate that this assumption is too simplistic leading to an inaccurate analysis of stress. Using Eq. (4.5) and at $\alpha\left(x',d\right)=0$, the stress along the *x'*-axis is given by: $\sigma'_{xx}\left(x',d\right)=168.25\times\varepsilon'_{xx}\left(x',d\right)$. By substituting the strain components in Eq. (4.6), $\varepsilon_{zz}=-0.36\times\varepsilon'_{xx}\left(x',d\right)$ and $\varepsilon_{xx}=0.47\times\varepsilon'_{xx}\left(x',d\right)$, into Eq. (4.7), the stress (in GPa) in the lon axis can be expressed in terms of the measured Raman shift as:

$$\sigma'_{xx}\left(x',d\right)=-225.67\times\frac{\omega_{\varepsilon-Si}-\omega_{Si}}{\omega_{Si}}. \quad (4.9)$$

In an alternative approach, I propose the introduction of an edge structure (edge parallel to *y'*-axis) consisting of a patterned nanomembrane with a practically semi-infinite dimension along *y'* (> 1 cm), which can be assumed as a hypothetical nanowire with an infinite width ($d=\infty$). Eq. (4.8) indicates that there are two unknown parameters, $\varepsilon'_{xx}(x',d)$ and $\alpha(x',d)$, while the experiment only provides the values of $\Delta\omega_z$ (Fig. 4.7b). For $\alpha(x',d)\neq 0$, $\varepsilon'_{xx}(x',d)$ can be determined using the reference structure ($d = \infty$). Here, the nanowire strain profile along *x'*-axis, $\varepsilon'_{xx}(x',d)$, can be taken as comparable to the profile along the same direction in the reference structure, $\varepsilon'_{xx}(x',d=\infty)=\varepsilon'_{xx}(x',d)$, because at an identical length (1 μm) the effect of the newly formed free surfaces should be similar in both systems. In *y'* axis, the reference sample is infinite and thus the initial strain is preserved (i.e., no relaxation

does take place along this axis) suggesting that $\varepsilon'_{yy}(x',d=\infty)$ is equivalent to the initial strain in the unpatterned nanomembrane, ε_0.

Analogously to Eq. (4.8), I introduce an additional anisotropic stress relaxation factor, $\beta(x',d=\infty)=\sigma'_{xx}(x',d=\infty)/\sigma_0$, which represents the relative stress relaxation along x'-axis in the reference structure. Thus, the equation of Raman shift as a function of $\beta(x',d=\infty)$ can be written as:

$$\Delta\omega_z=\omega_{\varepsilon-SiLO}-\omega_{Si}=\frac{-\omega_{Si}\varepsilon'_{yy}\left(x',d=\infty\right)}{2}\left[1.70\beta\left(x',d=\infty\right)+1.50\right] \qquad (4.10)$$

where $\varepsilon'_{yy}\left(x',d=\infty\right)$ is obtained from Raman signal of the unpatterned nanomembrane, whereas $\Delta\omega_z$ is obtained from Raman scans along the *x'*-axis from the edge. By using the obtained values of $\varepsilon'_{yy}\left(x',d=\infty\right)$ and $\Delta\omega_z$, I can determine β. Thus, the strain along the *x'*-axis of the edge sample can be extracted similarly to Eq. (4.5) using β:

$$\varepsilon'_{xx}\left(x',d=\infty\right)=\varepsilon'_{yy}\left(x',d=\infty\right)\left[1.06\beta\left(x',d=\infty\right)-0.06\right]. \qquad (4.11)$$

This strain is only a function of *x*' and varies from *x'* = 0 (edge) to an *x'* = 0.5 mm around the nanowire center. The strain component, $\varepsilon'_{yy}\left(x',d=\infty\right)$ (parallel to the edge) remains unchanged. This approach is analogous to the semi-infinitely wide line structures used in the theoretical treatment developed earlier by Jain et *al*. [4.24]. The measured Raman shifts from the edge structures were attributed mostly to the strain along the *x'*, $\varepsilon'_{xx}\left(x',d=\infty\right)$ and the constant strain component in the *y*'-direction, ε_0 which is the same as the strain obtained from the nanomembrane. In the following, I test the validity of these two approaches.

4.3.2 LO: Experimental Results and Discussion

Multiwavelength experiments utilizing 442 nm and 355 nm lasers for interface effects investigation [4.1]. Fig. 4.7a shows the Raman spectra obtained with the 442 nm excitation at the center of the nanowires using $z'\left(x',x'\right)\bar{z}'$ configuration. I

reported recently that TO phonons can be effectively observed using high NA illumination [4.12]. The observed TO-active Raman shift are upshifted relative to LO phonons as predicted by the association of Eq (4.1) and (4.2) [4.12]. This upward shift in the Raman spectra arising from TO phonon can be easily mixed with LO phonon signal and consequently overestimate the level of stress relaxation. This is because the spectral split between LO and TO phonons is small to be resolved by peak function fits. Proper selection of sample azimuth, incident polarization and analyzer orientation is therefore necessary to accurately uncover the stress behavior in strained Si nanowires. I observed that the $z'(x',x')\bar{z}'$ is constantly lower than the $z'(y',y')\bar{z}'$ configuration for all regions in the nanowires. Under $z'(x',x')\bar{z}'$, that is the incident polarization is parallel to the nanowire axis, the observed Raman is predominantly due to LO-phonon. For the case of $z'(y',y')\bar{z}'$, where incident polarization is perpendicular to the nanowire axis, the observed Raman consists of both LO- and TO-phonons [4.22]. This is because in $z'(y',y')\bar{z}'$ configuration the transverse (E_y) electric field is efficiently converted to E_z-field when introduced to the (110) and (-110) sidewalls, which results in an effective excitation TO phonons [4.12]. The TO scattered Raman is efficiently collected by backscattering geometry [4.22]. From previous work [4.12], I experimentally verified that TO phonon in nanowires has higher Raman peak shift relative to LO-phonons. This explains why the Raman peak shift for $z'(y',y')\bar{z}'$ is higher and broader (data not shown) than $z'(x',x')\bar{z}'$. Hence, in order to obtain an accurate in-plane tensile stress from LO-phonons, it is important to choose the incident polarization parallel to the nanowire.

Here, the Raman signal is collected from the whole thickness of the nanowire (i.e., 15 nm). The measured spectra are “background-free” and contain only the intrinsic Si-Si Raman shift peak of the probed nanowire because of the introduction of Ge interlayer described above. It should be noted that the dominant contribution to the measured Raman shift originated from the LO phonon mode from both the top (001) surface and the long axis sidewalls, [110], based on the Raman tensor calculation under *x'*-polarized light. For the sake of comparison, Raman spectrum of initial strained nanomembrane (solid black line) as well as the Si-phonon peak position in bulk Si (broken vertical lines) is also shown. Table 4.1 summarizes the Raman peak and spectral width for all the observed structures. As the width decreases, the Raman peaks shift upward with respect to the position of the Si-phonon peak of the initial strained Si layer.

Table 4.1. Summary of Raman peak and spectral width at center of single nanowires.

Initial strained layer	15nm-thick ($\omega_{\varepsilon-SiLO} = 515.42\ cm^{-1}$ $\Delta\upsilon = 4.86\ cm^{-1}$)		
Nanowire width, *d* (nm)	80	50	30
Peak, $\omega_{\varepsilon-SiLO}$ (cm^{-1})	516.43	516.99	517.42
Width, $\Delta\upsilon$ (cm^{-1})	5.09	5.20	5.16

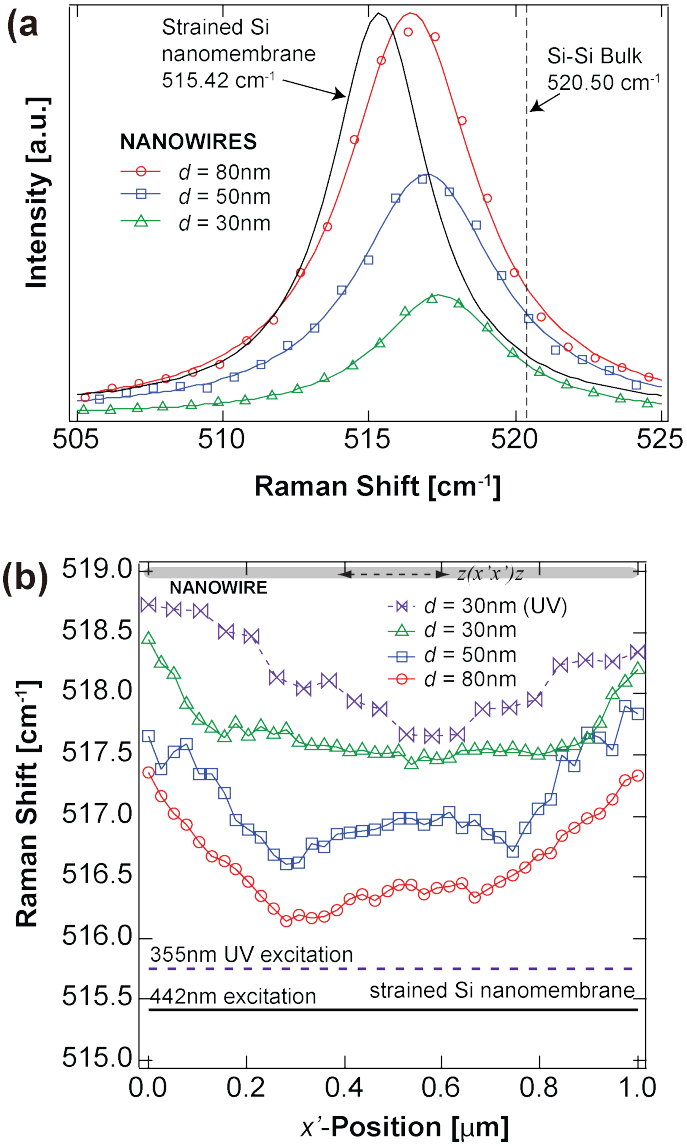

Figure 4.7. (a) Raman spectra recorded at the center of nanowires with lateral dimensions of 30 nm (triangles), 50 nm (squares) and 80 nm (circles). The Raman spectrum of the unpatterned strained Si is shown in solid black lines. The vertical dashed line denotes the Si–phonon peak position in bulk (unstrained) Si. (b) Profile of the Raman peak for nanowire obtained under the *z(x'x')z* configuration. The solid and dashed line represents the Raman peak position of the initial strained Si nanomembrane using 442 nm (515.75 cm^{-1}) and 355nm (515.42 cm^{-1}) excitation, respectively [Taken from Ref. 4.1 with permission from IOP Publishing].

No significant broadening in the nanowire Si-Si Raman mode is, however, observed. It is noticeable that Si-Si peak position of the investigated nanowires is upshifted with respect to its position in the initial ($\omega_{\varepsilon-SiLO} = 515.42$ cm^{-1}) strained nanomembrane. This shift is indicative of partial relaxation of stress during the process of nanowire pattering using reactive ion etching.

To obtain more insights into the complex redistribution of stress as nanowire dimension shrinks, the profiles of the Raman shift for nanowires of varying width are plotted in Fig. 4.7b. The nanowires were scanned along the *x'*-axis with a step size of 25 nm using $z'\left(x',x'\right)\bar{z}'$ configuration. The Raman shift for *d* = 30 nm using 355 nm (UV) excitation is also displayed in Fig. 4.7b. At this excitation, only the top 10 nm of the nanowire thickness is probed. For comparison, the Raman shifts measured from the original membrane are indicated with solid (442 nm) and dashed (355 nm) lines.

Fig. 4.8 shows the stress profiles using the (a) first, $\alpha\left(x',d\right)=0$, and (b) second, $\varepsilon'_{xx}(x',d=\infty)=\varepsilon'_{xx}(x',d)$, approaches. Regardless of the approaches used, the profiles measured for all the nanowires display a qualitatively similar behavior characterized by a more pronounced relaxation of stress near the nanowire edge. Moreover, as general trend, the residual stress profile shows plateau-like profiles in the region around the center. The breadth of this region is sensitive to the nanowire width and varies from ~400 nm at *d* = 50 or 80 nm to ~700 nm at *d* = 30 nm. The enhanced relaxation near the edges results from the additional free surface as compared to the rest of the nanowire (four *vs*. three facets). As described below, this constant stress values away from the edges can be attributed to the nearly constant and highly retained stress at the buried strained-Si/SiO_2 interface.

The obtained initial stress from the nanomembrane using Eq. (4.2) was plotted (solid black) to evaluate the validity of the first approach based on the assumption of a full relaxation along the nanowire width ($\alpha\left(x',d\right)=0$). Strikingly, the stress profiles along the long-axis obtained using this approach is higher than the original stress in the nanomembrane. This discrepancy indicates that the assumption of a full relaxation along the width is inaccurate and that stress is not uniaxial. In the following, I focus my analysis on the second approach.

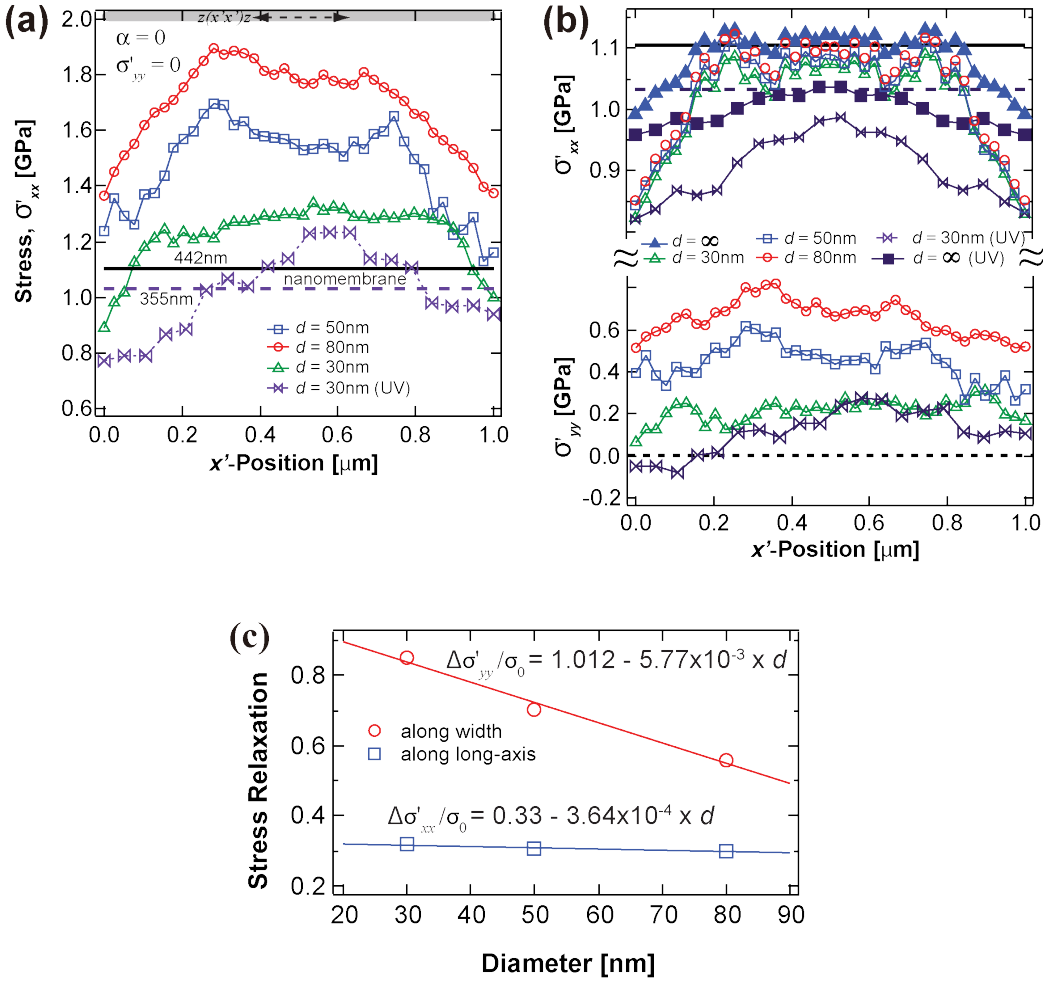

Figure 4.8. Stress Profiles in single nanowires obtained under different excitation wavelengths using the first (a) and second (b) approaches described in the text. (c) Stress relaxation dependence estimated at the center of the nanowire as a function of the nanowire diameter [Taken from Ref. 4.1 with permission from IOP Publishing].

I first calculated the strain from Eqs. (4.10) and (4.11) using the measured Raman shift scanned from *x*' = 0 (edge) to *x*' = 0.5 mm (towards the center) sample with semi-infinite width. The strain values are then used in Eqs. (4.8) and (4.9) to calculate the stress at each position. Fig. 4.8b shows the obtained stress profiles $\sigma'_{xx}(x',d)$ and $\sigma'_{yy}(x',d)$. The calculated stress values along the *x*'-direction are below the original stress of the membrane. It is also interesting to note that the profile of the stress along *x*'-direction of the nanowires is similar and with stress values very close to stress of the edge sample, suggesting that stress is preserved at the center. Moreover, the stress along *x*'-direction at edges (*x*' = 0 and *x*' = 1.0 μm) is the same ($\sigma'_{xx}(x'd) \approx 0.85$ GPa) for all nanowires regardless of excitation wavelengths. This is not the case when a full relaxation is assumed along the width, which indicates that this assumption is fraught with large uncertainties. On the other hand, I can clearly

see from the profile along the width, $\sigma'_{yy}(x',d)$, that the nanowire is still under a biaxial stress. The stress profile along the width is relatively constant through the whole length of the nanowire unlike along the long-axis where pronounced relaxation is observed at the edges. Furthermore, a full relaxation of stress is only observed at the edge of the nanowire with d = 30 nm. For this set of nanowires, the stress at the center reaches a value of ~200 MPa. This behavior is observed for both excitation wavelengths. At d = 80 nm and d = 50 nm, the stress is well above the fully relaxed region (gray dashed zero line). This result indicates that the overall average stress in the nanowire is biaxial but not bi-isotropic. Note that at an excitation wavelength of 442 nm the buried strained-Si/SiO_2 interface is also probed. Here, the stress between 200 ≤ x' ≤ 800 nm is comparable to the initial stress in the nanomembranes, whereas at 355 nm the initial stress in only preserved in the region 450 ≤ x' ≤ 550 nm. Fig. 8c exhibits the relaxation ratio at the center of the nanowire as a function of nanowire diameter. It is noticeable that the extent of this relaxation along the width exhibits a linear behavior as a function of the nanowire width: $\Delta\sigma'_{yy}/\sigma_0 = 1.01 - 5.77\times10^{-3}\times d$. The relaxation along the long-axis is small and remains unchanged with the nanowire width.

Interestingly, the combination of two excitation wavelengths provides new insights into the complex behavior of stress in nanowires. Fig. 4.9 shows the depth dependence of stress profiles along the two in-plane axes for nanowire with a width of d = 30 nm under $z'(x'x')\bar{z}'$ condition using different excitation wavelength (penetration depth) namely: 442 nm (~168 nm) and 355 nm (~10 nm). It is noteworthy that Raman shifts measured using the 355 nm laser are centered around higher wavenumbers as compared to those obtained using the 442 nm excitation as shown in Fig. 4.7b. The Fig. 4.9a also displays the original stress (lines) in the unpatterned nanomembrane obtained using the two-excitation wavelengths as well. The small difference in the measured stress using the two excitations suggests that the region near the surface of the nanomembranes is slightly relaxed.

After patterning of the nanowires, the stresses are observed to be more relaxed in both 442 nm and 355 nm excitations. However, the interesting observation is that the stress relaxation behavior as obtained by the 355 nm excitation decreases monotonously towards the center of the nanowire, which remains highly strained. At the 442 nm excitation, the stress relaxation plateaus in the region 200 ≤ x' ≤ 850 nm.

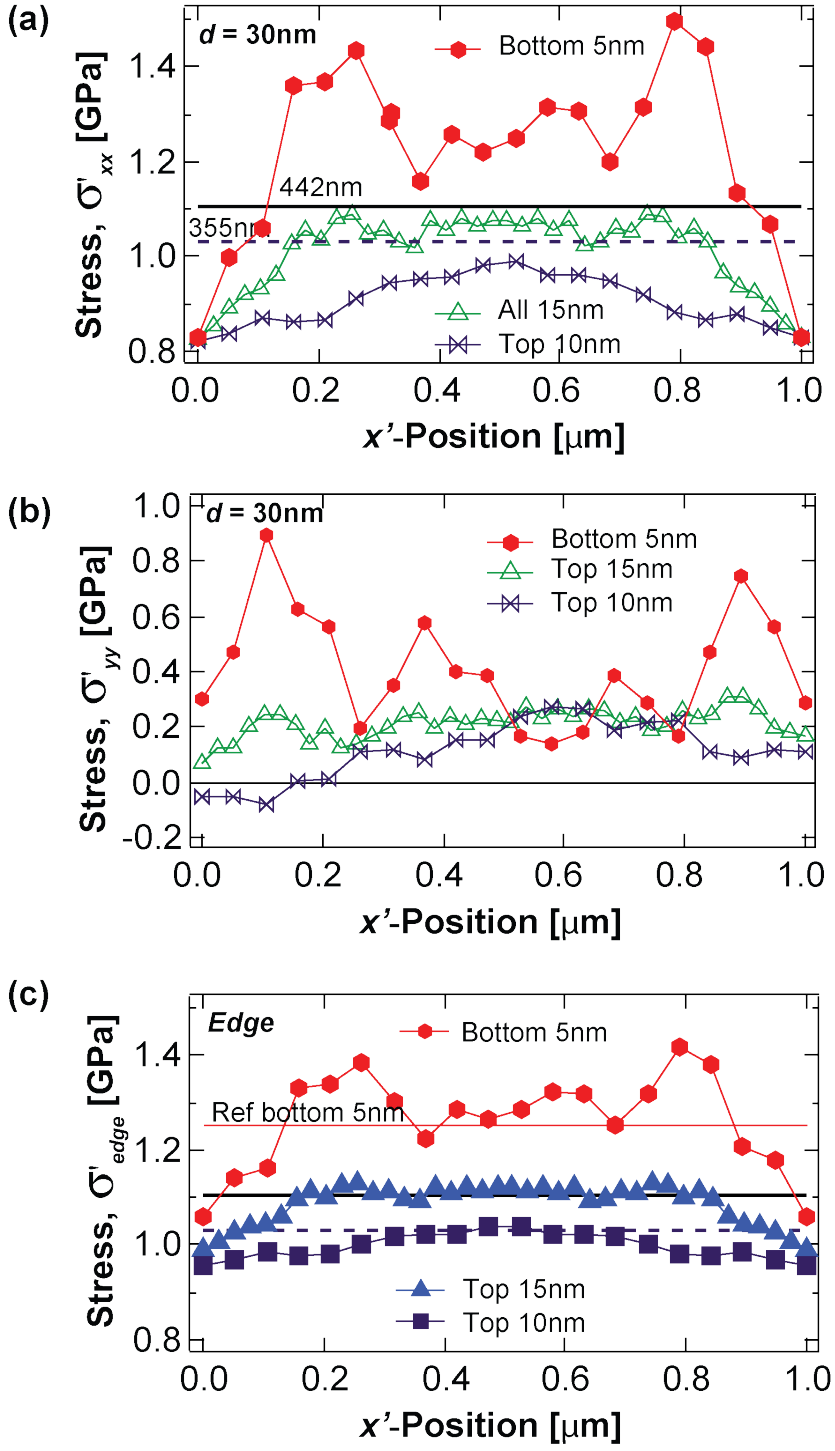

Figure 4.9. Stress profiles along the (a) *x'*- and (b) *y'*-axis for nanowire with a width of *d* =30 nm at different depths obtained using the two excitation wavelengths (penetration depths): 442 nm (~168 nm) and 355 nm (~10 nm). The horizontal solid (442 nm) and dashed (355 nm) lines marked the initial strain in Si nanomembrane. (c) Stress profiles at different depths in the reference sample with a semi-infinite edge.

This dissimilarity in stress behavior between the two-excitation wavelengths is indicative of the non-uniform distribution of the in-plane stress along the nanowire thickness. More precisely, the fact that the stress measured using a laser with the shallower penetration depth is systematically smaller than the value averaged over the whole thickness provides direct evidence that the region near the nanowire-oxide interface maintains a high level of stress. By combining the stress profiles measured at 442 nm (σ'^{15nm}_{xx}) and 355 nm (σ'^{10nm}_{xx}) excitations, I extract the stress profile in the bottom 5 nm of the nanowire along the *x*'-direction $\sigma'^{5nm}_{xx}\left(\sigma'^{5nm}_{xx} = 3\times\sigma'^{15nm}_{xx} - 2\times\sigma'^{10nm}_{xx}\right)$ (Fig. 9a). Similarly, the stress profile along *y*'-direction is depicted in Fig. 4.9b. For the two in-plane axes, the obtained stress profiles are qualitatively identical but remarkably different from the profiles measured for the top 10 nm or over the whole nanowire thickness. Particularly, the part of the nanowire near the interface becomes under a higher stress especially in the region about 100 to 200 nm away from the edge in a qualitative agreement with finite element simulations (not shown). In this region, close stress values are recorded for the two in-plane directions indicating that the interface with the oxide preserves almost the initial isotropy (i.e., a biaxial strain). Interestingly, the stress in *x'*-direction reaches values that are higher than the initial stress indicating that the contraction of the lattice near the newly formed free surfaces is accompanied by a strong distortion close to the interface with the oxide. This means that when the lattice near the edges moves inwards it drags the underlying substrate leading to a complex redistribution of stress. Above ~200 nm away from the edge, the stress decreases slightly along the nanowire length to stabilize around 1.2 GPa. The decrease is more significant along the width. For this direction, the in-plane stress remains the same independently of the depth in the nanowire. A similar behavior is also observed for the edge sample as shown in Fig. 9c. The only noticeable difference in the bottom 5 nm stress values along the long axis between the *d* = 30nm nanowire and reference sample is located at the edges. The bottom 5 nm stress at the edge is ~1.06 GPa, which is just above the stress measured with 355 nm excitation whereas for *d* = 30 nm nanowire, the bottom 5 nm stress is 0.83 GPa. Towards the center, the bottom 5 nm stress values remain unchanged.

Nanomembrane edge induced stress field [4.19]. I scanned a 12 μm x 6 μm area and Figure 4.10 shows the intensity and the Raman shift images of the 30 nm, 50 nm and 80 nm width ε-SiNWs. From the intensity images, various localized defects are observed, particularly in the 50 nm (Fig. 10b) and 30 nm (Fig. 10c) ε-SiNWs. These

defects become more pronounced in the Raman shift image. It is interesting to point out that there are defects only evident in the Raman shift image when compared its corresponding intensity image. Examples of such occurrences are in the Raman shift image of the 80 nm width ε-SiNWs and some part of the 50 nm width ε-SiNWs. This localized defect has significant effect on the Raman shift distribution in the ε-SiNWs as it lowers the supposed Raman shift, which represents higher stress. For proper analysis of the data, the defect areas were avoided. I also observed that the Raman shifts of the nanowires are blue shifted from the nanomembrane. This means that the Raman shifts of the ε-SiNWs are higher than the nanomembrane and that stress upon patterning occurs due to the formation of free surfaces.

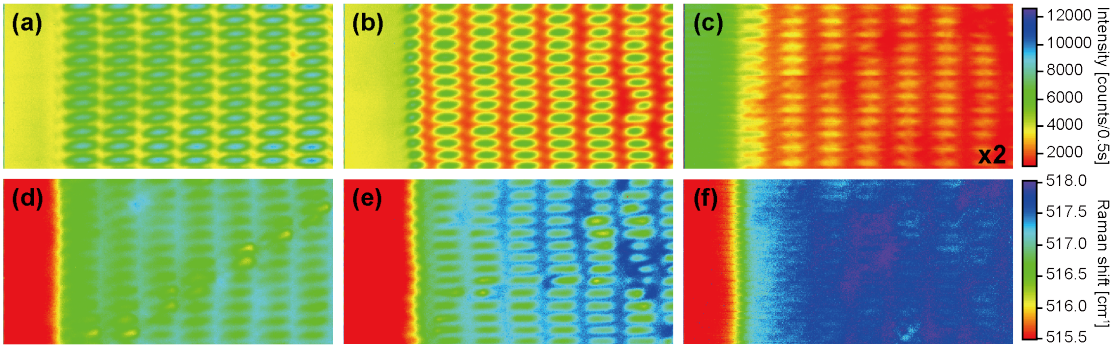

Figure 4.10. Intensity images of NWs with length of 1 μm and width of (a) 80 nm, (b) 50 nm and (c) 30 nm while (d), (e) and (f) are the corresponding Raman shift images. Image size is 12 μm x 6 μm with step size of 25 nm/pixel.

From the images in Fig. 4.10, the behavior of the Raman shift and the intensity signal as the NW approaches the edge was studied. Horizontal line profiles were taken at specific areas of the images, avoiding the defects. The black lines in Figure 4.11 denote the intensity line profile while the red lines denote the Raman shift line profile for (a) 80 nm, (b) 50 nm and (c) 30 nm width NWs. As seen from Fig. 4.11, a local maximum in the intensity line profile corresponds to a local minimum in the Raman shift line profile, which is indicative of the center location of each ε-SiNW. In the Raman shift, a redshift occurs for ε-SiNWs closer to the nanomembrane edge as compared to the ε-SiNWs farther from the edge. The affected nanowires are within 4 μm from the nanomembrane edge and exhibits the tuning of the stress that is induced by the nanomembrane edge. It should be noted that the half portion of ε-SiNWs at the left most row of the 50 nm width ε-SiNWs are embedded in the nanomembrane edge while the ones in 30 nm and 80 nm width are separated from the edge due to the fabrication process. This is also confirmed by the separate measurement by optical reflection imaging.

Three regions of interests have been identified and for ease of discussion shall be called: *near* edge, *middle* region and *far* from edge. Intensity images of the ε-SiNWs with 80 nm and 30 nm widths (Fig. 4.11a and 4.11c) show distinct edges of the ε-SiNW row. I denote the column of the NWs with 80 nm and 30 nm width at the boundary of the nanomembrane to be the *near* edge region while the second column from the edge of the 50 nm width ε-SiNWs to be the *near* edge region. The *middle* region of each ε-SiNW was taken at the column right after the *near* edge column while the *far* from edge region was taken at the 5th column from membrane for the 80 nm and 30 nm width NW and 6th column from the membrane for the 50 nm width ε-SiNWs.

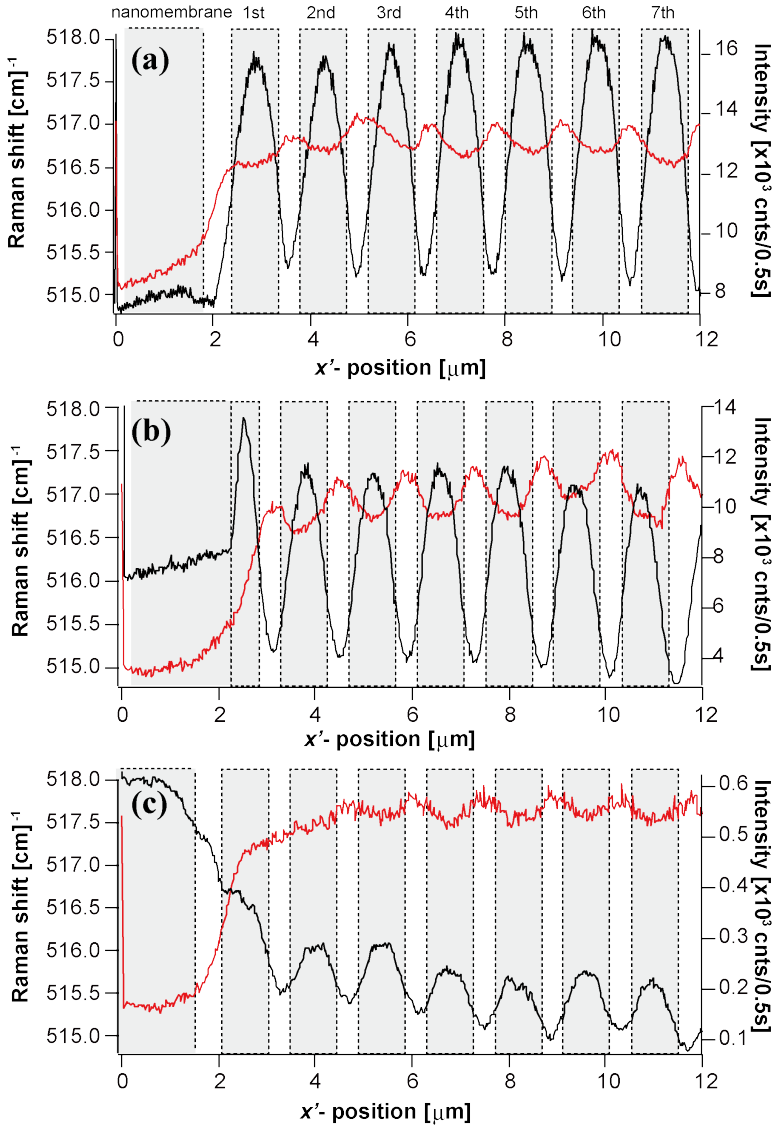

Figure 4.11. Intensity (black) and Raman shift (red) line profiles of ε-SiNWs with width of (a) 80 nm, (b) 50 nm and (c) 30 nm. The defects observed in Figure 4.10 were avoided when acquiring this data.

Using the Raman shift at the three identified regions, I determined the stress profile (σ'_{xx}) using the method outlined in Section 4.3.1. This method is usually applicable to the ε-SiNWs located *far* from the edge of the nanomembrane, since the nanomembrane affects the stress distribution of the NWs *near* it. I assumed that the stress distribution along the *x'*-axis of the ε-SiNWs will be modified as the ε-SiNWs approach the edge due to the higher stress induced through the substrate. As was shown in the multiwavelength experiment, the interface has a large effect on the stress in the ε-SiNWs. The stress distribution along the *y'*-axis, however, will remain unchanged – $\sigma'_{yy}\left(x'_{\text{far from edge}}, d\right) = \sigma'_{yy}\left(x'_{\text{middle region}}, d\right) = \sigma'_{yy}\left(x'_{\text{near edge}}, d\right)$ – since there is no edge present perpendicular to ε-SiNWs *y'*-axis.

Figure 4.12a shows the Raman shift of 30 nm, 50 nm and 80 nm width ε-SiNWs used for stress along *x'*-axis calculation, with the latter shown in Fig. 4.12b. For a given ε-SiNW width, the Raman shift decreases as one moves from the *far* edge region to the *near* edge region. All profiles show an increase in the Raman shift towards the center of the nanowire, indicating that a high amount of stress is maintained at the center of the nanowire, with the exception of the Raman shift profile of 30 nm width ε-SiNW, which is characterized by a steady increase in the Raman shift from the near nanomembrane side to the other edge of the ε-SiNW.

The stress behavior along the length of the nanowire (Fig. 4.12b) displays position dependence relative to the nanomembrane, particularly in the nanowire closest to the nanomembrane except the 30 nm width ε-SiNW near the edge. The side of the ε-SiNW near the nanomembrane edge exhibits higher stress than the center, indicating that the edge has bigger effect on it than its intrinsic stress. The effect of the nanomembrane edge on the ε-SiNWs near the edge also depends on the ε-SiNW width, as the stress along the *x'*-axis relaxes as the width increases. Also, as the ε-SiNW is farther away from the nanomembrane edge, the behavior of the stress along the length of the wire becomes symmetric, which is consistent with the multiwavelength experiments explained in the earlier part of this section. Independent of the ε-SiNWs' width, I found that the stress relaxes as the nanowire moves farther away from the nanomembrane. This is is because the stress from the highly stress nanomembrane is transferred to the smaller and less stressed ε-SiNW s via the substrate. This effect lessens as the ε-SiNW moves away from the nanomembrane.

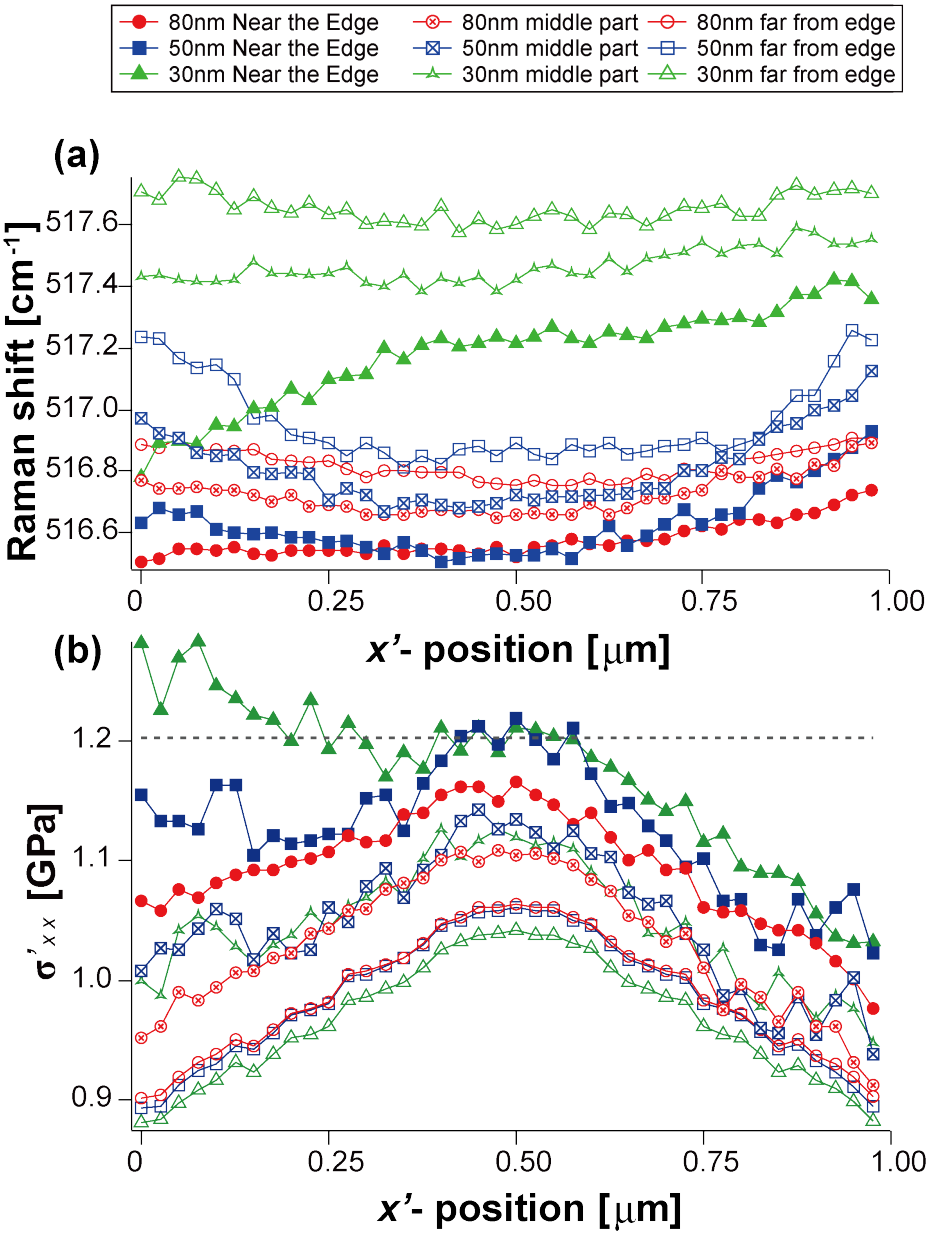

Figure 4.12. Raman shift along the *x'*-axis of the ε-SiNWs show that the Raman shift (a) increases from the *near* edge to the *middle* region up to the *far* from edge. (b) The stress along the *x'*-axis exhibits relaxation from the center to the going to the edge of the NW, with NWs *near* the edge having higher stress compared to the *middle* part and *far* from edge region. Gray dashed line indicates the stress on an unpatterned nanomembrane.

4.4 ANALYSIS OF STRESS II: TRANSVERSE OPTICAL PHONON SPLITTING APPROACH [4.2]

4.4.1 TO: Theoretical Approach

In this method, both TO phonon modes are simultaneously excited using the cross-polarization configuration by rotating the polarizer 90º. It is possible to detect these phonon modes because of the use of the high NA objective lens. Since both phonon modes are present, it is necessary to separate the peaks of the two TO phonon modes during data analysis. This is done through double Lorentzian fitting. In the case of nanowires, the stress is anisotropically relaxed as discussed in Chapter 3. In this case, the degenerate doublet mode $\Delta\omega_{xy}$ (TO phonon modes) in Eq. (4.1) is split into two modes, $\Delta\omega_{TO1}$ and $\Delta\omega_{TO2}$, which are given by [4.26]:

$$\left.\begin{aligned}\Delta\omega_{TO1}(x') &= -2.88\sigma'_{xx}(x') - 0.54\sigma'_{yy}(x'),\\ \Delta\omega_{TO2}(x') &= -0.54\sigma'_{xx}(x') - 2.88\sigma'_{yy}(x'),\end{aligned}\right\} \tag{4.12}$$

where the numerical values were derived using the PDPs reported in Ref. 4.27 and the elastic compliance tensor reported in Ref. 4.28. The values for $\Delta\omega_{TO1}$ and $\Delta\omega_{TO2}$ can be obtained experimentally and through simple algebraic manipulation, both stresses σ'_{xx} and σ'_{yy} can be directly solved. Eq. (4.12) was derived by Kosemura, et. al. in Ref. [4.29] and their derivation is briefly summarized in this section.

I assume a linear relationship between the force constant ΔK and strain in the crystal coordinate system, wherein x : [100], y : [010] and z : [001]. I define ΔK as

$$\Delta K = A\varepsilon, \tag{4.13}$$

$$A = \begin{pmatrix} p & q & q & 0 & 0 & 0\\ q & p & q & 0 & 0 & 0\\ q & q & p & 0 & 0 & 0\\ 0 & 0 & 0 & 2r & 0 & 0\\ 0 & 0 & 0 & 0 & 2r & 0\\ 0 & 0 & 0 & 0 & 0 & 2r \end{pmatrix}, \tag{4.14}$$

where ε is a strain tensor and *A* is a fourth-rank tensor with PDPs *p*, *q*, and *r*. The coordinate transformation for ε-SiNWs fabricated on a (001) Si in the direction of [110] (just like my sample and those found in actual transistors), use second-rank and fourth-rank tensors to move from the crystal coordinates to sample coordinates. In the sample coordinate system of *x'* : [110], *y'* : [-110], and *z'* : [001]. These tensor equations are:

$$T_{ij} = a_{ik} a_{jl} T_{kl}, \tag{4.15}$$

$$T_{ijkl} = a_{im} a_{jn} a_{ko} a_{lp} T_{mnop}, \tag{4.16}$$

where *T* and *a* are second- or fourth- rank tensors and a transformation matrix, respectively. Therefore, Eq (4.13) becomes

$$\Delta K' = A' \varepsilon', \tag{4.17}$$

where the prime refer to the sample coordinate system in (x',y',z'). The secular equation of $\Delta K'$ is then defined as

$$\begin{vmatrix} \Delta K'_{xx} - \lambda & \Delta K'_{xy} & \Delta K'_{xz} \\ \Delta K'_{xy} & \Delta K'_{yy} - \lambda & \Delta K'_{yz} \\ \Delta K'_{xz} & \Delta K'_{yz} & \Delta K'_{zz} - \lambda \end{vmatrix} = 0, \tag{4.18}$$

where λ is the eigenvalues. For anisotropic biaxial stress, the second-rank stress tensor is given by

$$\sigma' = \begin{pmatrix} \sigma'_{xx} & 0 & 0 \\ 0 & \sigma'_{yy} & 0 \\ 0 & 0 & \sigma'_{zz} \end{pmatrix}, \tag{4.19}$$

where σ'_{xx} and σ'_{yy} are the stress components in the [110] and [-110] directions, respectively. As explained in Chapter 3, the presence of stress can change the optical-phonon frequencies and also the Raman tensors. But in the special case wherein the stress tensor has only diagonal components, the Raman tensor does not change. Therefore, the polarization selection rules for stress-free Si and Si experience biaxial stresses σ_{xx} and σ_{yy} are the same. The sample coordinate Raman tensors are given by Eq. (3.8) in Chapter 3. The stress tensors are related to the strain tensors by Hooke's law:

$$\varepsilon' = S' \sigma', \tag{4.20}$$

$$S = \begin{pmatrix} S_{11} & S_{12} & S_{12} & 0 & 0 & 0 \\ S_{12} & S_{11} & S_{12} & 0 & 0 & 0 \\ S_{12} & S_{12} & S_{11} & 0 & 0 & 0 \\ 0 & 0 & 0 & S_{44}/4 & 0 & 0 \\ 0 & 0 & 0 & 0 & S_{44}/4 & 0 \\ 0 & 0 & 0 & 0 & 0 & S_{44}/4 \end{pmatrix}, \tag{4.21}$$

where S is the elastic compliance tensor and its individual components, S_{11}, S_{12}, and S_{44} were defined earlier along with Eqs. (4.1) and (4.2). The elastic compliance tensor S is transformed to sample coordinates using Eq. (4.16) to solve for the strain tensor ε'. Then solving the secular equation, Eq. (4.18), the eigenvalues λ_j can be calculated. The eigenvalues take the same form as Eqs. (3.10) and (3.11) in Chapter 3. I can then get expressions that relate the shift of the Raman shift to the amount of stress present in Si. These are

$$\begin{aligned} \Delta\omega_{TO1} &= \frac{\lambda_1}{2\omega_0} \\ &= \left[\frac{p\left(S_{11}+S_{12}\right)+q\left(S_{11}+3S_{12}\right)+rS_{44}}{4\omega_0}\right]\times\sigma'_{xx} \\ &\quad + \left[\frac{p\left(S_{11}+S_{12}\right)+q\left(S_{11}+3S_{12}\right)-rS_{44}}{4\omega_0}\right]\times\sigma'_{yy}, \end{aligned} \tag{4.22}$$

$$\begin{aligned} \Delta\omega_{TO2} &= \frac{\lambda_2}{2\omega_0} \\ &= \left[\frac{p\left(S_{11}+S_{12}\right)+q\left(S_{11}+3S_{12}\right)-rS_{44}}{4\omega_0}\right]\times\sigma'_{xx} \\ &\quad + \left[\frac{p\left(S_{11}+S_{12}\right)+q\left(S_{11}+3S_{12}\right)+rS_{44}}{4\omega_0}\right]\times\sigma'_{yy}, \end{aligned} \tag{4.23}$$

$$\begin{aligned} \Delta\omega_{LO} &= \frac{\lambda_3}{2\omega_0} \\ &= \left[\frac{p\left(S_{11}+S_{12}\right)+q\left(S_{11}+3S_{12}\right)+rS_{44}}{2\omega_0}\right]\times\left(\sigma'_{xx}+\sigma'_{yy}\right). \end{aligned} \tag{4.24}$$

Solving Eqs (4.22) – (4.24) using the PDPs reported by Anastasskis, et. al. in 1990, results to Eq. (4.12).

4.4.2 TO: Experimental Results and Discussion

Linear polarization in the $z'(x'y')\bar{z}'$ is used. It was shown in Chapter 3 that in this polarization configuration, TO phonon modes are predominantly detected, particularly in the case of nanowires. To extract the TO phonon peaks, double Lorentzian fitting was used, based on the results of the simulation suggesting that the detected signal consists only of TO_1 and TO_2 (negligible LO intensity) with equal intensity due to symmetry of the nanowire with respect to its orientation in the sample coordinate system. This observation was supported by numerical simulations, wherein the TO/LO ratio was computed for varying nanowire widths using the same $z'(x'y')\bar{z}'$ polarization configuration as that in experiment. From the simulations, it was found that the TO/LO ratios for the 80 nm, 50 nm and 30 nm nanowires are 23.56, 54.89 and 84.57, respectively. These values are very large as compared to the TO/LO ratio for the nanomembrane, which is 0.94. This means that for nanowires, the LO contribution is very small to the point that it is negligible. In contrast, previous work based on $z'(x'x')\bar{z}'$ predominantly detects only LO phonon mode [4.12].

Verifying the validity of the numerical simulations. To verify the validity of the numerical simulations, experiments were made on ε-Si nanomembranes under both $z'(x'x')\bar{z}'$ and $z'(x'y')\bar{z}'$ configurations. For a nanomembrane, it is reasonable to show that it is experiencing bi-isotropic strain. From the simulations discussed in Chapter 3, two peaks – LO and TO – are present. The LO peak was determined using the LO-active configuration $z'(x'x')\bar{z}'$, $\omega_{\varepsilon-SiLO}$ = 514.97 cm^{-1} as shown in Fig. 4.13a. Thus the TO frequency can be extracted to be $\omega_{\varepsilon-SiTO}$ = 516.26 cm^{-1} by Eqs. (4.1) and (4.2). In order to obtain the experimental TO/LO ratio, these LO and TO Raman frequencies are used for double Lorentzian fitting of TO-active configuration in Fig. 4.13b. The experimental TO/LO ratio was computed to be 0.944, which is in good agreement with the calculated value of 0.94 extracted in Chapter 3. Thus validating the soundness of my simulations.

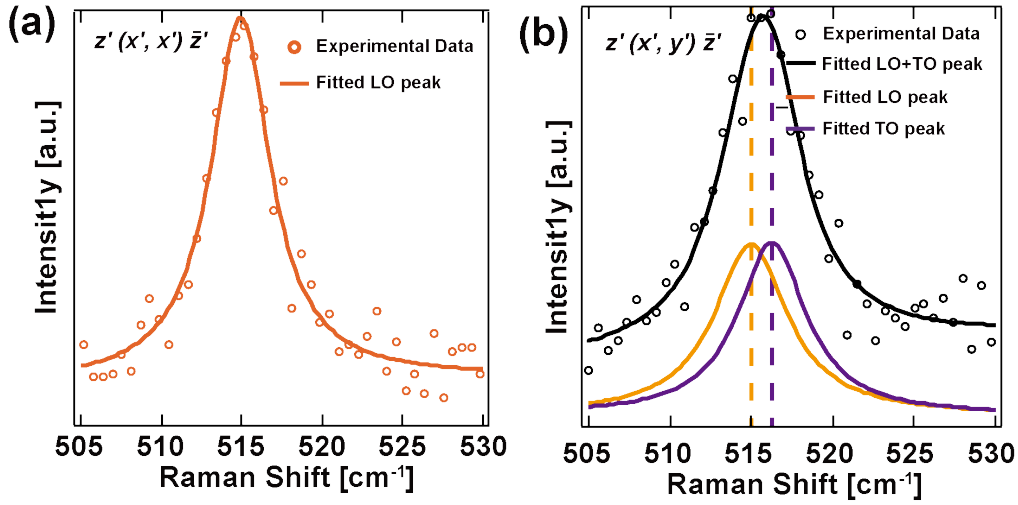

Figure 4.13 (a) Raman spectrum taken on the unpatterned ε-Si nanomembrane using $z'(x',x')\bar{z}'$ configuration. Only LO Raman signal is detected which peaked at 514.97 cm^{-1}. (b) Raman spectrum taken on the unpatterned ε-Si nanomembrane using $z'(x',y')\bar{z}'$ configuration. Singlet LO – peaked at 514.97 cm^{-1} – and doublet TO – peaked at 516.26 cm^{-1} – are detected in this configuration.

Characterization of anisotropic stress relaxation through the detection of TO phonon splitting. Figures 4.14a – 4.14c show the experimentally obtained Raman spectra at the center of the nanowire for 80 nm, 50 nm and 30 nm widths, respectively. These spectra were obtained under TO-active configuration wherein the contributions from the LO peak are negligible as supported by numerical simulations. The red vertical lines in Fig. 4.14a indicate the TO_1 (515.96 cm^{-1}) and the TO_2 (517.71 cm^{-1}) Raman shift peak for the 80 nm width nanowire. The difference between the two peaks is $\Delta\omega_{TO\_80}$ =1.75 cm^{-1}. This difference in the TO peaks is related to the strain anisotropy in the nanowire as illustrated in Fig. 3.3c in Chapter 3. Similarly, for the 50 nm nanowire, the blue vertical lines in Fig. 4.14b indicate the TO_1 Raman shift peak at 515.84 cm^{-1} and the TO_2 Raman shift peak at 517.75 cm^{-1}. The difference between the two peaks is $\Delta\omega_{TO\_50}$ = 1.91 cm^{-1} and is found to be slightly higher than that of 1.75 cm^{-1} for the 80 nm-wide nanowire. Figure 4.14c shows the Raman spectra from the 30 nm-wide nanowire. The signal is relatively weaker than the Raman spectra obtained from the 80 nm and 50 nm nanowires due to the smaller volume probed as compared to the wider nanowires. The green vertical lines denote the TO_1 (515.6 cm^{-1}) and TO_2 (518.32 cm^{-1}) Raman shift peak. The splitting is more apparent at this width and the difference between the two peaks is $\Delta\omega_{TO\_30}$ = 2.72 cm^{-1}. This indicates that the difference in the TO peaks tend to increase with smaller widths of the nanowire. Note that this is the first

experimental demonstration of TO_1 and TO_2 splitting in (001)-oriented silicon. The observed behavior is summarized in Fig. 4.14d displaying the TO_1 and TO_2 Raman shift peak as a function of the nanowire width. As a reference, the Raman peak of the nanomembrane is also shown in this figure. Based on the experiment on the unpatterned strained silicon nanomembrane, which can be considered as an infinitely wide nanowire, the extracted TO phonon frequency ω_{TO_∞} = 516.26 cm^{-1}. I see a slight increase in the TO_1 peak position (within a ±0.5 cm^{-1} range) as the nanowire width increases. In contrast, the TO_2 Raman peak decreases with increasing nanowire width. Besides, TO_2 was also found to have a higher slope compared to TO_1, which suggest that TO_2 is more sensitive to the changes in the nanowire dimension. For both TO_1 and TO_2, the evolution of the peak positions as the nanowire width increases exhibits a linear but opposite trend. It is also worth mentioning that the TO_1 and TO_2 peaks converge at 516.26 cm^{-1}, which corresponds to the Raman peak of the nanomembrane (i.e., a nanowire with an infinite width). These results agree very well with theoretical predictions shown in Fig. 3.3b (Chapter 3), where the detected TO is doubly degenerate for the nanomembrane. As illustrated in Fig. 3.3, this degeneracy is lifted in the case of the nanowire. From the linear trends, one can extrapolate that at a width of 155 nm the structure is sufficiently broad to possibly preserve the bi-isotropic character at the center, similar to the original nanomembrane. Looking at the difference between TO_1 and TO_2 Raman shift peaks for each nanowire width, we see that $\Delta\omega_{TO\_30} > \Delta\omega_{TO\_50} > \Delta\omega_{TO\_80}$. The increase in the splitting between the TO_1 and TO_2 is due to the narrowing of the width of the nanowires and is a manifestation of the increase in the anisotropy as the nanowire width decreases. To the best of my knowledge, this is the first demonstration of TO mode splitting.

Figures 4.15a – 4.15c display the TO_1 and TO_2 Raman shift images of the 80 nm, 50 nm, and 30 nm nanowires, respectively. These images were obtained through filtering based on the integrated intensity in order to identify the nanowires (see Fig. 4.16 for the intensity profile). This visualization of the fitted Raman shifts validates further the numerical simulations and demonstrates the successful detection of both TO_1 and TO_2 phonons. To examine the behavior of these modes along a nanowire, Figure 4.15d exhibits the profiles of the LO, TO_1 and TO_2 phonon frequencies along the *x*' – axis of the nanowire. Each profile is averaged over 10 different measurements of single nanowires.

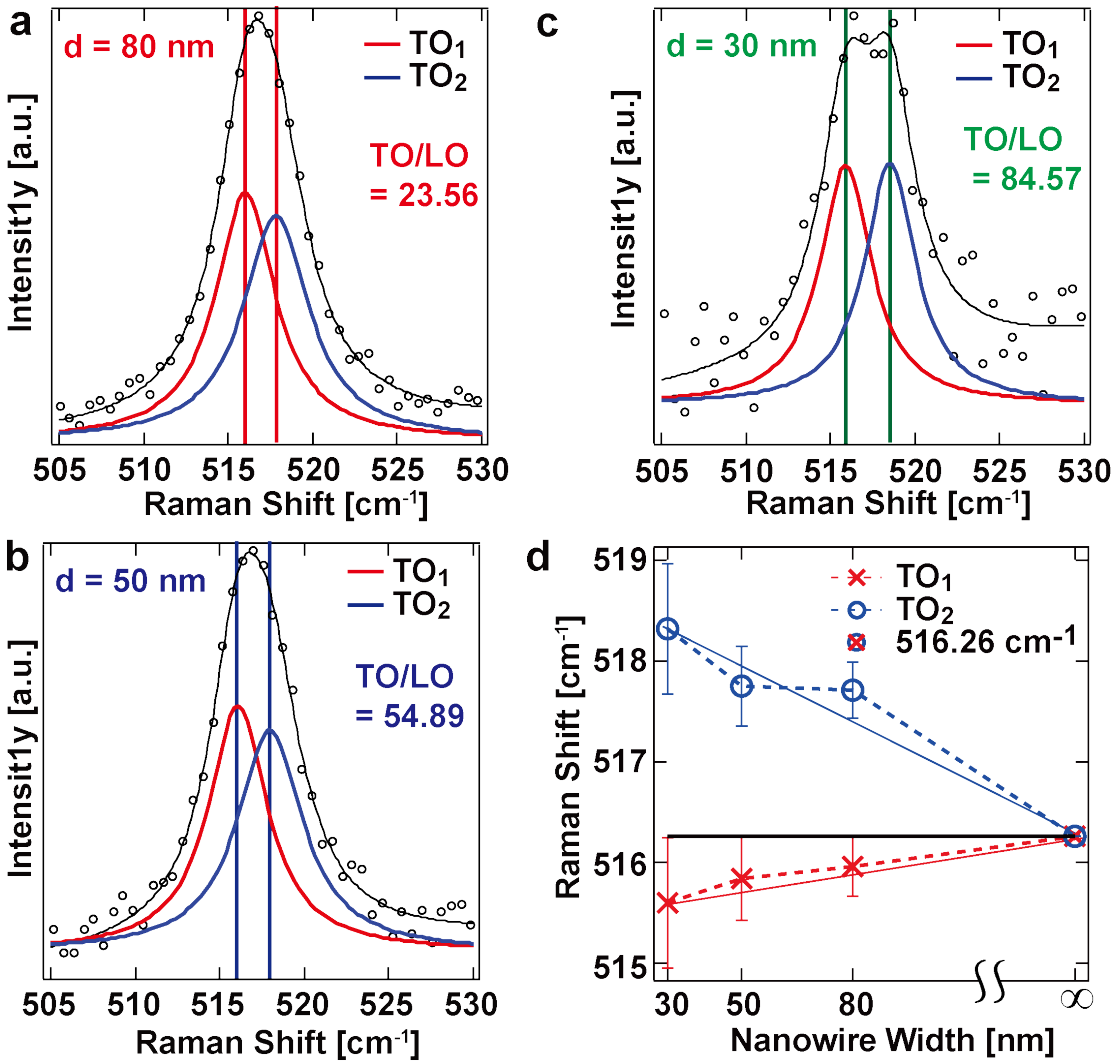

Figure 4.14. Raman spectra from the center of the nanowire with widths of **a**, 80 nm, **b**, 50 nm and **c**, 30 nm. Each Raman spectrum represents averaged data from 10 nanowires. The black hollow circles represent the actual experimental data, while the solid curves represents the fitted data. For fitting, the background signal was subtracted and it was assumed that the intensities of TO_1 and TO_2 are equal due to symmetry. Splitting becomes more evident as the nanowire becomes narrower. To further support the idea that splitting is indeed occurring, the spectral width (Δu) of the experimental data was determined. They are Δu_{80} = 5.38 cm^{-1}, Δu_{50} = 5.46 cm^{-1}, and Δu_{30} = 5.93 cm^{-1}, for 80 nm, 50 nm and 30 nm nanowire widths, respectively. Spectral width broadening occurs as the nanowire width decreases, which coincides with the increase of the splitting between the TO phonon peaks. **d**, The Raman shift of each nanowire is plotted with the degenerated phonon frequency (=516.26 cm^{-1}) of the unpatterned nanomembrane corresponding to infinity width (see Fig. 4.13b).

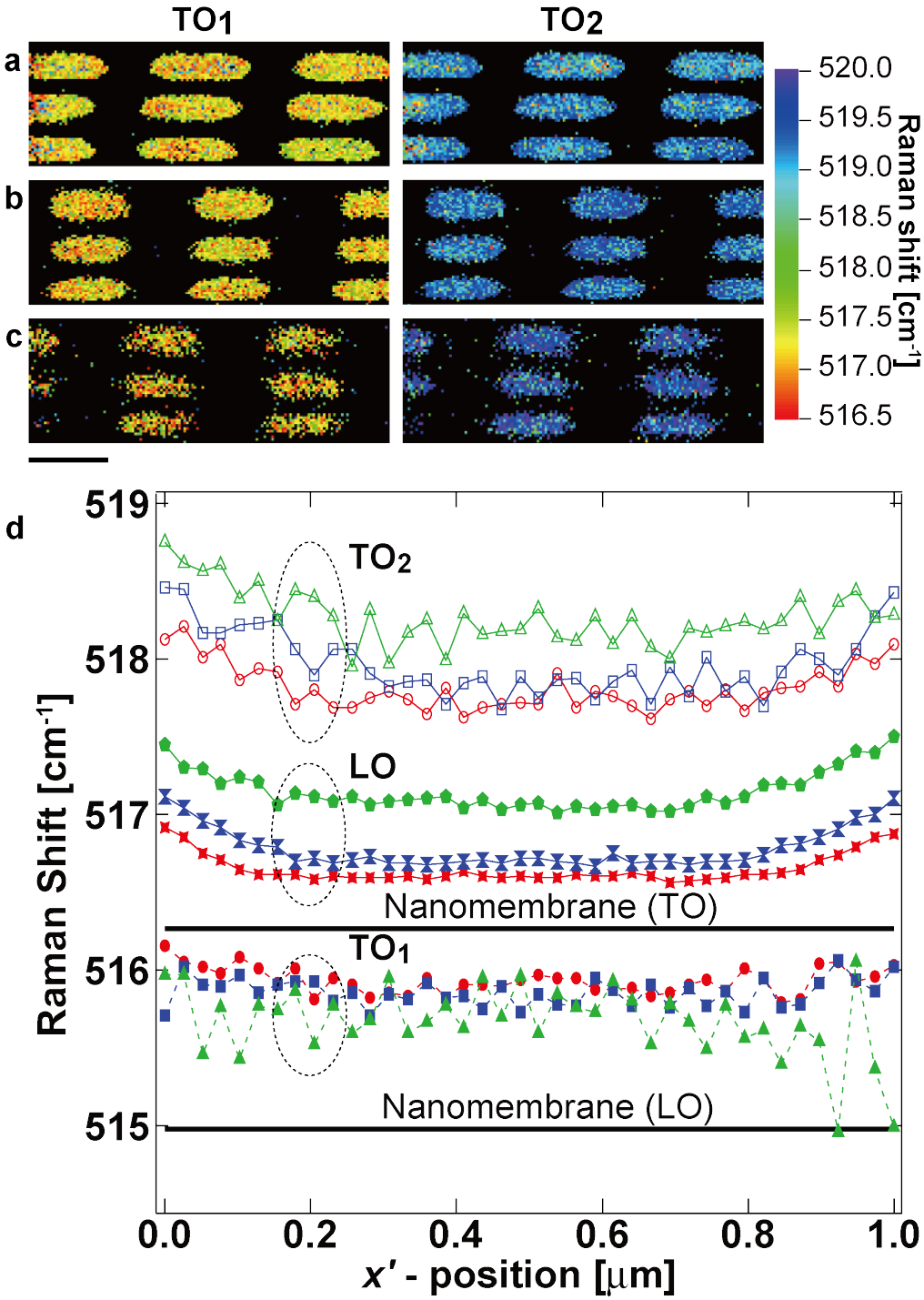

Figure 4.15 The TO_1 and TO_2 Raman shift derived from the double Lorentzian fitting were used to visualize the Raman distribution for **a**, 80 nm, **b**, 50 nm, and **c**, 30 nm width nanowires. The areas without any nanowires present were set to be black to improve the contrast of the image (see also the corresponding Raman intensity image in Fig. 4.16). The scale bar is equivalent to 1 μm. The edges of the nanowires are rounded as compared to the SEM image shown in Fig. 4.1a. This is due to the convolution of the edge of the nanowire and the focus spot, which is probing the nanowire. **d,** The LO, TO_1 and TO_2 Raman shifts along the *x*' – axis of a nanowire is plotted and compared to those of the nanomembrane (LO: 514.97 cm^{-1}, TO: 516.26 cm^{-1}) (see Fig. 4.13b). These data were averaged from 10 nanowires for each set.

The nanomembrane is used as a reference indicating the initial Raman shifts of LO and TO phonon modes prior to patterning, which are 514.97 cm^{-1} and 516.26 cm^{-1}, respectively (Fig. 4.13b). The LO peaks at each position of the nanowires were obtained via single Lorentzian fitting in the LO – active $z'(x',x')\bar{z}'$ polarization setting. It can be seen that for the Raman shifts, TO_2 > LO > TO_1. This behavior reflects the case of anisotropic strain illustrated in Fig. 3.3c. For TO_1, the Raman shift does not vary much as the nanowire width decreases. TO_2, on the other hand, exhibits an increase in the Raman shift as the width decreases. For both cases, the Raman shift around the center of the nanowire (*x*' – position: 200 nm to 800 nm) is relatively constant and increases towards the edges. Based on the obtained TO_1 and TO_2 Raman shifts – $\Delta\omega_{TO1}$ and $\Delta\omega_{TO2}$, respectively – the stress along the length (σ'_{xx}) and along the width (σ'_{yy}) can now be directly evaluated using Eq. (4.12).

Substituting the two TO modes' frequencies from Fig. 4.15 to Eq. (4.12), σ'_{xx} and σ'_{yy} along the nanowires are determined as shown in Fig. 4.16a. Interestingly, this demonstrates that stress in-plane components can be resolved using micro-Raman scattering spectroscopy in backscattering configuration. The general trend is that the stress is higher at the center of the nanowire and decreases as it approaches the edges of the nanowire. Interestingly, and against the prevalent belief that patterning induces strain relaxation in all directions [4.15, 4.24], we observe that the stress along the nanowire axis, σ'_{xx}, is higher than that of the original stress in the nanomembrane before patterning, which is around 1.2 GPa. However, the stress decreases significantly along *y'*-direction, σ'_{yy}. The strong contraction along the smallest dimension is attributed to a higher free surface to volume ratio along *y'*-direction. Fig. 4a also provides strong evidence that this contraction in the *y'*-direction is accompanied by a stretch along the *x'*-direction as expected from the Poisson effect. This lattice expansion translates into an increase in the stress along this direction. This subtle but important observation cannot be achieved based on the sole detection of LO phonons. Therefore, it is of paramount importance to detect both TO_1 and TO_2 to precisely characterize the stress distribution in nanowires and other nanoscale systems with anisotropic stresses. In order to probe the behavior of the stress anisotropy, Fig. 4.16b exhibits the anisotropy ratio σ'_{xx} / σ'_{yy} as a function of the nanowire width. Expectedly, the narrower the width, the higher is the anisotropy ratio. Interestingly, the anisotropy appears to be more significant at the edge of the nanowire where the contraction along the shortest dimension is more pronounced. This heterogeneous distribution of stress in nanowires and its

sensitivity to the nanowire width are very important for the design and fabrication of strained silicon-based devices as the electrical, optical and mechanical properties of the nanowire depend on them.

Using a high NA lens and polarized Raman spectroscopy, we have realized the detection of TO phonons, which is essential for a more comprehensive characterization of stress in nanostructures such as nanowires. Based on numerical simulations, I was able to infer that the LO contribution in the Raman signal is negligible and the detected signal is mainly composed of TO_1 and TO_2. Based on the measured Raman signals from strained silicon nanowires, TO mode splitting is observed for the first time. The splitting between the modes becomes larger as the nanowire width becomes smaller therefore showing higher anisotropic stress relaxation for narrower nanowires. From Raman shift imaging of the TO_1 and TO_2 modes, the stress profiles in single nanowires are directly obtained and it was seen that the stress along the *x'* – axis is higher than the stress of the nanomembranes as a result of the strong lattice contraction along the shortest dimension. Through the detection of the two TO modes, a more detailed stress analysis can be made which will provide a better understanding of the interplay between stress and basic properties and performance of strained semiconductors based nanoscale materials and devices.

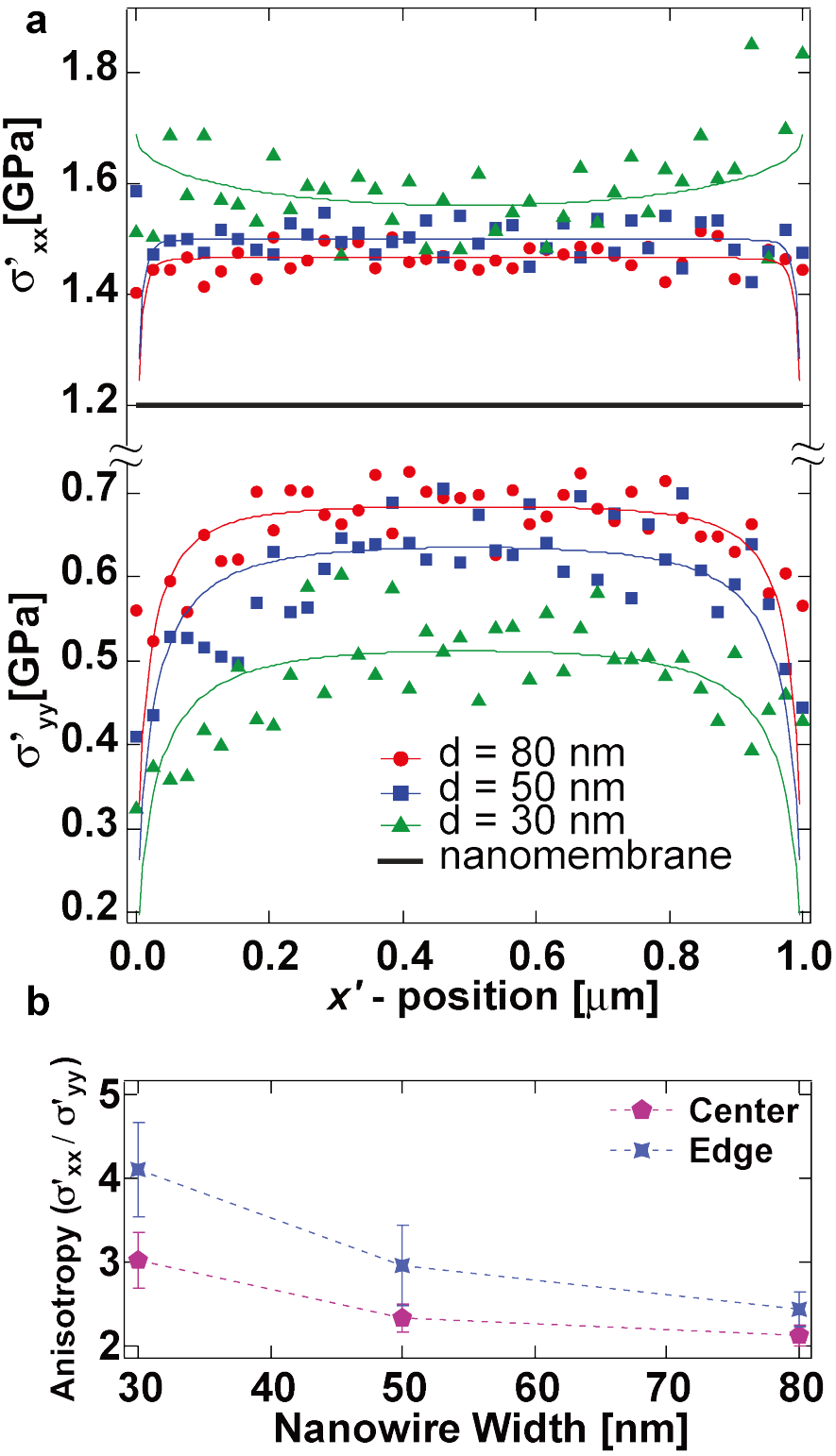

Figure 4.16 a The stress in the *x'* – axis, s'_{xx}, and *y'* – axis, s'_{yy}, along the *x'* – direction of a nanowire for varying width, as compared to the stress in a nanomembrane (1.2 GPa). The circular, square and triangular markers are the computed stresses for the 80 nm, 50 nm and 30 nm nanowire widths, respectively. The solid lines are the corresponding fitting from the computed stresses. **b**, The behavior of the anisotropy ratio as a function of the width both at the center and at the edge of nanowires.

4.5. Comparison of LO and TO Analysis

Using the same experimental setup described in the main text, a 6 μm x 6 μm area was scanned using the $z'(x',x')\bar{z}'$ polarization configuration with a step size of 25 nm. At each step, a Raman spectrum was recorded using an exposure time of 500 ms and incident laser power of 5 mW prior to the microscope. Single Lorentzian fitting was used to extract the LO Raman Shift peaks. Figures 4.17a to 4.17c show the LO intensity images while Figs. 4.17d to 4.17f shows their corresponding LO Raman shift images for the 80 nm, 50 nm and 30 nm width nanowires, respectively. Filtering was used based on the LO intensity images in order to obtain the exact position of the nanowires. It can be seen that as the nanowire width decreases, the Raman shift peak increases.

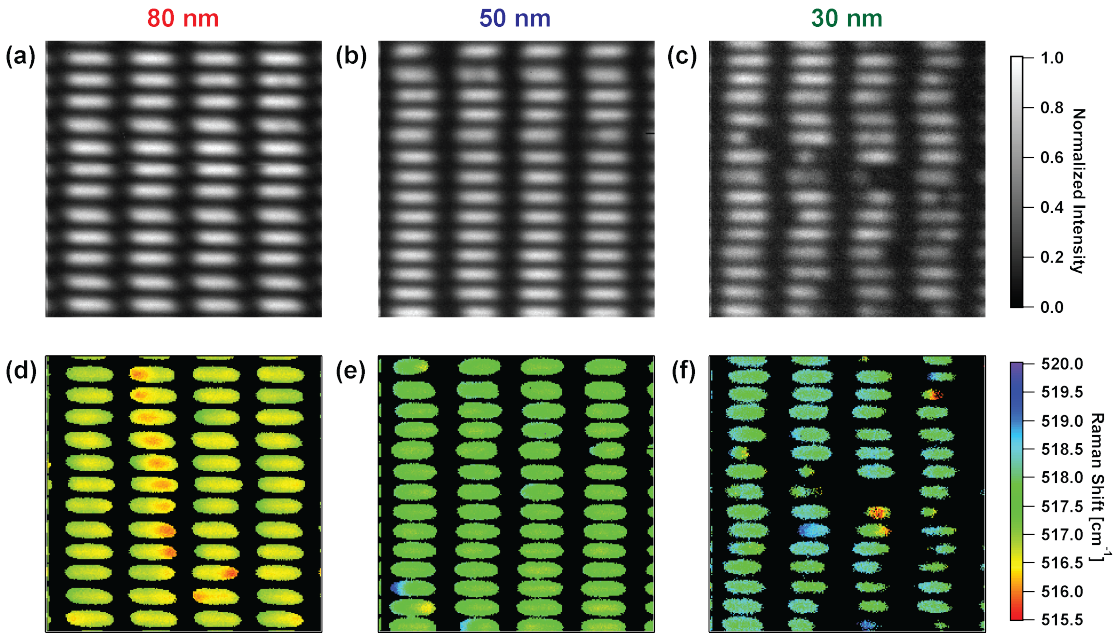

Figure 4.17. Raman intensity and Raman shift images of LO phonon mode detected by $z'(x',x')\bar{z}'$ configuration. The Raman shift clearly increases with decreasing nanowire width.

Figure 4.18 shows the extracted stress based on the experimentally observed LO phonon peaks. It is observed that all the stress values do not exceed the original stress in the unpatterned nanomembrane, which indicates that stress relaxation occurs in both directions. Comparing the stress relaxation in each direction, the y' – axis, σ'_{yy}, is more relaxed than the x' – axis, σ'_{xx}. It is also observed that, similar to the TO data (Fig. 4.16a), the variation of σ'_{xx} is not much as compared to that of σ'_{yy},

wherein the stress relaxation increases as the nanowire width decreases. This is primarily due to the change in dimension in the *y'* – axis wherein the width is varied as compared to the constant length dimension of 1 μm in the *x'* – axis. What is common though in both σ'_{xx} and σ'_{yy} is the behavior of the stress. The stress is maintained at the center of the nanowires and quickly relaxes as it moves to the edges of the nanowires due to the formation of free surfaces. The stress relaxation for a nanomembrane edge, which is assumed as a nanowire with semi-infinite width, was also computed based on experimental measurement from the edge ($x' = 0$) to $x' = 0.5$ mm. The computed σ'_{xx} is plotted at $0 < x' < 0.5$ mm and its mirror image is plotted at $0.5 < x' < 1.0$ mm, resulting to a symmetric plot. Its σ'_{xx} is almost similar to that of the nanomembrane, except that there is some relaxation at the edges. This is expected since one can imagine an infinitely wide nanowire with constant length of 1 μm to be a minute slice of the nanomembrane. Due to its infinite width, the stress at the center of nanowire is nearly preserved, but since it has a finite length, relaxation at the edges occurs. But compared to the relaxation of the 80 nm, 50 nm and 30 nm nanowires, this relaxation is relatively small.

Comparing the stress calculated using LO analysis (Fig. 4.18) and TO analysis (Fig. 4.16a), the main difference is, as mentioned earlier, that the stress does not exceed that of the nanomembrane when LO analysis is used. This is due to the initial assumption made that the nanomembrane is similar to a semi-infinite bulk material. Although this assumption is not wrong, it limits itself to the analysis of stress in the *x'*-direction and to structures experiencing bi-isotropic stress. TO analysis on the other hand does not utilize any assumptions that can limit its applications. Also, the TO analysis method is well suited for nanowire-like structures as shown in this work.

The strain was also computed using the LO method (Fig. 4.19) and it was seen that the derived strain values of strain are comparable to the values used in the semiconductor industry [4.30]. This shows that micro-Raman spectroscopy is indeed a useful technique for strain engineering.

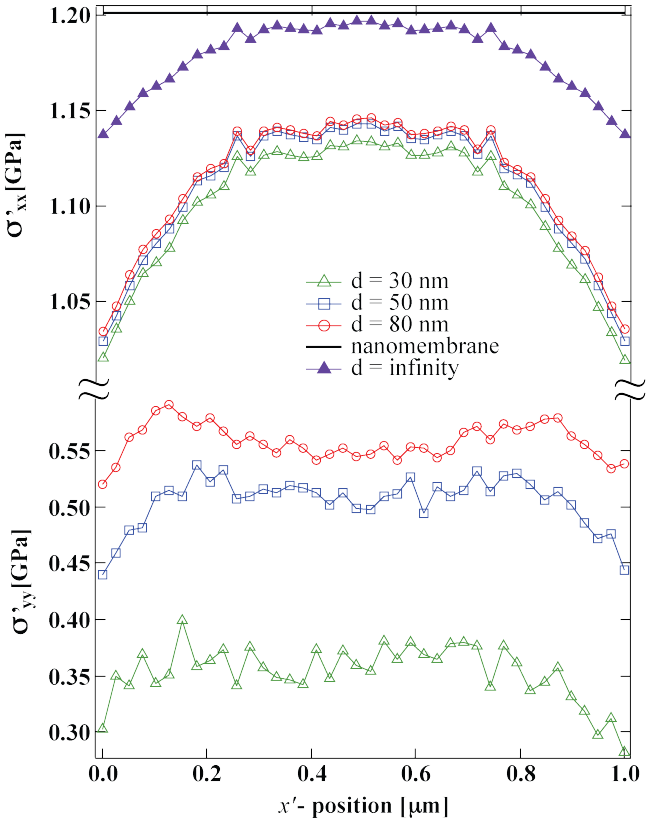

Figure 4.18. Experimentally extracted stress profile along nanowires with different diameters based on LO phonon modes using $z\left(x',x'\right)\bar{z}'$ configuration. All the stress values are smaller than the initial unpatterned nanomembrane stress (1.2 GPa) meaning stress relaxation occurs in both directions.

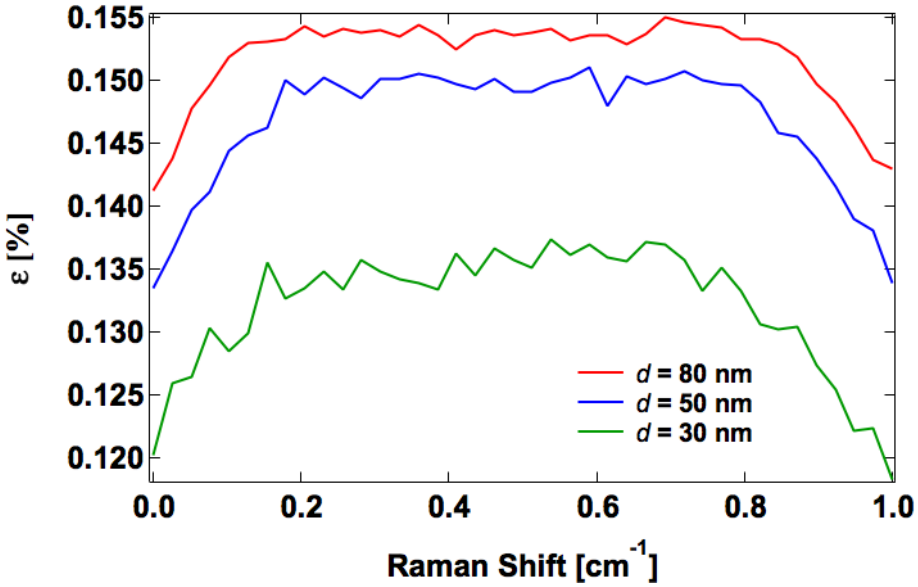

Figure 4.19. Calculated strain experienced by the ε-SiNWs from the LO data obtained.

4.6. REFERENCES

[4.1] A. Tarun, N. Hayazawa, **M.V. Balois**, S. Kawata, M. Reiche, and O. Moutanabbir, Stress redistribution in individual ultrathin strained silicon nanowires: a high-resolution polarized Raman study, *New Journal of Physics*, **15**, 053042, 2013.

[4.2] **M.V. Balois**, N. Hayazawa, A. Tarun, S. Kawata, M. Reiche and O. Moutanabbir. Direct optical mapping of anisotropic stresses in nanowires using transverse optical phonon splitting. *Nano Lett.* **14**, 3793-3798, 2014.

[4.3] J.K. Kuhn, *Proc. Int. Symp. On VLSI Technology, Systems and Applications (25-27 April 2011)*, pp. 1-2, 2011.

[4.4] H. Yan, H.S. Choe, S.W. Nam, Y. Hu, S. Das, J.F. Klemic, J.C. Ellenbogen, and C.M. Lieber, *Nature*, **470**, 240, 2011.

[4.5] T. Palacios, *Nature*, **481**, 152, 2012.

[4.6] M.D. Kelzenberg, S.W. Boettcher, J.A. Petykiewicz, D.B. Turner-Evans, M.C. Putnam, E.L. Warren, J.M. Spurgeon, R.M. Briggs, N.S. Lewis, and H.A. Atwater, *Nature Mater.* **9**, 239, 2010.

[4.7] A. Hochbaum and P. Yang, *Chem. Rev.* **110**, 527, 2010.

[4.8] J.P. Colinge, el. Al, *Nature Nanotechnol.* **9**, 225, 2010.

[4.9] K. Uchida, J. Koga, R. Ohba, T. Numata, and S.I. Takagi, *IEDM Technical Digest,* 633, 2001.

[4.10] O. Gunawan, L. Sekaric, A. Majumdar, M. Rooks, J. Appenzeller, J.W. Sleight, S. Guha, and W. Haensch, *Nano Lett.* **8**, 1566, 2008.

[4.11] P. Hashemi, L. Gomez, and J.L. Hoyt, *IEEE Electron Device Lett.* **30**, 401, 2009.

[4.12] A. Tarun, N. Hayazawa, H. Ishitobi, S. Kawata, M. Reiche and O. Moutanabbir, Mapping the “forbidden” transverse-optical phonon in single strained silicon (100) nanowire, *Nano Lett.* **11**, 4780-4788, 2011.

[4.13] R.A. Minamisawa, M. Süess, R. Spolenak, J. Faist, C. David, J. Gobrecht, KK. Bourdelle, and H. Sigg, *Nature Commun.* **3**, 1096, 2012.

[4.14] O. Moutanabbir, M. Reiche, A. Hähnel, W. Erfurth, U. Gösele, M. Motohashi, A. Tarun, N. Hayazawa and S. Kawata, *Nanotechnology*, **21**, 134013, 2010.

[4.15] F. Ma, T.W. Zhang, K.W. Xu, and P.K. Chu, *Appl. Phys. Lett.* **98**, 191907, 2011.

[4.16] G. Xiong, O. Moutanabbir, X. Huang, S. A. Paknejad, X. Shi, R. Harder, M. Reiche, and I. K. Robinson, *Appl. Phys. Lett*. **99**, 114103, 2011.

[4.17] V. Poborchii, T. Tada, K. Usuda, and T. Kanayama, Appl. Phys. Lett. **99**, 191911 (2011).

[4.18] O. Moutanabbir, M. Reiche, A. Hähnel, M. Oehme, and E. Kasper, Appl. Phys. Lett. **97**, 053105 (2010).

[4.19] **M.V. Balois**, L.L. Dasallas, N. Hayazawa, A. Tarun, S. Kawata and O. Moutanabbir, *in preparation*.

[4.20] O. Moutanabbir, M. Reiche, N. Zakharov, F. Naumann, and M. Petzold, Observation of free surface-induced bending upon nanopatterning of ultrathin strained silicon layer, *Nanotechnology* **22**, 045701, 2011.

[4.21] N. Hayazawa, K. Furusawa, and S. Kawata, Nanometric locking of the tight focus for optical microscopy and tip-enhanced microscopy, *Nanotechnology* **23**, 465203, 2012.

[4.22] I. De Wolf, Micro-Raman spectroscopy to study local mechanical stress in silicon integrated circuits, *Semicond. Sci. Technol.*, **11**, 139-154, 1996.

[4.23] T. Miyatake and G. Pezzotti, *J. Appl. Phys.* **110**, 093511, 2011.

[4.24] S.C. Jain, B. Dietrich, H. Richter, A. Atkinson, and A.H. Harker, *Phys. Rev. B* **52**, 6247, 1995.

[4.25] M. Chandrasekhar, J.B. Renucci, and M. Cardona *Phys. Rev. B* **17**, 1623, 1978.

[4.26] D. Kosemura, M. Tomita, K. Usuda, and A. Ogura, *Jpn. J. Appl. Phys.* **51**, 02BA03, 2012.

[4.27] E. Anastassakis, A. Cantanero, and M. Cardona. *Phys. Rev. B* **41**, 7529-7535, 1990.

[4.28] W.A. Brantley, *J. Appl. Phys.* **44**, 534-535, 1973.

[4.29] D. Kosemura, M. Tomita, K. Usuda, and A. Ogura, Stress measurements in Si and SiGe by liquid-immersion Raman spectroscopy, Book chapter in the book, “Advanced Aspects of Spectroscopy” edited by Muhammad Akhyar Farrukh, InTech, 2012.

[4.30] C.K. Maiti, S. Chattopadhyay, and L.K. Bera, *Strained-Si heterostructure field effect devices*, Taylor and Francis: New York, 2007.

Chapter 5. Carbon Nanotubes: Theory, Properties and Tip-Enhanced Raman Spectroscopy

As silicon is reaching its limit to maintain the continuity of Moore's law, chip manufacturers have invested time and money to develop new computing architectures and processor designs, wherein some are based on new materials [5.1]. There are a number of materials and technologies being innovated by different chip manufacturing companies. Some of these candidates are graphene [5.2], carbon nanotubes [5.3], memristors [5.4], and cognitive computers [5.5, 5.6]. Among these promising candidates, carbon nanotubes (CNTs) are of particular interest because of their intrinsic electronic properties and ultrathin body [5.7] and also because of the recent innovation of a CNT computer developed by engineers in Stanford University [5.8]. To learn more about the characteristics of this nano-sized material whose diameter ranges from around 0.7 – 10 nm in diameter [5.9], it is necessary to use nano-Raman spectroscopy techniques to spatially resolve individual CNTs or bundled CNTs. In this work, a nano-Raman spectroscopy technique called tip-enhanced Raman scattering is utilized to study CNTs.

In this chapter, the theory and basic concepts of TERS are first discussed. Numerical simulations by finite-difference time-domain calculations are presented to show the evolution of the electric field found in the gap between the metal-coated tip and a substrate, which is either glass or a metal-coated glass substrate. Afterwards, the theory and properties of CNTs are discussed. The Raman spectrum of CNTs are explained and results of TERS experiments on CNTs are presented.

5.1. TIP-ENHANCED RAMAN SCATTERING (TERS)

The basic concept of TERS was proposed in 1985 by Wessel – utilizing a single metal nanoparticle that can produce a constant field enhancement to investigate a surface [5.10]. The role of the sharp metal tip was to act as an active site to probe the surface point by point. By integrating this probe with scanning probe microscopy (SPM) techniques, it would be possible to map and analyze the entire surface. This concept became a reality through the development of the TERS system and experimentally demonstrated independently by Hayazawa [5.11], Stöckle [5.12], and Anderson [5.13]. After the initial development of TERS, the spatial resolution was improved being limited only by the diameter of the tip. Such high resolution was demonstrated by Hartschuh, et. al. [5.14] by imaging of single-walled CNTs using

TERS. Aside from achieving high spatial resolution, TERS has proven itself to be a powerful analytical tool because of its high chemical sensitivity. Owing to this sensitivity, TERS has then been used to study various samples and phenomena, reaching even the fields of biology and chemistry. There are a number of applications worth mentioning. The nucleobases of DNA [5.15-5.16] and RNA [5.17] have been identified through their unique vibrational modes. *Staphylococcus epidermidis* bacterium [5.18] has been chemically characterized and the different components of its cell wall [5.19] have been identified that may help further understand the biological processes occurring on the surface of cells. Viruses like the tobacco mosaic virus have also found an application for TERS to provide vibrational spectroscopic information that can eventually lead to fast detection and identification of single virus particles [5.20]. Proteins, such as cytochrome c [5.21], and peptides [5.22] have been analyzed via TERS and TERS gave more chemical information compared to surface-enhanced Raman scattering (SERS) and scanning tunneling microscopy (STM), respectively. Changes in the molecular structure of single-molecule junctions for different conductance states can be studied using a derivative of TERS called "fishing-mode" TERS [5.23]. Photocatalytic reactions can be monitored using time-resolved TERS [5.24], and, quite recently, mapping of catalytic activity using TERS has been achieved [5.25]. This demonstrates the potential and versatility of TERS as an analytical tool.

5.1.1 Electric Field Enhancement at the Tip

An enhanced electric field is generated at the tip of a metallic probe having a nanometric diameter by first irradiating the tip with an electric field (e.g. laser light). This incident electric field causes conductive free electrons to collectively oscillate at the surface of the metal (Fig. 5.1) called surface plasmon polaritons (SPP) [5.26, 5.27]. Both electrons and positive charges are concentrated at the tip and generate a strong external electric field. The photon energy is confined at the local vicinity of the tip, making the tip work as a photon reservoir [5.27]. The local electric field serves as a nanolight source that, when positioned near a sample surface excites and enhances the Raman signal from molecules near the tip apex giving access to spectroscopic information of the sample [5.28].

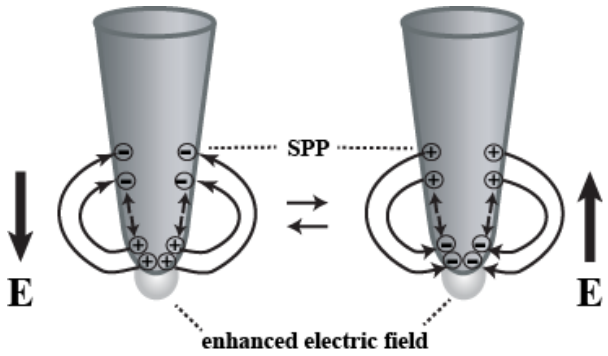

Figure 5.1. Formation of enhanced electric by local SPP at the metallic tip apex.

The strength of the enhanced electric field is dependent on the polarization of the incident beam. For tip enhancement to occur, the incident electric field must be *p*-polarized [5.14, 5.29-5.31]. In particular, if radially polarized light illuminates the tip, a strong electric field shall be generated. This is due to the presence of the strong longitudinal field that couples with the tip [5.31]. Figure 5.2 shows finite-difference time-domain (FDTD) calculations of the electric field generated at the tip apex situated on top of a substrate for different polarizations. The tips simulated are silver (Ag, diameter = 35 nm) and gold (Au, diameter = 60 nm) coated Si tips. These tips were chosen to simulate the tips used in actual TERS experiments. The substrates simulated are glass and Au/Ge coated substrates. The Au has a thickness of 10 nm while the Ge has a thickness of 1 nm. The Au/Ge substrate was used to simulate the actual substrate used in Chapter 6 of this thesis. This substrate is an ultrasmooth substrate that is highly transparent and has no SERS background. For the simulations, two wavelengths were used – 532 nm for Ag simulations and 633 nm for Au simulations. This is to excite the localized surface plasmon resonance on the metal surface. From the simulations, it can be seen that when *s*-polarization is used (Figs. 5.2a – 5.2b and Figs 5.2g – 5.2h) the generated electric field is weak and the central part has minimum enhancement. This can be correlated to the profile of the longitudinal field of linearly polarized light, simulated in Chapter 2 and Chapter 3. When *p*-polarization is used (Figs. 5.2c – 5.2d and Figs. 5.2i – 5.2j), the generated electric field is stronger compared to that of *s*-polarization. But when radial polarization is used (Figs. 5.2e – 5.2f and Figs. 5.2k and 5.2l), the generated electric field is more than 10 times higher compared to *p*-polarization. Therefore, in terms of generating a strong electric field, radial polarization is the best choice. Comparing the use of a glass substrate and a metal-coated substrate, it can be seen that the metal coated substrate helps in generating a stronger electric field. The presence of the metallic thin film enables a tighter confinement around the apex.

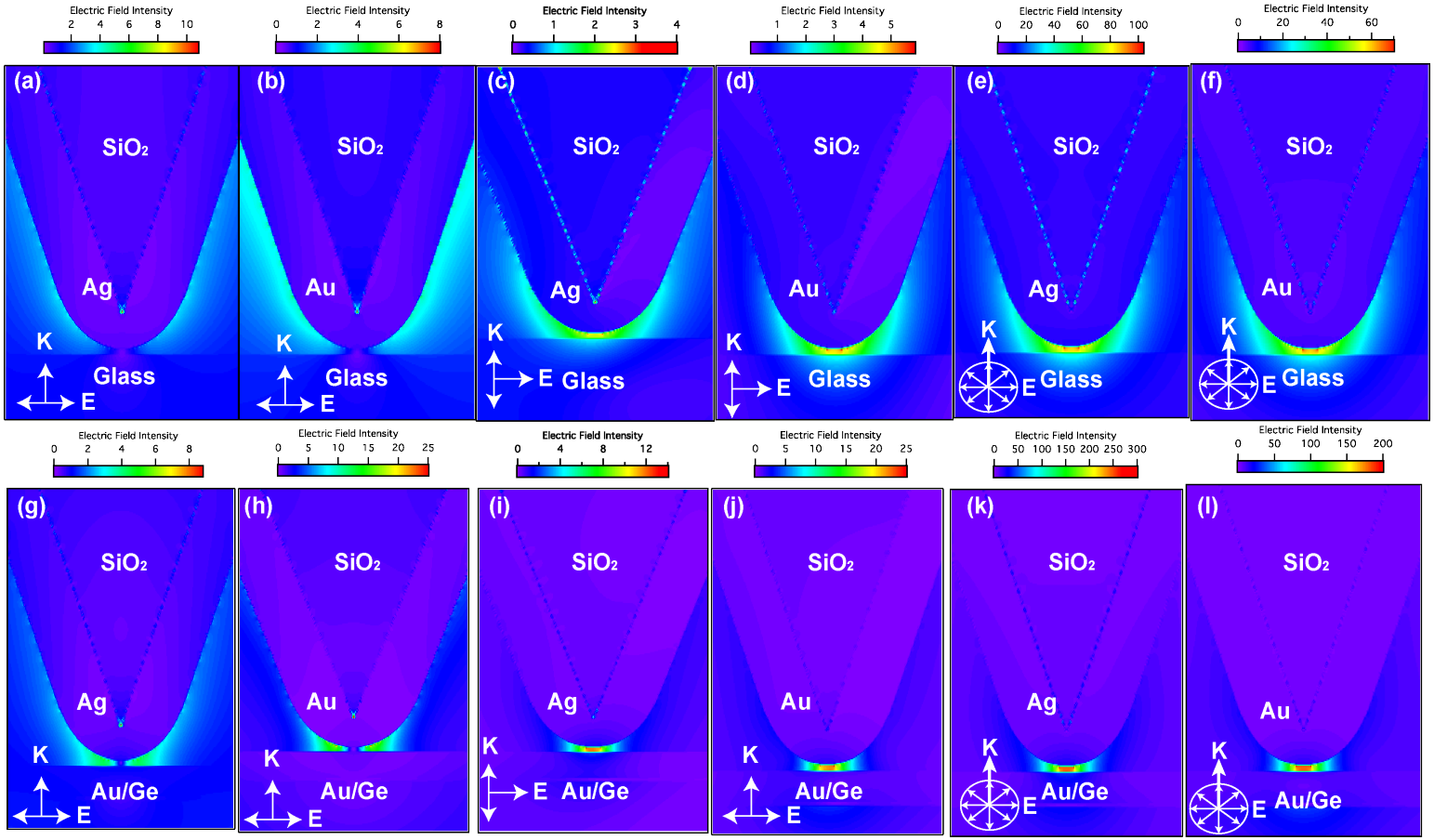

Figure 5.2 Electric field distribution at the tip apex illuminated by either 532 nm for Ag or 633 nm for Au coated tips. Metallic tips on glass substrates using (a) – (b) *s*-polarized, (c) – (d) *p*-polarized and (e) – (f) radially polarized illumination. Metallic tips on Au/Ge substrate using (g) – (h) *s*-polarized, (i) – (j) *p*-polarized and (k) – (l) radially polarized illumination.

5.1.2. System Geometry

A typical TERS setup consists of laser light that enters an inverted microscope and is focused by an objective lens (NA = 1.49) as shown in Fig. 5.3a. The metal-coated tip is then moved to the focus point to create a localized and enhanced electric field. The use of a high numerical aperture (NA) objective lens helps generate a strong longitudinal field along the tip axis that is p-polarized [5.32]. The spatial resolution is determined by the diameter of the tip, which dictates the size of the enhanced field. This kind of configuration is called “transmission mode” [5.11, 5.12] and is widely used for transparent samples. Another configuration is called “reflection mode” [5.13] and is used for opaque samples (Fig. 5.3b). Although reflection mode is advantageous for opaque samples, it has a relatively higher background signal compared to transmission mode TERS. This is because of the low NA objective lens with long working distance that is used to illuminate the tip.

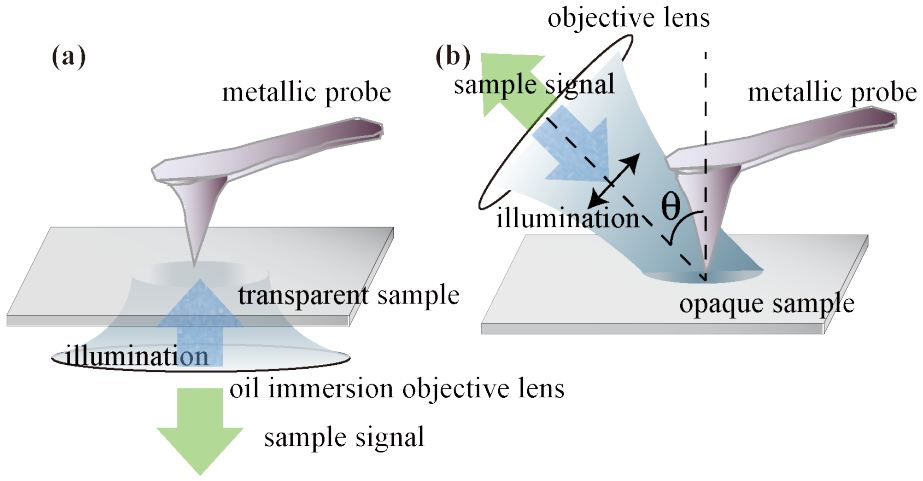

Figure 5.3 (a) Transmission mode and (b) reflection mode TERS.

5.1.3. Fabrication of Metallic Probes used for TERS

The tips used for the TERS experiments are contact mode atomic force microscopy (AFM) silicon cantilever tips (Fig. 5.4a), CSG10 (NT-MDT, force constant = 0.11 N/m). They are baked for 10 hours to form a SiO_2 layer (thickness > 200 nm) (Fig.5.4b). The diameter of the tips are around 30 nm after baking. The tips are baked in order to: (i) blue shift the resonant wavelength, (ii) the resulting SiO_2 is transparent and not absorptive compared to silicon and (iii) moderately dulls the tip end to aid in the formation of the appropriate metal grain size during evaporation [5.33]. Usually the noble

metals, Au or Ag, are deposited onto the oxidized tips via thermal evaproation. The thickness to attain high enhancement varies for each metal. For Ag, typically 60 nm is evaporated while for Au, 90 nm is evaporated (Fig. 5.4c).

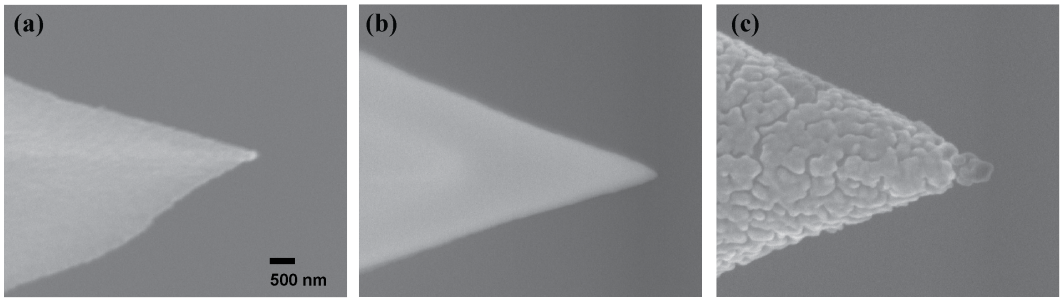

Figure 5.4. SEM images of the cantilever tips in each step of the metallization process: (a) unoxidized Si tip, (b) oxidized tip, and (c) Au-coated (metallized) tip.

5.1.4 Taking Care of TERS tip

The life of a TERS experiment relies heavily on how the tip is prepared and how it is handled during experiment. When the tip is prepared, it must be in a clean environment. A contaminated tip cannot be used for TERS experiments because the Raman generated by the contamination (called contamination peaks) would overpower the Raman from the sample. During TERS experiments, the power of the illuminating beam must be strong enough to detect Raman signal from the sample, but weak enough so as not to damage the tip. When too strong a power is used on the tip, the tip and the metal will melt as shown in Fig. 5.5a. Care must also be made when approaching the tip onto the sample surface. If the tip crashes onto the sample surface, the tip end may be broken (Fig. 5.5b). Any appreciable damage to the tip end caused by melting or breakage will render the tip useless for the rest of the experiment. In principle, tips must be used from within 24 hours to a few days after fabrication to ensure that the tip is still TERS active. When storing tips, it is advisable to put them in vacuum-sealed containers and store these containers in a vacuum cabinet. This will minimize the amount of contamination that can contaminate the tip.

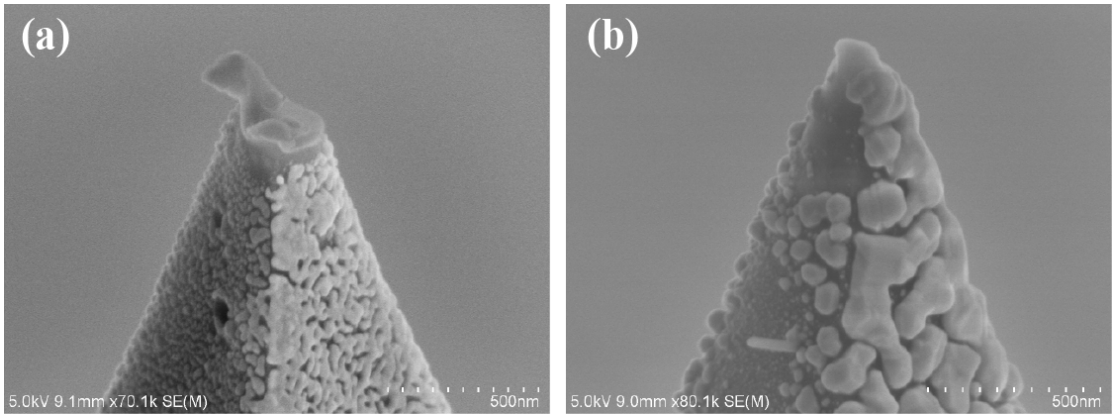

Figure 5.5 SEM images of damaged Au-coated SiO_2 tips: (a) melted tip due to high illumination power (~ 3 mW) and (b) broken tip.

5.2. CARBON NANOTUBES (CNTs)

Single walled CNTs are defined as graphene sheets rolled up into a seamless cylinder, which is usually one atom thick [5.9, 5.34]. A nanotube is identified by its chiral vector $\mathbf{C_h}$ [5.34],

$$\mathbf{C}_h = n\mathbf{a}_1 + m\mathbf{a}_2 \equiv (n,m), \tag{5.1}$$

where the paired indices (n,m) indicate the number of unit vectors $n\mathbf{a}_1$ and $m\mathbf{a}_2$ in the hexagonal honeycomb lattice contained in the vector $\mathbf{C}_h$. $\mathbf{C}_h$ makes a chiral angle θ with the zigzag or $\mathbf{a_1}$ direction (Fig. 5.6).

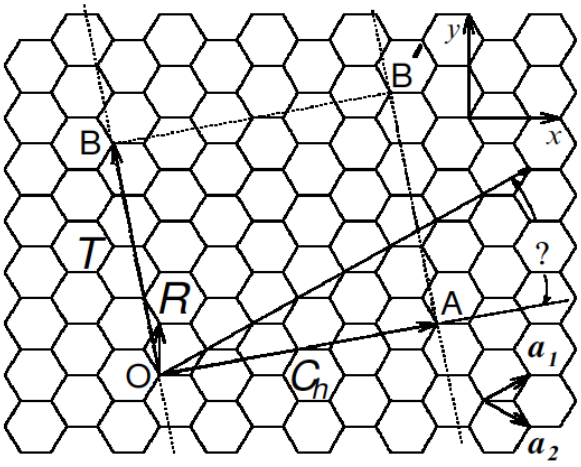

Figure 5.6 Unrolled honeycomb lattice of a CNT. When lattice sites *O* and *A*, and lattice sites *B* and *B'* are connected, a nanotube is constructed. $\overline{OA}$ represents the chiral vector, $\mathbf{C}_h$. $\overline{OB}$ represents the translational vector **T**. The rectangle $OAB'B$ is the unti cell of the CNT. In this illustration, the CNT is $(n,m)=(4,2)$. [Taken from Ref. 5.9]

The diameter of the CNT, d_t, is defined as [5.9]

$$d_t = L/\pi, \quad L = |C_h| = \sqrt{C_h \cdot C_h} = a\sqrt{n^2 + m^2 + nm}, \tag{5.2}$$

where L is the circumferential length of the CNT.

The chiral angle θ is computed by taking the inner product of $\mathbf{C_h}$ and $\mathbf{a_1}$,

$$\cos\theta = \frac{C_h \cdot \mathbf{a}_1}{|C_h||\mathbf{a}_1|} = \frac{2n+m}{2\sqrt{n^2+m^2+nm}}. \tag{5.3}$$

From this equation, the zigzag nanotube has a chiral angle of $\theta = 0°$, while the armchair nanotube has $\theta = 30°$. There are two kinds of CNTs depending on their electronic properties. These are metallic or semiconducting CNTs based on their on d_t and θ.

5.2.1 The Raman Spectrum of CNTs

The Raman spectrum of CNTs can give valuable information about the electronic and structural state of the CNT. Figure 5.7 shows a typical micro-Raman spectrum of a semiconducting CNT. There are 4 distinct Raman peaks and these are the *G band, 2D band, D band* and *radial breathing mode (RBM)*.

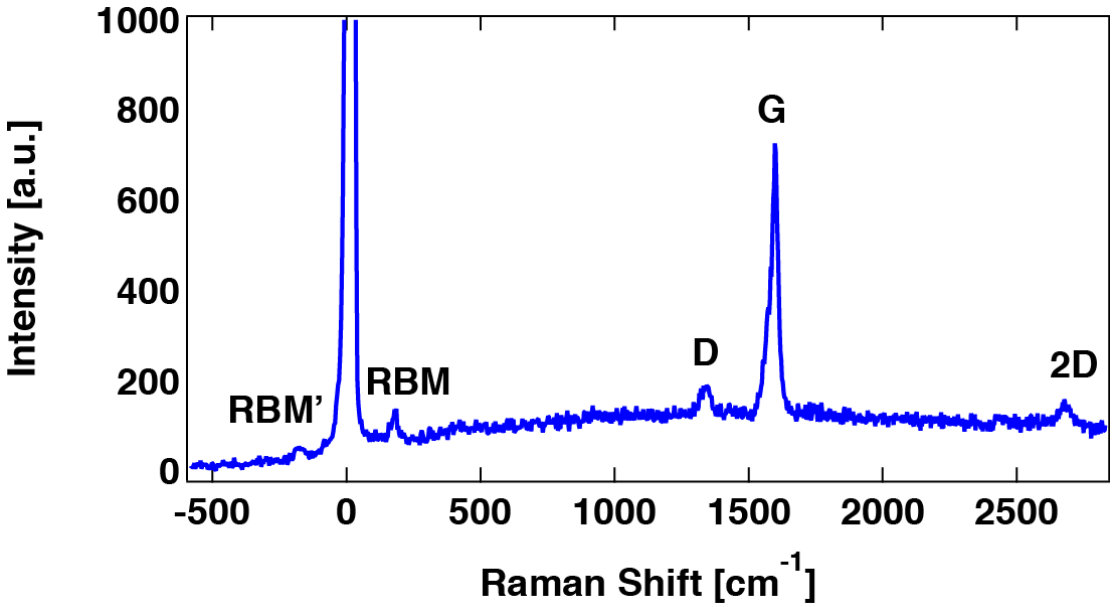

Figure 5.7 Typical micro-Raman spectrum from a semiconducting CNT, the G-band, D-band, 2D-band and RBM (RBM' is for anti-Stokes) are identified.

The G band is related to the longitudinal optical (LO) phonon mode whose peak occurs around 1580 cm^{-1} [5.35]. This is related to the tangential vibration mode of the C atoms and is useful for 1) diameter characterization, 2) distinguishing between metallic and semiconducting CNTs through their differences in Raman lineshapes, 3) probing charge

transfer from doping of CNT and 4) studying Raman selection rule for various scattering processes and geometries [5.36]. The 2D band arises from a two-photon, intervalley, second-order Raman scattering process. Its peak position is dependent on the excitation laser used. In the case of Fig. 5.7, a 532 nm laser was used. The intensity of the 2D band determines the quality of the CNT. If the CNT is of high-quality, the 2D band's intensity is comparable to that of the G band. The D band is induced by disorders in the carbon. It indicates atomic defects within the layer of carbon. The relative intensity of D to G bands can determine the CNT purity [5.35]. While changes in the D and 2D bands can be used to probe structural modifications of the nanotube sidewalls due to defects or attachment of chemical species onto the walls [5.36]. The RBM is useful to determine the d_t via its RBM frequency $\left(\omega_{RBM}\right)$. It is also possible to extract the temperature of the CNT with knowledge of the Stokes and anti-Stokes intensities [5.28]. Further discussion on this aspect of the RBM can be found in Chapter 6 of this thesis. From the d_t, the chirality of the CNT being studied can also be determined. The intensity of the RBM can also give information regarding the electronic structure of the CNT. Along with the Kataura plot [5.37], the RBM can identify whether the CNT is metallic or semiconducting. Any structural changes in the CNT can have implications on the electronic properties of the CNT. Through the use of Raman spectroscopy, it is possible detect such changes.

5.2.2 CNT and TERS

From Section 5.2.1, using micro-Raman spectroscopy, it is possible to detect the Raman spectra from CNTs. But since micro-Raman spectroscopy is diffraction limited, it is not possible to detect whether the signal is coming from a single CNT or a group of CNTs spaced close together. Since CNTs are nanometer in size, they cannot be seen via a conventional microscope. In order to resolve this nano-sized material, TERS is necessary. Figure 5.8a shows the far-field image obtained via micro-Raman spectroscopy. The bright area indicates the presence of CNTs (semiconducting in this case), but no clear structure of the CNTs can be seen. Figure 5.8b and 5.8c show the TERS and topography image of the same area shown in Fig. 5.8a, respectively. Both TERs and topography images were taken simultaneously during experiment. The white horizontal lines on the right side of the topography image (Fig. 5.8c) are artifacts from the measurement. From the TERS image, the semiconducting CNT can be clearly seen. Even the bending of the tube is resolved and shows good correspondence with the topography image. Figure 5.9 shows both the far-field (gray line) and the TERS (red line) spectra taken at the same point A with the same power (150 μW) and exposure time (10

s). It can be clearly seen that TERS can enhance the signal from the sample. The contrast to determine the enhancement is defined as [5.38]

$$Contrast = \frac{I_{near}}{I_{far}} = \left(\frac{I_{total}}{I_{far}} - 1 \right) \tag{5.4}$$

where I_{near} is the intensity of the near-field signal, I_{far} is the intensity of the far-field signal and I_{total} is the measured intensity during experiment, which is the sum of the near-field and far-field Raman intensities. The enhancement factor (EF) is defined as [5.27]

$$EF = Contrast \times \left(\frac{d_{focus}^2}{d_{tip}^2} \right), \tag{5.5}$$

where d_{focus} and d_{tip} are the diameters of the focus and tip, respectively. For the G-band, the contrast is around 12. The diameter of the focus using a 532 nm laser and a NA = 1.49 objective lens is 435.6 nm. The diameter of the tip is 35 nm. Therefore, the EF for the G-band is 1760. With this high enhancement and high spatial resolution, TERS can provide information on the local changes in structure of CNTs which can be useful in analyzing the CNTs' electronic properties.

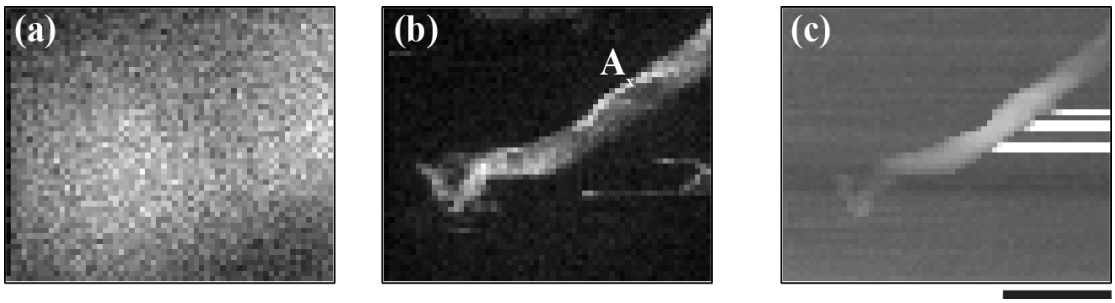

Figure 5.8 (a) Far-field, (b) near-field (TERS) and (c) topography image of bundled semiconducting CNTs. Scale bar indicates 200 nm.

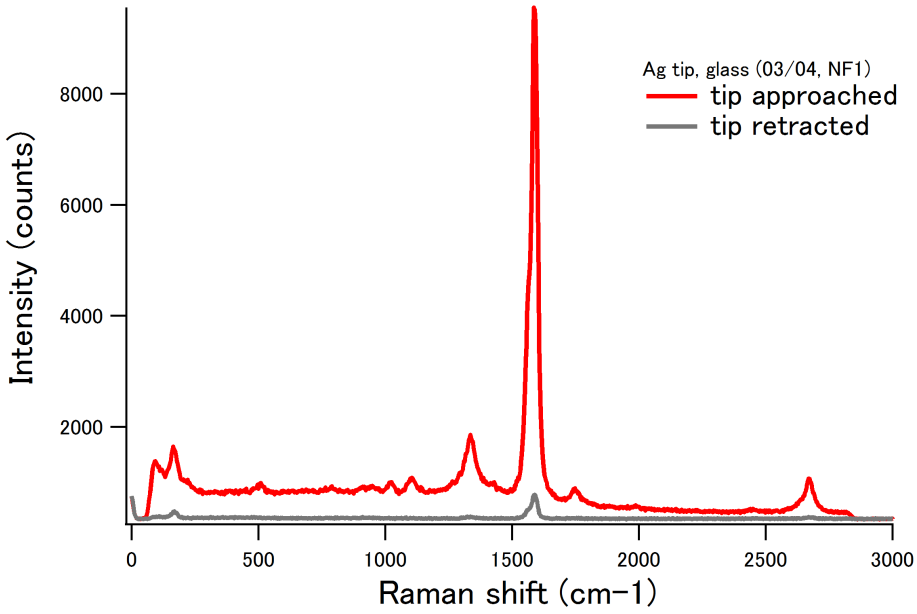

Figure 5.9 Far field (gray line) and TERS (red line) spectra taken at point A of Fig. 5.8b. Far-field is when the tip is retracted from the sample. TERS is when the tip has approached the sample.

5.3. REFERENCES

[5.1] J. Pavlus, The Search for a New Machine, *Scientific American*, **312**, 58 – 63, 2015.

[5.2] X. Gan, R.J. Shiue, Y. Gao, I. Meric, T.F. Heinz, K. Shepard, J. Hone, S. Assefa, and D. Englund, Chip-integrated ultrafast graphene photodetector with high responsivity, *Nature Photonics*, **7**, 883 – 887, 2013.

[5.3] S.J. Tams. A.R.M. Verschueren, and C. Dekker, Room-temperature transistor based on a single carbon nanotube, *Nature* **393**, 49 – 52, 1998.

[5.4] D.B. Strukov, G.S. Snider, D.R. Stewart, and R.S. Williams, The missing memristor found, *Nature* **453**, 80-83, 2008.

[5.5] D.S. Modha, R. Ananthanarayanan, S.K. Esser, A. Ndrirango, A.J. Sherbondy, and R. Singh, Cognitive Computing, *Communications of the ACM*, **54**, 62 – 71, 2011.

[5.6] Esser, S.K.; Andreopoulos, A.; Appuswamy, R.; Datta, P.; Barch, D.; Amir, A.; Arthur, J.; Cassidy, A.; Flickner, M.; Merolla, P.; Chandra, S.; Basilico, N.; Carpin, S.; Zimmerman, T.; Zee, F.; Alvarez-Icaza, R.; Kusnitz, J.A.; Wong, T.M.; Risk, W.P.; Mcquinn, E.; Nayak, T.K.; Singh, R.; Modha, D.S., "Cognitive computing systems: Algorithms and applications for networks of neurosynaptic cores," *Neural Networks (IJCNN), The 2013 International Joint Conference on* , vol., no., pp.1,10, 4-9 Aug. 2013

[5.7] J. Appenzeller, Carbon nanotubes for high-performance electronics – progress and report, *Proceedings of the IEEE*, **96**, 201-211, 2008.

[5.8] M.X. Shulaker, G. Hills, N. Patil, H. Wei, H.Y. Chen, H.S.P. Wong, and S. Mitra, Carbon nanotube computer, *Nature* **501**, 526-530, 2013.

[5.9] R. Saito, G. Dresselhaus, and M.S. Dresselhaus, *Physical Properties of Carbon Nanotubes*, Imperial College Press: London, 1998.

[5.10] J. Wessel. Surface-enhanced optical microscopy, *J. Opt. Soc. Am.* **2**, 1538, 1985.

[5.11] N. Hayazawa, Y. Inouye, Z. Sekkat, S. Kawata. Metallized tip amplification of near-field Raman scattering. *Opt. Commun.* **183**, 333, 2000.

[5.12] R. M. Stöckle, Y. D. Suh, V. Deckert, R. Zenobi. Nanoscale chemical analysis by tip-enhanced Raman spectroscopy*. Chem. Phys. Lett.* **318**, 131, 2000.

[5.13] M. S. Anderson. Locally enhanced Raman spectroscopy with an atomic force microscope*. Appl. Phys. Lett.* **76**, 3130, 2000.

[5.14] A. Hartschuh, E. J. Sánchez, X. S. Xie, L. Novotny. High-Resolution Near-Field Raman Microscopy of Single-Walled Carbon Nanotubes*. Phys. Rev. Lett.* **90**, 095503, 2003.

[5.15] Rasmussen A, Deckert V (2006) Surface- and tip-enhanced Raman scattering of DNA components. J Raman Spectrosc 37:311-317

[5.16] Najjar S, Talaga D, Schué L, Coffinier Y, Szunerits S, Boukherroub R, Servant L, Rodriguez V, Bonhommeau (2014) Tip-enhanced Raman spectroscopy of combed double-stranded DNA bundles. J Phys Chem C 118:1174-1181

[5.17] Bailo E, Deckert V (2008) Tip-enhanced Raman spectroscopy of single RNA strands: towards a novel direct-sequencing method. Angew Chem Int Ed 47:1658-1661

[5.18] Neugebauer U, Schmid U, Baumann K, Ziebuhr W, Kozitskaya S, Deckert V, Schmitt M, Popp J (2007) Towards a detailed understanding of bacterial metabolism – spectroscopic characterization of *Staphylococcus Epidermidis*. ChemPhysChem 8:124-137

[5.19] Budich C, Neugebauer U, Popp J, Deckert V (2008) Cell wall investigations utilizing tip-enhanced Raman scatter. Journal of Microscopy 229:533-539

[5.20] Cialla D, Deckert-Gaudig T, Budich C, Laue M, Möller R, Naumann D, Deckert V, Popp J (2009) Raman to the limit: tip-enhanced Raman spectroscopic investigations of a single tobacco mosaic virus. J Raman Spectrosc 40:240-243

[5.21] Yeo BS, Mädler S, Schmid T, Zhang W, Zenobi R (2008) Tip-enhanced Raman spectroscopy can see more: the case of cytochrome c. J Phys Chem C 112:4867-4873

[5.22] Paulite M, Blum C, Schmid T, Opilik L, Eyer K, Walker GC, Zenobi R (2013) Full spectroscopic tip-enhanced Raman imaging of single nanotapes formed from ß-amyloid (1-40) peptide fragments. ACS Nano 7:911-920

[5.23] Liu Z, Ding SY, Chen ZB, Wang X, Tian JH, Anema JR, Zhou XS, Wu DY, Mao BW, Xu X, Ren B, Tian ZQ (2011) Revealing the molecular structure of single-molecule junctions in different conductance states by fishing-mode tip-enhanced Raman spectroscopy. Nat Commun 2:305

[5.24] Van Schrojenstein Lantman EM, Deckert-Gaudig T, Mank AJG, Deckert V, Weckhuysen BM (2012) Catalytic processes monitored at the nanoscale with tip-enhanced Raman spectroscopy. Nat Nanotechnol 7:583-586

[5.25] Kumar N, Stephanidis B, Zenobi R, Wain AJ, Roy D(2015) Nanoscale mapping of catalytic activity using tip-enhanced Raman spectroscopy. Nanoscale 7:7133-7137

[5.26] N. Hayazawa, A. Tarun, A. Taguchi, and S. Kawata, Development of tip-enhanced near-field optical spectroscopy and microscopy, *Jpn. J. Appl. Phys.* **48**, 08JA02, 2009.

[5.27] Kawata S, Shalaev VM (2007) Tip enhancement. Elsevier, The Netherlands

[5.28] **M.V. Balois**, N. Hayazawa, F.C. Catalan, S. Kawata, T. Yano, and T. Hayashi, Tip-enhanced THz Raman spectroscopy for local temperature determination at the nanoscale, *Analytical and Bioanalytical Chemistry*, *accepted*, Vol. xx, pp. xx-xx, 2015.

[5.29] E.J. Sánchez, L. Novotny, and X.S. Xie, *Phys Rev Lett* **82**, 4014, 1999.

[5.30] H. Furukawa and S. Kawata, *Opt. Commun.* **148**, 221, 1998.

[5.31] N. Hayazawa, Y. Saito and S. Kawata, *Appl. Phys. Lett.* **85**, 6239, 2004.

[5.32] N. Hayazawa, Y. Inouye, and S. Kawata, *J. Microsc.* **194**, 472, 1999.

[5.33] N. Hayazawa, T. Yano and S. Kawata, *J. Raman Spectrosc.* **2012**, *43,* 1177-1182

[5.34] M.S. Dresselhaus and P.C. Ecklund, Phonons in carbon nanotubes, *Advances in Physics* **49**, 705-814, 2000.

[5.35] M.S. Dresselhaus, A. Jorio and R. Saito, Characterizing graphene, graphite and carbon nanotubes by Raman spectroscopy, *Annu. Rev. Condens. Matter Phys.* **1**, 89-108, 2010.

[5.36] M.S. Dresselhaus, G. Dresselhaus, R. Saito, and A. Jorio, Raman spectroscopy of carbon nanotubes, *Physics Reports* **409**, 47-99, 2005.

[5.37] Kataura H, Kumazawa Y, Maniwa Y, Umezu I, Suzuki S, Ohtsuka Y, Achiba Y (1999) Optical properties of single-wall carbon nanotubes. Synthetic Metals 103:2555-2558

[5.38] A. Tarun, N. Hayazawa, and S. Kawata, Tip-enhanced Raman spectroscopy for nanoscale strain characterization, *Anal Bioanal Chem* **394**, 1775-1785, 2009.

Chapter 6. Carbon Nanotubes: Tip-Enhanced TeraHertz Raman Scattering, a nano-Raman spectroscopy study [6.1]

One consequence of the enhancement brought about by TERS is the increase in temperature, particularly in the vicinity of the tip apex [6.2-6.3]. The joule heating generated at the tip apex is caused by the absorption of light – represented by a value proportional to the imaginary part of the dielectric function of the tip. Temperature plays a key role when studying physicochemical properties of materials, especially thermally sensitive ones. Variations in the temperature of the material and its environment may alter its molecular structure, chemical composition or induce thermal damage. Therefore, it is important to know the temperature on the sample for a certain amount of laser power used during TERS experiments. There are only several works reported so far on the temperature issue in TERS. Downes et al. analytically predicted the increase of the local temperature at the tip apex based on the finite element method [6.2], in which a large tip-enhancement effect induces a temperature rise over 3 orders of magnitude higher than without the tip. Zenobi's group reported an experimental verification of local heating at the tip apex by observing the morphological change of metallic nano-grains even at low temperatures (less than 100 °C) and the subsequent loss of the tip-enhancement [6.3]. This observation, however, was an indirect method and the exact temperature was not known. Sokolov's group reported on the direct determination of the local temperature based on the Boltzmann distribution of the anti-Stokes/Stokes Raman intensity ratio [6.4]. The extracted temperature had a minimum value of 100 °C, but they used a relatively thick film as a sample (thickness ~ 50 nm) making the extracted temperature an average over the sample volume. The detection sensitivity was also quite low due to the high energy of their observed Raman shift (1000 cm^{-1} ~ 1600 cm^{-1}) resulting in extremely weak anti-Stokes signal. In addition, the difference of detection efficiency for both anti-Stokes and Stokes frequencies was not considered in their calculation. In 2010, Kawata's group reported another approach to determine the temperature at a metal-coated silicon cantilever tip [6.5]. The temperature was determined by the shift of the Raman peak originating from the silicon cantilever [6.6]. Although this method is useful, it is limited to silicon cantilever based tips and is not applicable to recently reported oxidized tips for higher tip-enhancement [6.7]. Moreover, the detectable temperature was rather high (greater than 100 ºC) because the spectral shift at low temperatures (less than 100 ºC) was too weak to be detected. In this thesis chapter, all the issues of the previous works are circumvented. The proposed approach is based on the direct determination of the temperature extracted by the Boltzmann distribution of

simultaneously observed anti-Stokes and Stokes Raman scattering in the terahertz (THz) Raman frequency range (less than 200 cm^{-1}). Let us focus on the low frequency feature of the radial breathing mode (RBM) of single walled carbon nanotubes (CNTs) by which the difference of detection efficiency, tip-enhancement, and resonant Raman efficiency at anti-Stokes and Stokes frequencies could be negligible due to the small wavelength gap between the two frequencies. Furthermore, the intensity of anti-Stokes Raman scattering is sufficiently high to be even comparable to Stokes Raman scattering because of the low energy of THz Raman modes. Here the local temperature of the sample located underneath the tip apex at a low temperature range (less than 100 ºC) is determined and showed that the temperature was controlled by the incident laser power with high sensitivity.

6.1 TEMPERATURE DETERMINATION BASED ON THE BOTLZMANN DISTRIBUTION

The temperature at the sample is related to the ratio of the intensities of the anti-Stokes (I_{AS}) and Stokes (I_S) Raman signal according to the Boltzmann distribution defined as [6.8]

$$\frac{I_{AS}}{I_S} = \left(\frac{\omega_0 + \omega_R}{\omega_0 - \omega_R} \right)^4 \exp\left[\frac{-hc\omega_R}{k_B T} \right] \tag{6.1}$$

where ω_0 is the laser excitation frequency, ω_R is the Raman scattering frequency, h is Planck's constant, c is the speed of light, k_B is Boltzmann's constant and T is the temperature at the sample. The factor raised to the fourth power corrects the frequency dependent scattering cross section. However, Eq. 6.1 is only valid if I_{AS} and I_S are measured directly. For experiments involving photon counting using a charge couple device (CCD) as a detector, a conversion factor is needed. This conversion factor is the Planck relationship that relates the photon count rates to the intensities and is defined as [6.9]

$$E = h\omega \tag{6.2}$$

$$\left.\begin{aligned} I_{AS} \propto P_{AS} = \dot{n}_{AS} h\left(\omega_0 + \omega_R\right), \\ I_S \propto P_S = \dot{n}_S h\left(\omega_0 + \omega_R\right). \end{aligned}\right\} \tag{6.3}$$

In Eq. 6.3, P_{AS} and P_S are the power propagated by the scattered light (both anti-Stokes and Stokes), while $\dot{n}_{AS}$ and $\dot{n}_S$ are the photon count rates. Substituting Eq. 6.3 into Eq. 6.1 results into the more applicable form

$$\frac{\dot{n}_{AS}}{\dot{n}_S} = \left(\frac{\omega_0 + \omega_R}{\omega_0 - \omega_R} \right)^3 \exp\left[\frac{-hc\omega_R}{k_B T} \right]. \quad (6.4)$$

Henceforth, the intensity being described is the intensity based on the photon count rates, $\dot{n}_{AS}$ and $\dot{n}_S$.

Figure 6.1 shows the behavior of the $\dot{n}_{AS}$ and $\dot{n}_S$ ratio ($\dot{n}_{AS}/\dot{n}_S$) as a function of temperature up to around 100 ˚C (373.15 K) based on Eq. 6.4 for different ω_R. As the ω_R increases, the change of $\dot{n}_{AS}/\dot{n}_S$ as a function of temperature also increases; however, $\dot{n}_{AS}$ becomes extremely weak, compared to $\dot{n}_S$, which makes it nearly impossible to experimentally detect the signal at the given low temperature range. In this sense, the D- and the G-bands of CNTs are not good choices for temperature calculation. Similarly, as the Raman shift gets lower than 100 cm^{-1}, $\dot{n}_{AS}$ becomes higher and even comparable to $\dot{n}_S$; however, the change of $\dot{n}_{AS}/\dot{n}_S$ becomes very small and is experimentally difficult to detect. In contrast, the Raman shift between 150 ~ 200 cm^{-1}, which is the typical frequency range of RBM, shows comparable intensity while exhibiting more than 30% of the change in $\dot{n}_{AS}/\dot{n}_S$ within the plotted temperature. This signal level and the change in $\dot{n}_{AS}/\dot{n}_S$ make RBM detection sensitive enough to experimentally obtain the local temperature in the probed volume. Previous works have shown the temperature dependence of the RBM frequency [6.10-6.11], but these measurements have only been done in the far-field. It is advantageous to use the RBM to determine *in situ* the temperature of the CNTs during TERS measurements because both the anti-Stokes and the Stokes can be measured simultaneously with high spectral resolution. Strictly speaking, the experimentally detected $\dot{n}_{AS}$ and $\dot{n}_S$ are affected by the detection efficiency of the detector such as diffraction efficiency of the grating and camera sensitivity. However, owing to the THz feature of RBM, the wavelength gap between anti-Stokes and Stokes is 10 nm – for the case of 532 nm excitation with 180 cm^{-1} Raman shift – which makes the difference of the detection efficiency negligible. Moreover, the possible frequency dependent tip-enhancement effect and resonant Raman condition could be negligible.

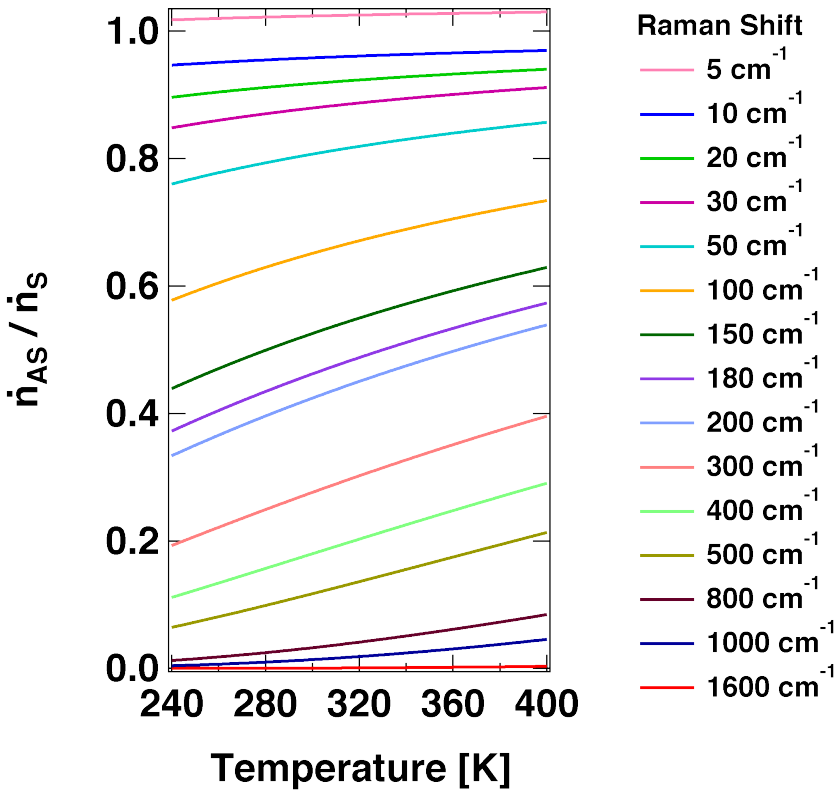

Figure 6.1. Calculated between anti-Stokes/Stokes intensity ratio as a function of temperature at various Raman shifts. ω_0 is set to 15802.8 cm^{-1} corresponding to 632.8 nm.

6.2 SAMPLE PREPARATION

6.2.1. Au/Ge substrate

In TERS, a metallic gap induces much higher electric field enhancement [28-30], which would result to higher temperature rise. Among the metallic substrates, on which molecules are adsorbed, gold is one of the preferable choices for its high chemical stability. In order to apply transmission configuration for the illumination described below, an ultrathin and smooth Au (gold) / Ge (germanium) coated cover glass is used as a substrate [6.12], which is similar to the concept of a single crystal Au nanoplate [6.13]. First, the Ge layer with a thickness of 1 nm was deposited onto a cover glass in a thermal evaporator (K-Science Inc. KS-807RK) at an evaporation rate of 0.1 Å/s. Afterwards, the Au layer with a thickness of 10 nm was evaporated at a rate of 0.2 Å/s. The Ge layer acted as a wetting layer that improved the adhesion of Au onto the glass surface, resulting to a smooth Au film.

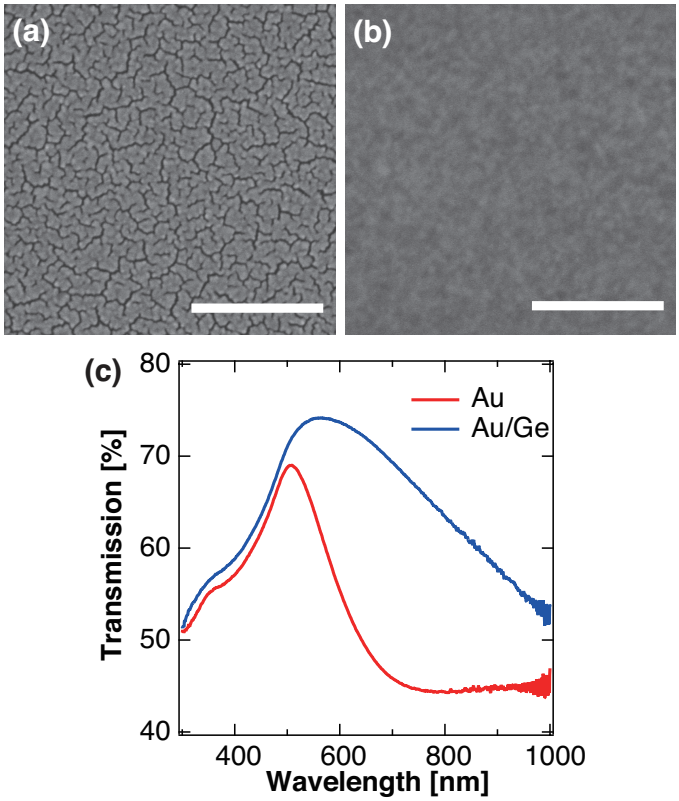

Figure 6.2. Scanning electron microscope images (SEM) of (**a)** Au and **(b)** Au/Ge substrates. The scale bars indicate 200 nm length. **(c)** Transmission spectra of Au (red line) and Au/Ge (blue line) substrates.

Figures 6.2(a) and 6.2(b) show the scanning electron microscope images of the surfaces of an Au thin film (thickness = 10 nm) and an Au/Ge thin film (Au thickness = 10 nm / Ge thickness = 1 nm), respectively. Without the Ge layer (Fig. 6.2(a)), gaps across the Au film were observed. These gaps are potential sources of hot spots that can generate SERS signals and affect the TERS measurements. On the other hand, when the Ge layer was introduced, a smooth and almost gap-free Au film was fabricated (Fig. 6.2(b)). This Au/Ge substrate had no SERS effect, which was also confirmed by dark field image of the substrate [6.12]. The change in surface morphology also reflected in the films' optical properties. Fig. 6.2(c) shows the transmission spectra of the Au (red line) and the Au/Ge (blue line) thin films. It should be noted that the transmission of Ge film was separately measured and was subtracted from the Au/Ge spectrum. While the Au/Ge thin film reflected the dielectric function of gold and exhibited a broad transmission from visible to near infrared wavelengths, the Au thin film showed a dip in the transmission from 550 ~ 800 nm caused by absorption due to local surface plasmon polariton excitation. Thus, the high transmission of the SERS free Au/Ge film makes it a good substrate for TERS in the transmission configuration and can be used for biological [6.13] and self-assembled monolayers (SAMs) samples.

6.2.2. Carbon nanotube on substrate preparation

The samples used in this study are CNTs made via arc-discharge method (Meijo Nano Carbon Co., Ltd), in which the diameter distribution is centered at 1.4 nm. Based on the Kataura plot [6.14], semiconducting CNTs (s-CNTs) are in resonance with 532 nm excitation and metallic CNTs (m-CNTs) are in resonance with 632.8 nm excitation. Accordingly, two separate samples were made: one containing only s-CNTs and the other containing only m-CNTs. Both samples were prepared in a similar manner. An amount of 0.1 mg of CNTs was dissolved in 10 mL of dichloroethane through sonication. From this solution, 50 µL was taken and spin coated on an Au/Ge thin film on cover glass following a sequence of 500 rpm for 10 s and 3000 rpm for 30 s. The sample was placed in a vacuum (0.13 KPa) drying oven and baked at 150 ˚C for 1.5 hours to minimize carbon-based contamination. Baking also ensured the evaporation of residuals, which is essential to affix the CNTs onto the substrate surface and prevent dragging during contact-mode AFM scanning.

6.3. EXPERIMENTAL SETUP FOR TIP-ENHANCED TERAHERTZ RAMAN SCATTERING

I have recently developed a TERS system to detect THz-Raman modes that have been difficult to observe by conventional edge filters due to the filters' cutoff frequency. In this work, tip-enhanced THz-Raman spectroscopy (TE-THzRS) is explored as a means to determine the local temperature of a sample directly underneath the tip apex. The temperature of CNTs is determined through the detection of the RBM using low laser power on the sample. The experimental setup of the TE-THzRS system (Figure 6.3(a)) consists of an inverted optical microscope (NIKON, TE2000) equipped with an XY-PZT stage for stage scanning the sample and an atomic force microscope (AFM) head for controlling the a metal coated cantilever tip. The beam from either a continuous-wave He-Ne (λ = 632.8 nm) or solid-state (λ = 532 nm) laser is introduced into the polarization convertor (ARCoptix) to generate radially polarized laser light for efficient tip-enhancement effect [6.14] and focused onto the sample via a high numerical aperture (NA) oil-immersion objective lens (NA = 1.49, ×100). The scattered light from the tip and the sample is collected using the same objective lens. To detect both the Stokes and the anti-Stokes Raman signals from the sample, the scattered light passes through two notch filters (OptiGrate, BragGrate^{TM} Notch Filter) that block the strong Rayleigh component. The beam is then guided to a spectrometer and detected by either a cooled charge coupled device (CCD) or by a single-photon counting avalanche photodiode

(APD). Spectroscopic measurements are detected via CCD. Optical imaging measurements are detected via APD while simultaneously obtaining topographic images. Thermally oxidized silicon cantilever tips (NTMDT, CSG10) [6.8] are coated with either Au (thickness = 90 nm) or Ag (silver) (thickness = 60 nm) by evaporation. The consequent diameters of the tips after evaporation are typically 60 nm for Au (Fig. 6.3(b)) and 35 nm for Ag (Fig. 6.3(c)). These Au- and Ag-coated tips are experimentally confirmed to show sufficiently high reproducibility and tip-enhancement for 632.8 nm and 532 nm excitation, respectively.

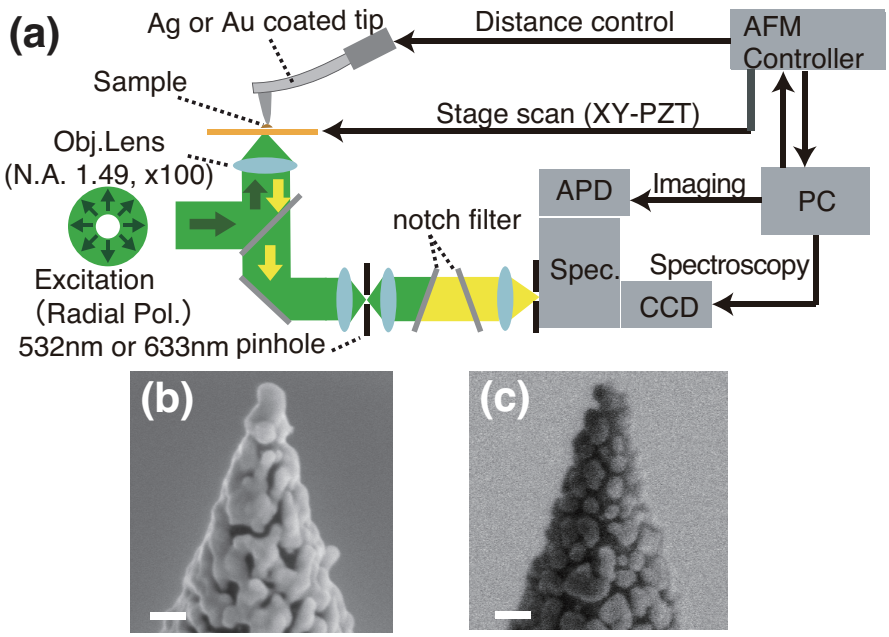

Figure 6.3. (a) Schematic of TE-THzRS experimental setup. Scanning electron microscope images of **(b)** Au- and **(c)** Ag-coated SiO_2 cantilever tips. Scale bars indicate 100 nm length.

6.4. LOCAL TEMPERATURE DETECTION OF CARBON NANOTUBE SAMPLES BY TE-THzRS

Figures 6.4(a) and 6.4(b) show the experimental results using 632.8 nm illumination on an m-CNT sample. The laser power illuminating the sample is 50 μW. Fig. 6.4(a) is the tip-enhanced Raman scattering (TERS) image resulting from the detection of the G-band ($\omega_{G\text{-}632.8}$ = 1580.05 cm^{-1}). Fig. 6.4(b) is the corresponding topography image obtained simultaneously with the TERS image. Based on the topographical height, the observed m-CNT sample is a bundle consisting of several individual m-CNTs. In both images, the intersection of two m-CNTs is clearly visualized. It should be pointed out that the width of the m-CNT in topography image is wider than the one in TERS image. This is attributed to the large grain diameter of the Au-tip apex (see Fig. 6.3(b)). Fig. 6.4(c) and 6.4(d) show, respectively, the TERS image of G-band ($\omega_{G\text{-}532}$ = 1591.21 cm^{-1}) and the corresponding topography image of s-CNTs excited by 532 nm with the power of 36.7 μW. With this power, the photon density (and the resultant electric field) at the tight focus is comparable with the 632.8 nm measurement. The area with two parallel s-CNTs is clearly resolved beyond the diffraction limit in both images. Due to the relatively smaller diameter of the Ag-tip (see Fig. 6.3(c)) and the high tip-enhancement factor, the width of the TERS image is analogous to the topography image. It should be noted that regardless of the different widths of the topography images in Fig. 6.4(b) and 6.4(d), the height is still comparable, meaning that both the observed m-CNTs and s-CNTs are bundles comprising several CNTs. For TE-THzRS spectroscopy of RBM, an area with strong TERS intensity in Fig. 6.4(a) was chosen. Fig. 6.4(e) shows the TE-THzRS spectrum (red line) and the far-field spectrum (blue line) from Point A in Fig. 6.4(a). The corresponding topography height is around 6 nm. To obtain the anti-Stokes and Stokes intensities, single Lorentzian fitting is made for the TE-THzRS spectrum from which the far-field spectrum is subtracted. The calculated intensities are taken to be the background free integrated intensities of the fitted Lorentzian curves. The RBM frequency, $\omega_{RBM\text{-}632.8}$, is 187.70 cm^{-1}. The calculated $\dot{n}_{AS}/\dot{n}_{S}$ is 0.44. Using Eq. (1), wherein the Raman scattering frequency of interest is the RBM frequency, the sample temperature is calculated to be 33.7 ˚C. The rise in temperature with respect to room temperature (17.0 ˚C) is $\Delta T_{632.8}$ = 16.7 ˚C. Fig. 6.4(f) shows the TE-THzRS spectrum (red line) and the far-field spectrum (blue line) from Point B in Fig. 6.4(c). The corresponding topography height is also around 6 nm. The RBM frequency, $\omega_{RBM\text{-}532}$ is 173.83 cm^{-1}. The $\dot{n}_{AS}/\dot{n}_{S}$ ratio is 0.48 so that the derived sample temperature is 51.6 ˚C. The rise in temperature from the room temperature is ΔT_{532} = 34.6 ˚C.

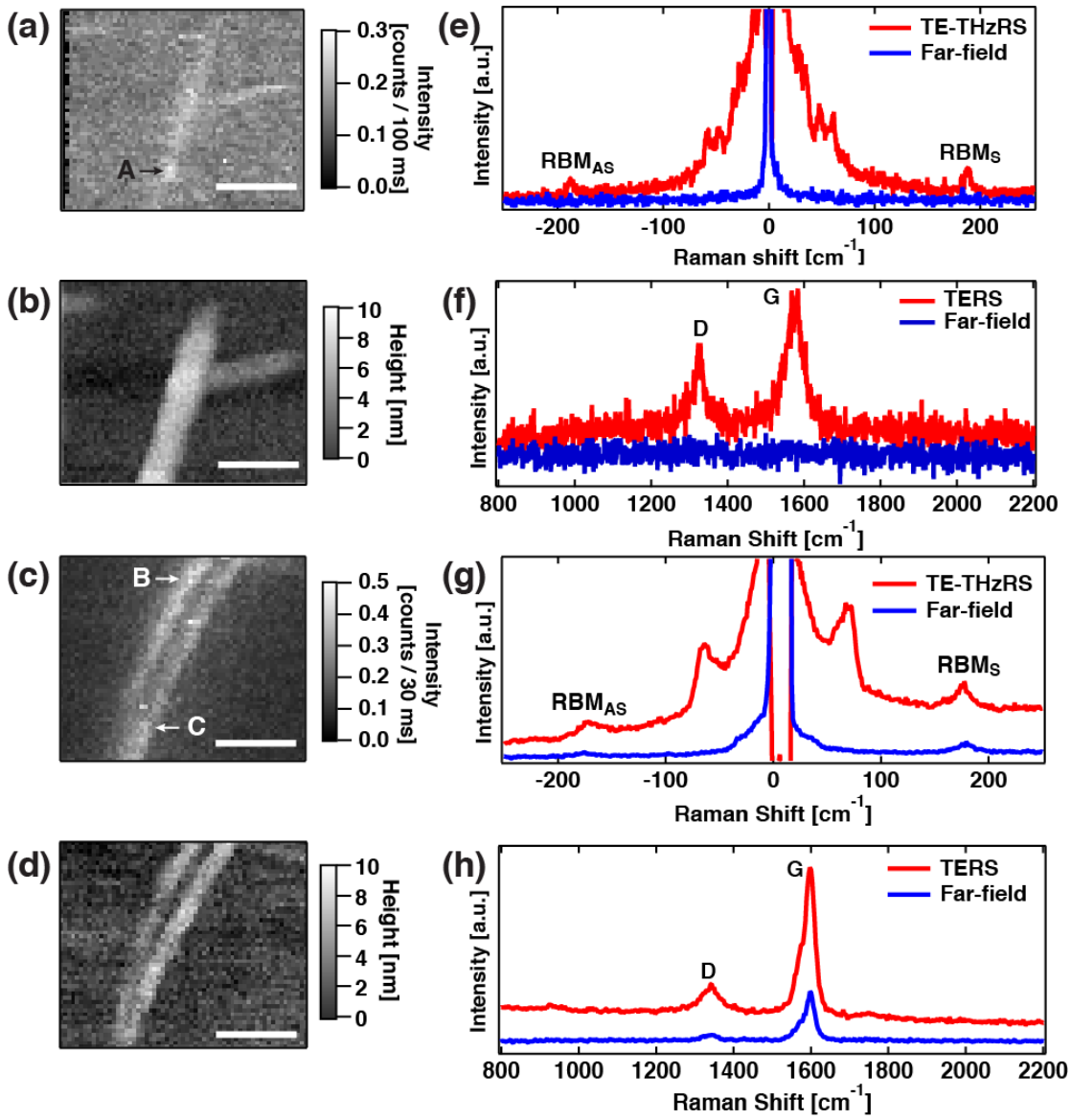

Figure 6.4. **(a)** TERS image of G-band from m-CNT using 632.8 nm illumination. **(b)** Corresponding topography image of m-CNT simultaneously acquired with the TERS image. **(c)** TERS image of s-CNT using 532 nm illumination. **(d)** Corresponding topography image of s-CNT also simultaneously acquired with the TERS image. The scale bars indicate 200 nm length. **(e)** TE-THzRS Raman spectrum of RBM and **(f)** TERS G and D band Raman spectra from Point A of m-CNT (Fig. 6.4(a)). **(g)** TE-THzRS Raman spectrum of RBM and **(h)** TERS G and D band Raman spectra from point B of s-CNT (Fig. 6.4(c)). Near-field data (TE-THzRS and TERS) are both indicated by red lines. Raman spectrum without the tip is also plotted in each figure (blue lines).

Although the expected number of CNTs in both cases is similar based on the topography, the observed TERS and TE-THzRS intensity in 632.8 nm are quite weaker than the one in 532 nm. There could be two reasons for this. First, the m-CNT has a weaker Rayleigh scattering efficiency (632.8 nm illumination) as compared to the s-CNT (532 nm illumination). Second, from the Kataura plot [6.14], the m-CNTs of 1.4 nm in diameter are not in perfect resonance with the 632.8 nm laser whereas the s-CNTs of 1.4 nm in diameter exhibit a good overlap with the 532 nm laser, leading to strong resonance Raman efficiency. This can be confirmed by the observed RBM frequencies. The diameter of the CNT was determined using the relation [6.16]:

$$\omega_{\mathrm{RBM}} = A / d_t + B \qquad (2)$$

where d_t is the diameter of the CNT, A = 234 cm^{-1} and B = 10 cm^{-1}. In the case of $\omega_{RBM\text{-}532}$ = 173.83 cm^{-1} d_t is 1.43 nm while $\omega_{RBM\text{-}632.8}$ = 187.7 cm^{-1} gives d_t = 1.32 nm, which is quite smaller than the expected diameter centered at 1.4 nm. Based on the Kataura plot, at around 1.4 nm diameter using 632.8 nm excitation, m-CNTs with smaller diameter (~ 1.3 nm) are in resonance condition. Hence, only a few m-CNTs having such small diameters contribute to the observed TERS and TE-THzRS intensity of 632.8 nm resulting in a weaker signal compared to the 532 nm on s-CNTs.

Regardless of the different resonant Raman condition for 632.8 nm and 532 nm, the experimentally obtained temperature rise of the m-CNT sample ($\Delta T_{632.8}$) was considerably lower than the temperature rise of the s-CNT sample (ΔT_{532}) under the comparable photon density at the tight focus. In order to further investigate the difference in the temperature rise in both excitation wavelengths, analytical calculations have been conducted and are shown in the next section.

6.5 Comparison and Discussion with Analytical Results

I carried out electromagnetic and thermal simulations of TERS using a finite element software package (COMSOL Multiphysics) to predict the temperature rise at different particle sizes and gap distances. In order to mimic and simplify the real experimental system, I assumed the metallic tip as a metallic particle (Au for 632.8 nm and Ag for 532 nm) with a diameter comparable to the size observed in the SEM images (Figs. 6.2(b) – 6.2(c)) and modeled the Au substrate as an Au particle for both excitation wavelengths in the analytical calculation. The initial phase of the analysis consisted of high frequency electromagnetic calculations to obtain the Joule heat generation caused by the absorption of light, which is proportional to the imaginary part of the dielectric function

and the enhanced electromagnetic field between the particles. The Joule heat generated was then used in the steady state thermal simulation to predict the temperature at the gap using conduction and radiation heat transfer. The initial temperature in the calculation was set to 20 ºC (293.15 K). The complex permittivity of Au and Ag were obtained from literature [6.17]. Also the thermal constants such as conductivity and heat capacity, and density of the materials used in the simulation were taken from the COMSOL library.

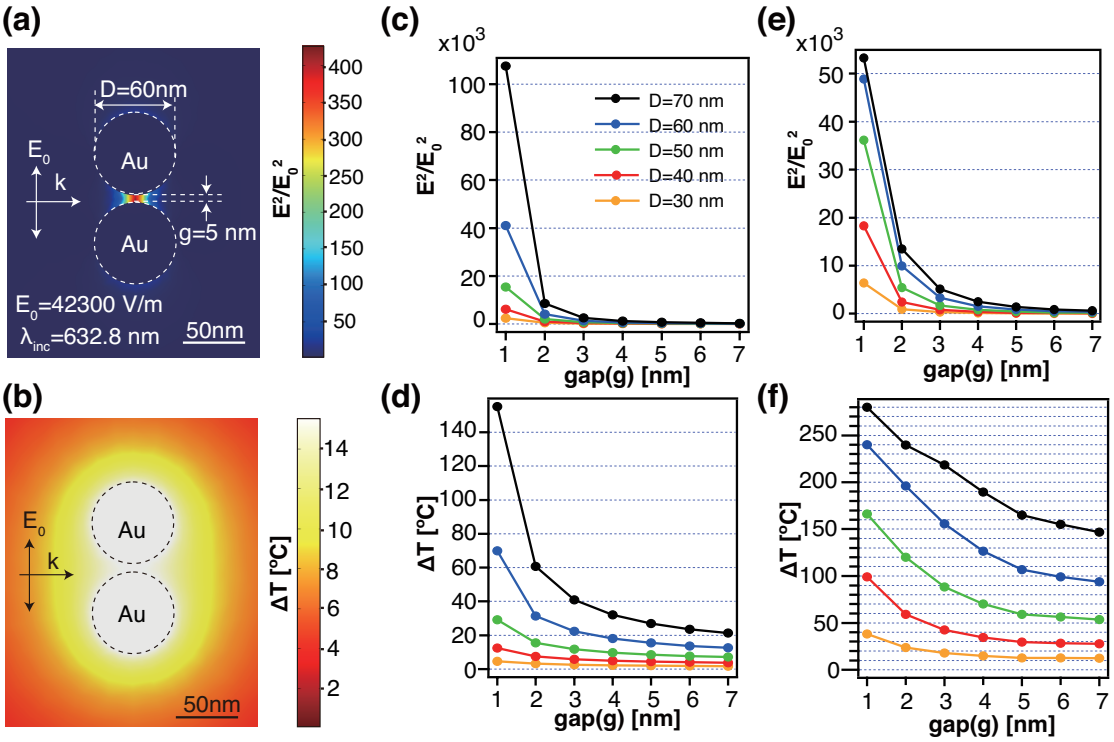

Figure 6.5. Calculated distributions of **(a)** electric field intensity enhancement and **(b)** temperature rise at Au-Au particles' gap. The diameter of particle and the gap are set to 60 nm and 5 nm, respectively. **(c)** and **(d)** are intensity enhancement and temperature rise at the Au-Au gap as a function of gap distance with various particle diameter for 632.8 nm excitation. **(e)** and **(f)** are the cases of Ag-Au gap for 532 nm excitation.

A p-polarized 632.8 nm and 532 nm plane wave with electric field magnitude of 4.23 x 10^5 V/m and 4.32 x 10^5 V/m (equivalent to optical powers of 50 μW and 36.7 μW used in Figs. 6.4(e) and 6.4(f)), respectively, and a propagation vector ***k*** parallel to the *x*-axis were used. Figures 6.5(a) and 6.5(b) show the electric field intensity and the temperature distribution around the gold particle gap using 632.8 nm light irradiation. The enhanced electric field localized at the gap in Fig. 6.5(a) induced the temperature rise of the particles and exhibited 15 ˚C temperature increase at the gap particle surface. The surrounding media (including the gap) was modeled as air in the calculation. When a

carbon nanotube with high thermal conductivity [6.18] filled the gap, however, the equilibrium temperature at the gap slightly decreased, although, the general trend of the dependence on gap and particle diameter was unchanged (data not shown). The experimental value is comparable to that of simulation with d = 60 nm but is less than the simulated value for d = 70 nm, which is reasonable since the diameter of the Au particle on the tip is within this range. The enhancement factor and the temperature rise are summarized in Fig. 6.5(c)-6.5(d) for 632.8 nm illumination and Fig. 6.5(e)-6.5(f) for 532 nm illumination. It was found that both the enhancement factor and the temperature rise were sensitive to the particle diameter and to the gap distance equivalent to the diameter of the observed carbon nanotubes. As a general trend, the higher the enhancement factor is, the higher the temperature becomes, which can be seen either when the gap becomes smaller or when the particle size gets larger. Moreover, Ag particles in 532 nm excitation showed relatively higher temperature as compared with Au particles in 632.8 nm owing to the higher enhancement of the Ag particle and the higher absorption of the Au particle at 532 nm. This trend is in good agreement with the experimentally obtained temperature rise in both excitation wavelengths. When the gap becomes larger, the enhancement factor is drastically decreased whilst the temperature rise shows moderate decrease. For both enhancement factor and temperature rise, the values converged to the case of a single isolated particle (gap = infinity), which is also similar to the case of s-polarized excitation for the gap (data not shown). Although it is practically difficult to control the gap and the size of the tip diameter in the experiment, the experimentally obtained temperature in this study is reasonably within the analytically expected temperature under the same excitation power. The relatively lower temperature in the experiment could originate from two factors: 1) the high thermal conductivity of CNTs located at the gap and 2) the higher thermal conductivity of the flat metallic substrate compared to metallic nanoparticles [6.18], both of which improve the heat dissipation of the experiment compared to the simulation.

When the incident laser power becomes very high, the tip enhancement factor can be reduced due to the temperature dependent Drude function [6.5], resulting in a nonlinear dependence of the temperature rise as a function of incident power density [6.20]. When the incident power is low, as used in our experiment, the temperature rise could be nearly proportional to the incident power. Power dependence experiments were conducted to see the effect of incident power on the temperature rise. Figure 6.6 compares the TE-THzRS spectra (far-field contribution are subtracted) of the s-CNT RBM taken at the same point (Point C in Fig. 6.4(c)) on the s-CNT sample, but using

three different incident powers, 50 μW (red line), 36.7 μW (blue line) and 25 μW (green line). Single Lorentzian fitting was used for both cases.

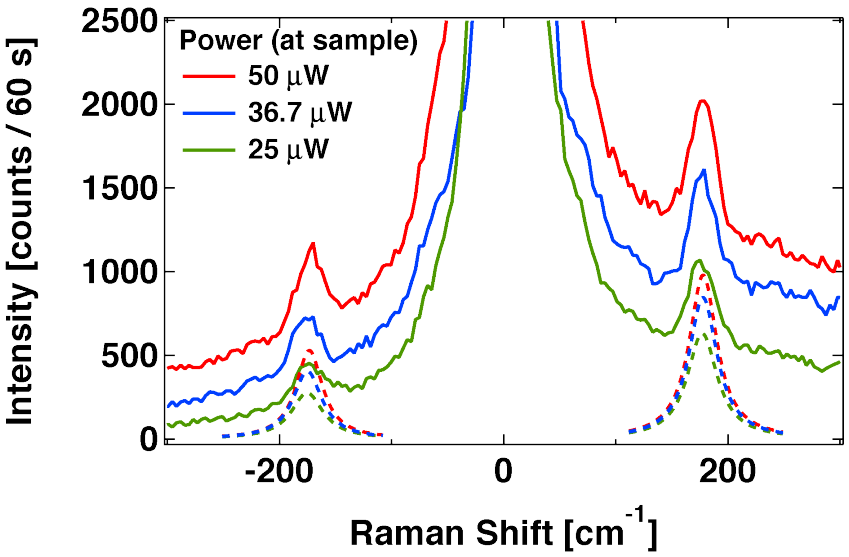

Figure 6.6. Comparison of TE-THzRS Raman spectra taken at point C of s-CNT for different incident powers. Solid lines indicate experimentally obtained data and dashed lines indicate fitting results.

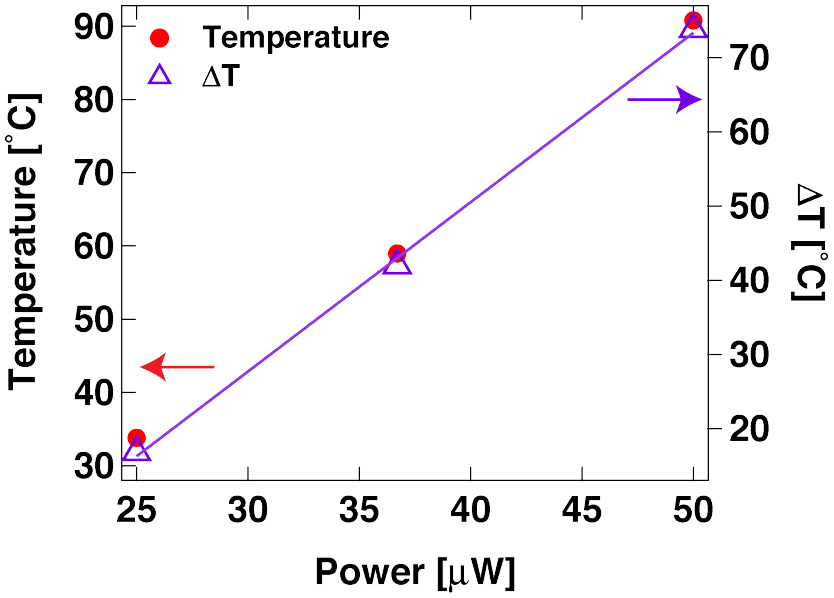

Figure 6.7. Plot of temperature and change in temperature versus power. Left-axis shows the calculated temperature while the right-axis shows the change in temperature.

For 50 μW, $\omega_{RBM\text{-}50}$ was 172.87 cm^{-1}. The $\dot{n}_{AS}/\dot{n}_{S}$ is 0.52 and the computed sample temperature is 90.8 ˚C. The temperature rise was ΔT_{50} = 73.8 ˚C. For 36.7 μW, $\omega_{RBM\text{-}36.7}$ was 177.8 cm^{-1}. The $\dot{n}_{AS}/\dot{n}_{S}$ is 0.49 and temperature is 59.0 ˚C. The temperature rise

was $\Delta T_{36.7}$ = 42.0 ˚C. For 25 μW, $\omega_{RBM\text{-}25}$ was 166.98 cm^{-1}. The $\dot{n}_{AS}/\dot{n}_{S}$ ratio was 0.46, yielding a lower sample temperature of 33.8 ˚C. The temperature rise was ΔT_{25} = 16.8 ˚C. Figure 6.7 summarizes these results displaying temperature and the change in temperature as a function of laser power. The change in temperature exhibits a linear relationship with the incident laser power, which is within the expectation when low laser power is used. It is observed that the temperature rise from 25 μW to 50 μW is quite large. One reason for the large temperature rise is a decrease in the gap distance and an increase in the enhancement of the electric field at the gap. A decrease in the gap distance can be brought about by drift. Although our TE-THzRS system is stable, a small amount of drift due to slight changes in the experimental environment (e.g. room temperature and mechanical vibrations) is unavoidable. Hence, small drift changed the observed positions with different gaps during the TE-THzRS measurements. An indication of this was that the obtained RBM frequencies for the 50 μW and 25 μW experiments were different. Temperature dependent RBM shift [6.21] is typically too small to exhibit such a large spectral shift observed between $\omega_{RBM\text{-}50}$ and $\omega_{RBM\text{-}25}$. The dependence of the enhancement factor on the gap distance is illustrated in the FEM calculations (Fig. 6.5(e)). Even just a 1 nm decrease in the gap distance can result to a two-fold increase in the enhancement factor. Accordingly, the higher enhanced signal due to the smaller gap increases the temperature. A further validation of the decrease in the gap distance for the case of 50 μW is the higher contrast between TE-THzRS and far-field spectra (a contrast of 6-fold and 3-fold for 50 μW and 25 μW, respectively. Data not shown), indicating that the enhancement was higher for the 50 μW data. The same experiments were conducted using the 632.8 nm illumination and m-CNT sample, and showed similar trends.

By developing TE-THzRS to see low frequency Raman modes in the nanoscale it is possible to determine the local sample temperature of s-CNT and m-CNT through the simultaneous detection of the anti-Stokes and Stokes Raman peaks of the RBM. FEM calculations showed that the temperature rise at the gap was dependent on the gap distance. This was because the gap distance dictated how high the enhancement factor would be. A higher enhancement factor meant a stronger electric field in the gap, thus resulting to a higher rise in the temperature. Experimental results were within the analytically predicted results from the FEM calculations. Through power dependence experiments, it was shown that the temperature on the sample for nanoscale sized volumes can be controlled well below 100 ºC by changing the incident power while keeping sufficiently high enhancement factor. The findings of this work are applicable to

other samples of interest, particularly biological samples that are prone to thermal damage. This work assures that TERS and TE-THzRS are one of the promising bioanalytical techniques for studying heat sensitive materials [6.22] and the various intermolecular and intramolecular interactions that occur in biological samples [6.23-6.24].

6.6. TE-THzRS AND CARBON NANOTUBES: A POSSIBLE NEXT STEP

A possible next step for utilizing TE-THzRS to study carbon nanotubes is the observation of ultra-low frequency modes whose frequencies are less than 100 cm^{-1}, as seen in Figs. 6.4(e) and 6.4(g). These peaks can be indicative of inter-tube interaction. It has been theoretically predicted that the E_{2g} mode of CNTs has low frequency peaks (around 20 cm^{-1}) [6.25, 6.26]. But this low frequency E_{2g} mode is greatly dependent on the chirality of the CNT [6.26]. Through TE-THzRS, thorough studies of these ultralow frequency peaks can be made and more knowledge about the properties of CNTs can be gathered.

6.7. REFERENCES

[6.1] **M.V. Balois**, N. Hayazawa, F.C. Catalan, S. Kawata, T. Yano, and T. Hayashi, Tip-enhanced THz Raman spectroscopy for local temperature determination at the nanoscale, *Analytical and Bioanalytical Chemistry*, *in press*, Vol. xx, pp. xx-xx, 2015.

[6.2] Downes A, Salter D, Elfick A (2006) Heating effects in tip-enhanced optical microscopy. Optics Express 14:5216-5222

[6.3] Zhang W, Schmid T, Yeo BS, Zenobi R (2008) Near-field heating, annealing, and signal loss tip-enhanced Raman spectroscopy. J Phys Chem C 112:2104-2108

[6.4] Malkovskiy, AV, Malkovsky VI, Kisliuk AM, Barrios CA, Foster MD, Sokolov AP (2009) Tip-induced heating in apertureless near-field optics. J Raman Spectrosc 40:1349-1354

[6.5] Tarun T, Hayazawa N, Yano T, Kawata S (2011) Tip-heating-assisted Raman spectroscopy at elevated temperatures. J Raman Spectrosc 42:992-997

[6.6] Hart TR, Aggarwal L, Lax B (1970) Temperature dependence of Raman scattering in silicon Phys Rev B 1:638

[6.7] Hayazawa N, Yano T, Kawata S (2012) Highly reproducible tip-enhanced Raman scattering using an oxidized and metallized silicon cantilever tip as a tool for everyone. J Raman Spectrosc 43:1177-1182

[6.8] Long, DA (1976) Raman Spectroscopy. McGraw-Hill, New York

[6.9] Rassat SD and Davis EJ (1994) Temperature measurements of single levitated microparticles using Stokes/anti-Stokes Raman intensity ratios, Appl Spectrosc 48:1498-1505

[6.10] Raravikar NR, Keblinski P, Rao AM, Dresselhaus MS, Schadler LS, Ajayan PM (2002) Temperature dependence of radial breathing mode Raman frequency of single-walled carbon nanotubes. Phys Rev B 66:235424

[6.11] Chiashi S, Murakami Y, Miyauchi Y, Murayama S (2008) Temperature dependence of Raman scattering from single-walled carbon nanotubes: undefined radial breathing mode peaks at high temperatures. Jpn J Appl Phys 47:2010-2015

[6.12] Oguchi M, Mochizuki M, Yano T, Hara M, Hayashi T (2014) Light-transmittable ultrasmooth gold film for gap-mode tip-enhanced Raman scattering spectroscopy. Chem Lett 43:808-810

[6.13] Deckert-Gaudig T, Deckert V (2009) Ultraflat transparent gold nanoplates – ideal substrates for tip-enhanced Raman scattering experiments. Small 5:432-436

[6.14] Kataura H, Kumazawa Y, Maniwa Y, Umezu I, Suzuki S, Ohtsuka Y, Achiba Y (1999) Optical properties of single-wall carbon nanotubes. Synthetic Metals 103:2555-2558

[6.15] Hayazawa N, Saito Y, Kawata S (2004) Detection and characterization of longitudinal field for tip-enhanced Raman spectroscopy. Appl Phy Lett 85:6239-6241

[6.16] Dresselhaus MS, Dresselhaus G, Saito R, Jorio A (2005) Raman spectroscopy of carbon nanotubes. Physics Reports 409:47-99

[6.17] Palik ED (1998) Handbook of Optical Constants of Solids. Academic Press, London

[6.18] Khan WA, Khan ZH, Rahi M (2014) Fluid flow and heat transfer of carbon nanotubes along a flat plate with Navier slip boundary. Appl Nanosci 4:633-641

[6.19] Feng B, Zhixin L, Zhang X (2009) Prediction of size effect on thermal conductivity of nanoscale metallic films. Thin Solid Films 517:2803-2807

[6.20] Albella A, de la Osa RA, Moreno F, Maier SA (2014) Electric and magnetic field enhancement with ultralow heat radiation dielectric nanoantennas: considerations for surface-enhanced spectroscopies. ACS Photonics 1:524-529

[6.21] Ci L, Zhou Z, Song L, Yan X, Liu D, Yuan H, Gao Y, Wang J, Liu L, Zhou W, Wang G, Xie S (2003) Temperature dependence of resonant Raman scattering in double-wall carbon nanotubes. Appl Phys Lett 82:3098

[6.22] Hermann P, Hermelink A, Lausch V, Holland G, Möller L, Bannert N, Naumann D (2011) Evaluation of tip-enhanced Raman spectroscopy for characterizing different virus strains. Analyst 136:1148

[6.23] Lazarevic JJ, Uskokovic-Markovic S, Jelikic-Stankov M, Radonjic M, Tanaskovic D, Lazarevic N, Popovic ZV (2014) Intermolecular and low-frequency intramolecular Raman scattering study of racemic ibuprofen. Spectrochimica Acta Part A: Molecular and Biomolecular Spectroscopy 126:301-305

[6.24] Rzeznicka II, Horino H, Kikkawa N, Sakaguchi S, Morita A, Takahashi S, Komeda T, Fukumura H, Yamada T, Kawai M (2013) Tip-enhanced Raman spectroscopy of 4,4'-bipyridine *N,N'*-dioxide adsorbed on gold thin films. Surface Science 617:1-9

[6.25] R. Saito, T. Takeya, T. Kimura, G. Dresselhaus and M.S. Dresselhaus, *Phys. Rev. B*, **57**, pp. 4145-4153, 1998.

[6.26] A.M. Rao, E. Richter, S. Bandow, B. Chase, P.C. Eklund, K.A. Williams, S. Fang, K.R. Subbaswamy, M. Menon, A. Thess, R.E. Smalley, G. Dresselhaus and M.S. Dresselhaus, *Science*, **275**, pp. 187-191, 1997.

Chapter 7. Summary and Conclusions

This thesis deals with analyses of local physicochemical properties of strained-silicon nanowires (e-SiNWs) and carbon nanotubes (CNTs) via micro and nano-Raman spectroscopy, respectively, to improve transistor technology. This work's significance is addressing the effects of size reduction and complexity increase of transistor geometry – a trend dictated by Moore's law – on transistor performance. Present-day transistors employ e-Si as channel material using high stress to increase carrier mobility. The amount of stress is altered, however, during nanopatterning inducing dimension-dependent anisotropic stress relaxation, suggesting reduced carrier mobility and size limitations. To overcome these problems, CNTs as alternative materials are considered because of their intrinsic electronic transport properties and ultrathin body. Function optimization can be realized through characterization of CNT's local electronic properties utilizing nano-Raman.

Chapter 1 briefly discussed the background, purpose and significance of this work. Present-day transistors utilize strained silicon technology as channel material to improve performance by increasing electron mobility. It is constantly assumed that isotropic (uniaxial) stress is used since the channels are very narrow. In order to keep pace with Moore's law, however, transistors are becoming smaller and more complicated. As a result, the stress is no longer isotropic but more anisotropic. Scaling of silicon causes other problems such as current leakage and the size limitation to maintain strain. It is the latter of these problems that is pushing scientists and engineers to find alternate channel materials in order to maintain Moore's law. One possible channel material is carbon nanotubes. Carbon nanotubes have superior electronic transport properties and an ultrathin body, which can address the problems of leakage and size limitation. There have already been works resulting to carbon nanotube transistors and even a functional carbon nanotube computer, but all these are still in the development stage. A deeper understanding of the structural and electronic properties of carbon nanotubes is needed to help further the development of carbon nanotube research for transistor technology.

Both strained silicon and carbon nanotubes are nano-sized materials and in order to study them, special characterization techniques with high sensitivity and spatial resolution are needed. These techniques are micro and nano-Raman spectroscopy. For strained silicon, micro-Raman spectroscopy is utilized because of its high sensitivity to strain. Carbon nanotubes, on the other, utilize nano-Raman spectroscopy because of its

spatial resolution. But these characterization techniques are not without problems. Micro-Raman spectroscopy is insensitive to anisotropy making it a challenge to study anisotropic stress in strained silicon. Nano-Raman spectroscopy is susceptible to heating making it an invasive technique that can alter and damage the sample. Solutions to these problems were presented in this thesis, making it possible to do precise characterization and analysis of the aforementioned nano-sized materials.

Chapter 2 gave a theoretical background on how focused light is diffracted across an interface. This chapter begins with how the electric field component of light is focused using an aplanatic lens. The discussion then moves to the integral representation of an electric field and how this representation changes as the field travels between two media of different refractive index. The resulting field that exits the final medium is a superposition of the incident, reflected and transmitted fields. The effect of polarization on the profile of the individual components of the electric field were also discussed. As proof of principle, a two-layer system consisting of glass/air was studied for the numerical simulations, and was extended to a more complex system (three-layers) in Chapter 3. *It was shown that different polarizations (linear, radial and azimuthal) generated different electric field distributions in the transverse (E_x + E_y) and longitudinal (E_z) components. Only linear and radial polarization generated the E_z component. For the longitudinal component, radial polarization generated a strong and tightly focused spot. The strength of this field is dependent on the numerical aperture (NA) of the objective lens. Linear polarization also generated an E_z field but the distribution composed of two lobes, which would affect spatial resolution.*

Chapter 3 discussed the theory of Raman scattering in Silicon and the polarization selection rules. Stress in Silicon (particularly strained Silicon) can be quantified through the detection of longitudinal optical (LO) and transverse optical (TO) phonons. The detection of these phonon modes is dictated by their respective Raman tensor. If all three phonons are detected, a clear picture of the stress distribution in strained Silicon can be made. From the polarization selection rules, it was found that TO modes could not be detected in a backscattering geometry, a limitation when such geometry is used. In order to find a way to detect the undetectable TO modes and determine the contributions of both LO and TO modes, three-dimensional electric field calculations were conducted based on the electric field distribution inside silicon using the theory developed in Chapter 2. A three-layer system consisting of oil/strained-silicon/air was used. After calculating the electric field inside silicon the Raman tensor of both LO and TO modes was applied. *It was shown via numerical simulations that through the use of a*

high NA lens and appropriate polarization, it is possible to directly detect the undetectable TO phonons. Therefore making the initially insensitive micro-Raman spectroscopy sensitive anisotropy. This makes it possible to accurately determine the stress in strained Silicon structures such as nanowires. Nanowire structures were chosen because strained Silicon based transistors have nanowire-like channels.

Chapter 4 focuses on the redistribution of stress in strained Silicon nanowires after nanopatterning. These strained Silicon nanowires mimic the strained Silicon channels found in present-day transistors. Micro-Raman spectroscopy was utilized for its sensitivity to stress and fast data acquisition. *By implementing the experimental conditions simulated in Chapter 3, TO phonon splitting was experimentally observed for the first time. Through the detection of the two TO phonons, it was found that the stress in nanowires along the x-axis (long axis) was high (even higher than the bulk material from where it came from). It was also found that the stress along the y-axis (short axis) is non-zero. These findings are important because the prevalent beliefs are 1) when the dimensions of strained Silicon nanowires become smaller, the stress decreases and 2) the stress along nanowire structures in uniaxial (stress along y axis = 0). The work in Chapter 4 presents a new method of stress characterization that is sensitive to anisotropic stress and will be very useful for strain nanoengineering of transistors.*

Chapter 5 shifts the focus of this work to carbon nanotubes giving a brief background on their properties. The Raman spectra of CNTs was also discussed and what information can be extracted from these spectra was explained. To study CNTs whose diameters range from 0.7 to 10 nm, nano-Raman spectroscopy techniques such as TERS must be employed to spatially resolve them. *This chapter demonstrates the power of TERS in terms of spatial resolution and signal enhancement.*

Chapter 6 discusses the problem of heating in TERS. Since TERS generates a strong enhanced electric field, it is unavoidable that this electric field can generate heat. This heating can affect the sample, tip and substrate (if it is metallic), thus affecting sample analysis. In order to establish TERS as a truly non-intrusive analytical tool, the local temperature generated at the tip apex must be determined. This is most especially important when studying heating effects in CNTs, which is an important aspect for transistors. *This chapter presents a novel temperature determination technique that can detect the temperature and temperature changes at the nanoscale. This technique is called tip-enhanced THz Raman spectroscopy. Through the detection of the RBM of CNTs and the Boltzmann distribution, the temperature of the CNTs was determined. It*

was also found that at low temperatures (less than 100˚C) the temperature can be controlled by controlling the power of the illuminating laser. TE-THzRS is not only useful for CNTs but can be extended to other fields and applications as well, such as biological samples.

List of Papers:

1. **M.V. Balois**, N. Hayazawa, F.C. Catalan, S. Kawata, T. Yano, and T. Hayashi, Tip-enhanced THz Raman spectroscopy for local temperature determination at the nanoscale, *Analytical and Bioanalytical Chemistry*, *accepted*, Vol. xx, pp. xx-xx, 2015.

2. **M.V. Balois**, N. Hayazawa, A. Tarun, S. Kawata, M. Reiche and O. Moutanabbir, "Direct optical mapping of anistropic stresses in nanowires using transverse optical phonon splitting", *Nano Lett.* 14, 3789-3798, **2014.**

3. A. Tarun, N. Hayazawa, **M.V. Balois**, S. Kawata, M. Reiche and O. Moutanabbir, "Stress redistribution in individual ultrathin strained silicon nanowires: a high-resolution polarized Raman study", *New Journal of Physics* 15, 053042, **2013**.

List of Presentations (International conference):

1. **M.V. Balois**, N, Hayazawa, A. Tarun, O. Moutanabbir and S. Kawata, "Direct Determination of Stress Anisotropy in Strained Silicon Nanowires via Phonon Mode Splitting", *24th International Conference on Raman Spectroscopy*, Jena, Germany, August, **2014**. (POSTER)

2. A. Tarun, N. Hayazawa**, M.V. Balois**, S. Kawata, M. Reiche, and O. Moutanabbir, "Unravelling the complexity of anisotropic stress in ultrathin strained silicon nanowires" XXIV International Conference on Raman Spectroscopy (ICORS), p.57 (August 8-13, Jena), **2014**.

3. **M.V. Balois**, N, Hayazawa, A. Tarun, O. Moutanabbir and S. Kawata, "Anisotropic Stress Relaxation in Strained Silicon Nanowires Characterized by High Precision Polarized Raman Microscopy", *International Conference on Vibrational Spectroscopy 7*, Kobe, Japan, August, **2013.** (ORAL)

4. N. Hayazawa, A. Tarun, **M.V. Balois**, S. Kawata, and O. Moutanabbir, "Local Stress in Nanowires Unraveled by Raman Spectroscopy", 7th International Conference on Advanced Vibrational Spectroscopy (ICAVS), Kobe, Japan, August 25-30, **2013**.

5. A. Tarun, N. Hayazawa, **M. V. Balois**, S. Kawata, and O. Moutanabbir, "Stress Profiles in Single Ultrathin Strained Silicon Nanowires", The 2013 MRS Spring Meeting (April 1-5, Moscone, USA) **2013**.

6. **M.V. Balois**, N, Hayazawa, A. Tarun, O. Moutanabbir and S. Kawata, "Dimension dependence of strain-relaxation of strained silicon nanostructures", *29th Conference of the Physics Society of the Philippines*, October, **2011**. (ORAL)

7. **M.V. Balois** and P. Almoro, "Wavefront sensing using correlations of two speckle intensity measurements and a Shack Hartmann-based algorithm", *28th Conference of the Physics Society of the Philippines*, October, **2010**. (ORAL)

8. **M.V. Balois** and P. Almoro, "Technique for controlling chromatic dispersion of full-color holograms", *22nd Conference of the Physics Society of the Philippines*, October, **2004**. (ORAL)

List of Presentations (Domestic conference):

1. **M.V. Balois**, N, Hayazawa, T. Hayashi and S. Kawata, “Tip-enhanced THz Raman spectroscopy for local temperature determination at the nanoscale”, *Noyori School 2014*, Hayama, Japan, December, **2014**. (POSTER)

2. **M.V. Balois**, N, Hayazawa, T. Hayashi and S. Kawata, “Tip-enhanced THz Raman spectroscopy for local temperature determination at the nanoscale”, *RIKEN Center for Advanced Photonics Symposium*, Sendai, Japan, November, **2014**. (POSTER)

3. **M.V. Balois**, L. Dasallas, N. Hayazawa, O. Moutanabbir and S. Kawata, “Tuning Stress of Nanowires via Nanomembrane Edge Induced Stress Field Study by Polarized Raman Microscopy”, *Annual Meeting of the Spectroscopical Society of Japan*, Wako, Japan, May, **2014**. (POSTER)

4. **M.V. Balois**, N, Hayazawa, A. Tarun, O. Moutanabbir and S. Kawata, “Characterization of Anisotropic Stress Relaxation in Strained Silicon Nanowires via Polarized Raman Microscopy using a High NA Lens”, *Annual Meeting of the Spectroscopical Society of Japan*, Osaka, Japan, November, **2013**. (ORAL)

5. **M. V. Balois**, N. Hayazawa, A. Tarun, O. Moutanabbir, and S. Kawata, "Precise and stable polarization control in a tight focusing system for accurate characterization of strained silicon nanostructures" JSAP-OSA Joint Symposia 2013 Abstracts, (Optical Society of America, 2013) paper 19a_D5_9 (Sep. 16-20, Kyoto, Japan), **2013**. (ORAL)

6. **M.V. Balois**, N, Hayazawa, A. Tarun, S. Kawata and O. Moutanabbir, “Anisotropic stress relaxation in strained silicon nanowires via polarized Raman microscopy using a high NA lens”, *RIKEN Center for Advanced Photonics Symposium*, Wako, Japan, October, **2013**. (POSTER)

7. **M.V. Balois**, N, Hayazawa, A. Tarun, O. Moutanabbir and S. Kawata, “Raman Analysis of the Complex Nanopatterning Induced Redistribution of Stress in Single Ultrathin Strained Silicon Nanowires”, *Noyori Summer School 2013*, Kobe, Japan, September, **2013**. (POSTER)

8. **M.V. Balois**, N, Hayazawa, A. Tarun, O. Moutanabbir and S. Kawata, “Complex nanopatterning induced redistribution of stress in single ultrathin strained silicon nanowires”, *Annual Meeting of the Spectroscopical Society of Japan*, Tokyo, Japan, November, **2012**. (POSTER)

D. Awards and Distinctions

1. **Best Poster** - Analytical and Bioanalytical Chemistry: *24th International Conference on Raman Spectroscopy*, "Direct Determination of Stress Anisotropy in Strained Silicon Nanowires via Phonon Mode Splitting", Jena, Germany, August, 15, **2014**.

2. **2013 Young Scientist Presentation Award of the Spectroscopical Society of Japan**: "Characterization of Anisotropic Stress Relaxation in Strained Silicon Nanowires via Polarized Raman Microscopy using a High NA Lens" *Annual Meeting of the Spectroscopical Society of Japan*, Osaka, Japan, November 21, **2013.**

3. **Noyori Prize (Best Poster Award)**: *RIKEN – Noyori Summer School*, "Raman Analysis of the Complex Nanopatterning Induced Redistribution of Stress in Single Ultrathin Strained Silicon Nanowires", September 7, **2013**.

Acknowledgements

I would first like to express my gratitude to my Academic Supervisor, Associate Professor Tomohiro Hayashi, for giving me the opportunity to pursue my doctoral studies here in Tokyo Institute of Technology. Without his belief in my abilities and desire to do research here in Japan, all this would not be possible. I am also thankful for his guidance not only in research, but also in the other important aspects of life.

I am also very grateful to my RIKEN Supervisor, Dr. Norihiko Hayazawa, for being my mentor, who introduced me to the field of near-field scanning probe microscopy and Raman spectroscopy. Although going through this research path was and still is filled with challenges, his constant advice, constructive criticism and giving me the freedom of what I want to do has helped mold me to become a better researcher. “If you want to learn, you will learn,” are his words of wisdom that have been and will continue to be my mantra, as I start off on my own in this journey of science.

I would like to thank the my panel and reviewers of my doctoral thesis, Professor Masahiko Hara, Associate Professor Fusao Kitamura and Dr. Kazunari Ozasa, for their questions during my defense, which have helped me gain an even deeper understanding of my own work and seeing my work through the eyes of other researchers from other scientific fields. Their insightful comments and suggestion have helped further improve the structure and content my doctoral thesis.

I would also like to thank my colleagues and collaborators, Dr. Alvarado Tarun and Dr. Oussama Moutanabbir, for introducing me to the concept and material called strained Silicon. I have learned a lot from our Skype discussions and realized the true value of having colleagues and friends in the field of Science. Interdisciplinary work and collaboration is an important factor in improving not only one’s research but also in gaining a broader view of the world.

I appreciate and enjoyed the discussions I had with Assistant Professor Taka-aki Yano during my progress reports, JDI and those random times when I have scientific questions or I just feel like chatting about our common interests such as my home country, the Philippines. I would also like to thank Dr. Atsushi Taguchi for teaching me how to use the FDTD program called Lumerical. I know this knowledge will go a long way, especially if I want to work on theoretical modeling. I would like to thank Dr. Francesca Celine Catalan for her help and advice during my TERS experiments.

My research work would not have gone smoothly without the help our previous secretary in Tokyo Tech, Ms. Mari Miura. She has been my “mother” in Tokyo Tech for the two-and-a-half years of my PhD student life. I am very thankful for her help especially with important announcements and documents, since I am always in RIKEN. I enjoyed chatting with her about various things, both in English and Japanese. I would also like to thank our current secretary, Ms. Nobue Ueda, who has also been a great help in handling all the administrative related requirements I need in the last half year of my PhD course.

I would like to thank Dr. Satoshi Kawata for letting me be a member of his Nanophotonics Laboratory (NaPs) and his Near-Field Nanophotonics Research Team in RIKEN. His way of thinking and his aggressive nature in science has been a strong influence on how I do my research and what kind of mindset I must have as I tackle the challenges of science in the international community.

I would like to thank the generosity of Dr. Yousoo Kim, Chief Scientist of the Surface and Interface Science Laboratory, for letting me stay in his lab in the last six months of my PhD course. I would also like to thank Dr. Emiko Kazuma for letting me use her Lumerical program and for teaching me how to allocate the resources of the computer for faster computation. Her patience and kindness have encouraged me a lot.

My life in Tokyo Tech has been filled with fun and exciting experiences, not just in science, because of my lab mates in the Hara-Hayashi Laboratory. My thanks go to my lab mates from the Hayashi Lab: Mr. Masahiro Oguchi, Mr. Masahito Mochizuki, Mr. Taito Sekine, Ms. Kaori Takano, Mr. Ryo Hamamoto, Ms. Syifa Asatyas, Mr. Tetsu Ogawa, Mr. Kosuke Miyaue, Mr. Takashi Nyu, Ms. Ganchimeg Lkhamsuren, Ms. Rina Ohashi, Mr. Ryongsok Chang, Mr. Makoto Hirohara, Mr. Tatsuhiro Maekawa, Mr. Yoshiki Mizushita, and Ms. Azuho Tsunoi; and to my lab mate from the Hara Lab: Ms. Tika Kusbandiah, Mr. Kosuke Hara, Ms. Narangerel Ganbaatar, Mr. Yuya Nakazawa, Mr. Keisuke Yoshida, Mr. Yuta Tsuchimoto, Ms. Nina Matsuzaki, Ms. Kanae Imai, Ms. Arie Senda, and Mr. Yasuhiro Morita. I would like to thank them all – those who are current students and those who have graduated – for the friendships that have been made, which I hope lasts a lifetime. The questions you keep asking me have helped improve my analysis skills and have pushed me to study even more. I feel that I have lived my student life here in Japan to the fullest because of these wonderful people.

I would like to thank RIKEN's Program for Junior Scientists and for the financial support provided to me as an International Program Associate. This program made it possible for me to do research in RIKEN and be able to interact with world-class researchers, whom I aspire to become someday.

I would like to thank Mr. Masahiro Oguchi, who has walked the PhD path with me, for his constant intellectual and emotional support especially at the times when I felt like I have hit a wall or reached a new low. His irreplaceable company has kept my loneliness at bay as I am far away from my family and his encouragement has made me aspire for greater heights. I wish him all the best as he finishes his PhD.

I dedicate this thesis to my family, who has been the solid foundation of my life ever since the very first day of my existence. I am very much thankful for their patience as I told them stories of my life here in Japan on an almost nightly basis. And I am most thankful for their love and understanding that have kept me going no matter what.

Maria Vanessa Cases Balois
August 2015

APPENDIX A: COPYRIGHT PERMISSIONS

From: **pubscopyright** copyright@osa.org
Subject: RE: Request for Copyright Permission
Date: June 12, 2015 at 11:49 PM
To: Maria Vanessa Balois mariavanessa.balois@riken.jp

Dear Dr. Balois,

Thank you for contacting The Optical Society.

OSA considers your requested use of its copyrighted material to be Fair Use under United States Copyright Law. It is requested that a complete citation of the original material be included in any publication.

Let me know if you have any questions.

Kind Regards,

Susannah Lehman

Susannah Lehman
June 12, 2015
Authorized Agent, The Optical Society

From: Maria Vanessa Balois [mailto:mariavanessa.balois@riken.jp]
Sent: Monday, June 01, 2015 11:15 PM
To: pubscopyright
Cc: Vanni RIKEN Balois
Subject: Request for Copyright Permission

Dear OSA:

I am Maria Vanessa Balois, a PhD student in Tokyo Institute of Technology currently doing research in RIKEN. I am currently writing my PhD dissertation and would like to use the following figures:

1.Figure 1 from P. Török, P. Varga, Z. Laczik and G. R. Booker, Electromagnetic diffraction of light focused through a planar interface between materials of mismatched refractive indices: an integral representation. *Journal of the Optical Society of America A*, Vol. 12, No. 2, February 1995.

2.Figure 2 from the same article in #1.

A section of one chapter in my dissertation describes the derivation of equations I used to simulate an electric field propagating across an interface. My derivation is based on the aforementioned article and the figures would greatly help the readers (and referees) of my dissertation to visualise the systems I am describing.

My complete contact information is as follows:

Maria Vanessa Balois
International Program Associate

International Program Associate
Surface & Interface Science Laboratory
The Institute of Physical and Chemical Research (RIKEN)
2-1 Hirosawa, Wako, Saitama, JAPAN 351-0198
Tel: +81-48-467-4073
Fax: +81-48-467-1945
Email: mariavanessa.balois@riken.jp

Thank you very much.

Best,
Maria Vanessa Balois

«————————————————»

Maria Vanessa Balois
International Program Associate
Surface & Interface Science Laboratory
The Institute of Physical and Chemical Research (RIKEN)
2-1 Hirosawa, Wako, Saitama, JAPAN 351-0198
Tel: +81-48-467-4073
Fax: +81-48-467-1945
Email: mariavanessa.balois@riken.jp

From: **Permissions** permissions@iop.org
Subject: Re: PLS Clear Permission Request - [711] NEW JOURNAL OF PHYSICS (13672630)
Date: June 16, 2015 at 5:01 PM
To: mvbalois@gmail.com

Dear Maria Vanessa Balois,

Thank you for your request to reproduce IOP Publishing material in your thesis.

Regarding:

'Stress redistribution in individual ultrathin strained silicon nanowires: a high-resolution polarized Raman study' (New Journal of Physics 15 (2013) 053042)

The material you have requested was published under a CC BY licence (http://creativecommons.org/licenses/by/3.0/).

Therefore you may reuse the content without permission, so long as you reference it adequately and make the figure available under the same terms.

Regarding:
Figure 1 (Nanotechnology 23 (2012) 465203)

We are happy to grant permission for the use you request on the terms set out below.

Conditions

Non-exclusive, non-transferable, revocable, worldwide, permission to use the material in print and electronic form will be granted subject to the following conditions:

- Permission will be cancelled without notice if you fail to fulfil any of the conditions of this letter.
- You will make reasonable efforts to contact the author(s) to seek consent for your intended use. Contacting one author acting expressly as authorised agent for their co-authors is acceptable.
- You will reproduce the following prominently alongside the material:

a the source of the material, including author, article title, title of journal, volume number, issue number (if relevant), page range (or first page if this is the only information available) and date of first publication. This information can be contained in a footnote or reference note; or

a a link back to the article (via DOI); and

a if practical and IN ALL CASES for works published under any of the Creative Commons licences the words '© IOP Publishing. Reproduced with permission. All rights reserved'

- The material will not, without the express permission of the author(s), be used in any way which, in the opinion of IOP Publishing, could distort or alter the author(s)' original intention(s) and meaning, be prejudicial to the honour or reputation of the author(s) and/or imply endorsement by the author(s) and/or IOP Publishing.
- Payment of £0 is received in full by IOP Publishing prior to use.

Special Conditions – For STM Signatories ONLY (as agreed as part of the STM Guidelines)

Any permissions granted for a particular edition will apply also to subsequent editions and for editions in other languages, provided such editions are for the work as a whole in situ and does not involve the separate exploitation of the permitted illustrations or excerpts.

If you have any questions, please feel free to contact our Permissions team at permissions@iop.org.

I should be grateful if you would acknowledge receipt of this email.

Kind regards,

Zoe Caverlek

Publishing Assistant

IOP Publishing

Please note: We do not usually provide signed permission forms as a separate attachment. Please print this email and provide it to your publisher as proof of permission.

From: <plsclear@iop.org.uk>
To: <permissions@iop.org>,
Cc: <plsclear@iop.org.uk>, <plsdeartheil@gmail.com>
Date: 12/06/2015 10:04
Subject: PLS Clear Permission Request - [711] NEW JOURNAL OF PHYSICS (13672630)

Here is a permissions request for you. It has been generated by PLSclear, the Publishers Licensing Society's new permissions tool.

This tool ensures that

- you only receive requests for content you own, and that the requests go to the right people in your company
- you receive all the necessary information to grant requests (PLSclear uses a questionnaire that has been developed by some of the UKs leading rights specialists).

We hope this saves you time and makes managing the process easier.

If this is not one of your titles, you cannot grant permission or perhaps we have emailed the wrong contact, then please click the following link and tell us so that we can update our records: [Unable to process this request]

I am applying for permission for:

NEW JOURNAL OF PHYSICS (13672630)
Article extract
year of publication: 2013
volume number: 15
title of article: Stress redistribution in individual ultrathin strained silicon nanowires: a high-resolution polarized Raman study
author(s): Alvarado Tarun, Norihiko Hayazawa, Maria Vanessa Balois, Satoshi Kawata, Manfred Reiche, Ousmane Moutanabbir
page number: 053042
number of words: 6758
additional information: I am one of the co-authors of this paper and I would like to use the entire article if possible as a chapter for my Thesis.

To be used in:

A Book, Journal, Magazine or Academic Paper...
The Thesis details are
type of document: Thesis
publication title: Characterization of local physicochemical properties of nano-sized materials via micro and nano Raman spectroscopy
estimated publication date: September 2015
other relevant information: I am one of the co-authors of the aforementioned paper and I would like to use this article as one chapter of my Thesis.

Please respond directly to the person making the request. They have not received your company name or contact details.

Contact details are

Name: Maria Vanessa Balois
Email: mvbalois@gmail.com
Address: Surface and Interface Science Laboratory;
Hirosawa 2-1, Wako-shi
Town /City: Saitama
Post Code: 351-0198

Help us improve PLSclear: 5 quick questions

I am applying for permission for:

NANOTECHNOLOGY (09574484)
A illustration extract
content source: Online
issue date: October 23, 2012

issue number: **23**

article title: **Nanometric locking of the tight focus for optical microscopy and tip-enhanced microscopy**

figure number &title / caption: **Figure 1. Schematic of the focus locking system consisting of an objective lens, a sample stage and a capacitive sensor.**

position on page: **Upper half**

reproduction colour: **Full Colour**

reproduction size: **Half page**

positioning: **inside or later pages**

will it be cropped: **No**

full details of how it will be altered: **I will remove the image of the Si cantilever and the XY-PZT**

To be used in:

A **Book, Journal, Magazine or Academic Paper...**

The **Thesis** details are

type of document: **Thesis**

publication title: **Characterization of local physicochemical properties of nano-sized materials via micro and nano Raman spectroscopy**

estimated publication date: **September 2015**

other relevant information: **I used the same focus locking system as the one described in the paper. The author, Dr. Norihiko Hayazawa, is my research supervisor.**

Please respond directly to the person making the request. They have not received your company name or contact details.

Contact details are

Name: **Maria Vanessa Balois**

Email: **mvbalois@gmail.com**

Address: **Surface and Interface Science Laboratory**
Hirosawa 2-1, Wakoshi

Town /City: **Saitama**

Post Code: **351-0198**

Help us improve PLSclear: 5 quick questions

Home | Account Info | Help | Live Chat

Title: Mapping the "Forbidden" Transverse-Optical Phonon in Single Strained Silicon (100) Nanowire

Author: Alvarado Tarun, Norihiko Hayazawa, Hidekazu Ishitobi, et al

Publication: Nano Letters

Publisher: American Chemical Society

Date: Nov 1, 2011

Logged in as:
Maria Vanessa Balois
Account #: 3000924141

LOGOUT

PERMISSION/LICENSE IS GRANTED FOR YOUR ORDER AT NO CHARGE

This type of permission/license, instead of the standard Terms & Conditions, is sent to you because no fee is being charged for your order. Please note the following:

- Permission is granted for your request in both print and electronic formats, and translations.
- If figures and/or tables were requested, they may be adapted or used in part.
- Please print this page for your records and send a copy of it to your publisher/graduate school.
- Appropriate credit for the requested material should be given as follows: "Reprinted (adapted) with permission from (COMPLETE REFERENCE CITATION). Copyright (YEAR) American Chemical Society." Insert appropriate information in place of the capitalized words.
- One-time permission is granted only for the use specified in your request. No additional uses are granted (such as derivative works or other editions). For any other uses, please submit a new request.

If credit is given to another source for the material you requested, permission must be obtained from that source.

BACK CLOSE WINDOW

RightsLink®

Home | Account Info | Help | Live Chat

Logged in as:
Maria Vanessa Balois
LOGOUT

Title: Direct Optical Mapping of Anisotropic Stresses in Nanowires Using Transverse Optical Phonon Splitting

Author: Maria Vanessa Balois, Norihiko Hayazawa, Alvarado Tarun, et al

Publication: Nano Letters

Publisher: American Chemical Society

Date: Jul 1, 2014

PERMISSION/LICENSE IS GRANTED FOR YOUR ORDER AT NO CHARGE

This type of permission/license, instead of the standard Terms & Conditions, is sent to you because no fee is being charged for your order. Please note the following:

- Permission is granted for your request in both print and electronic formats, and translations.
- If figures and/or tables were requested, they may be adapted or used in part.
- Please print this page for your records and send a copy of it to your publisher/graduate school.
- Appropriate credit for the requested material should be given as follows: "Reprinted (adapted) with permission from (COMPLETE REFERENCE CITATION). Copyright (YEAR) American Chemical Society." Insert appropriate information in place of the capitalized words.
- One-time permission is granted only for the use specified in your request. No additional uses are granted (such as derivative works or other editions). For any other uses, please submit a new request.

BACK CLOSE WINDOW